GRADUATE PROGRAM IN ELECTRICAL ENGINEERING

Nitride semiconductors as carrier-selective contacts for silicon heterojunction solar cells.

Davi Marcelo Fébba

Itajubá

December 15, 2021

UNIVERSIDADE FEDERAL DE ITAJUBÁ - UNIFEI
GRADUATE PROGRAM IN ELECTRICAL ENGINEERING

Davi Marcelo Fébba

Nitride semiconductors as carrier-selective contacts for silicon heterojunction solar cells.

Doctoral thesis submitted to the Graduate Program in Electrical Engineering, in partial fulfillment of the requirements for the degree of Doctor of Science in Electrical Engineering

Supervisor: Prof. Dr. Edson da Costa Bortoni
Co-supervisor: Prof. Dr. Rero Marques Rubinger

Itajubá
December 15, 2021

Acknowledgements

I firstly thank God for all the blessings bestowed upon me, and for helping me to overcome the many hurdles I have faced during my journey.

I warmly thank my advisors, Prof. Dr. Rero Rubinber and Prof. Dr. Edson Bortoni, for their never-ending support and guidance throughout these years. I appreciate their trust in my work and thank them for motivating me to pursue new challenges.

Special thanks go to Dr. Mathieu Boccard, who warmly welcomed me in his team during my time as a visiting doctoral student at EPFL's PV-LAB in Neuchâtel, Switzerland. His patience, support, and mentorship were fundamental not only for the development of this work but played a key role in my scientific career.

I also warmly thank Prof. Dr. Christophe Ballif and Prof. Dr. Aïcha Hessler-Wyser for allowing me work in PV-LAB, which was a turning point in my life. Many thanks also go to Karine Frossard for her willingness to help me with everyday life situations in Switzerland, always in a good mood.

I also thank the support of my colleagues at PV-LAB, especially Julien Hurni, for the measurement and processing of X-ray diffractograms, Luca Antognini, Julie Dréon, Jonathan Thomet, Vincent Paratte, and Wenjie Lin, for contributing to this work in many ways. Special thoughts go to Cristóvão Vieira, Julia Dias, and Mathijs van der Meer. Their friendship made my time in Switzerland easier and certainly much funnier.

I express my most sincere gratitude to my parents for their invaluable support and encouragement. I also warmly thank Talita for being supportive, with her never-ending patience, and for some code debugging now and then.

Finally, I acknowledge the financial support granted by CAPES and CNPq, as well as the Swiss Government Excellence Scholarship granted by the FCS (Switzerland).

"But still try, for who knows what is possible..."
(Michael Faraday)

Resumo

Este trabalho apresenta a caracterização elétrica de camadas de $ZnSn_xGe_{1-x}N_2$ (ZTGN) ($10\% < x < 90\%$) depositadas em substrato de vidro por sputtering combinatório e avalia o desempenho de células solares de heterojunção de silício (SHJ) que apresentam essas camadas como contatos elétron-seletivos. Bandgap, condutividade e energia de ativação variaram significantemente entre amostras ricas em Sn e Ge. Quando tais camadas foram aplicadas como contatos elétron-seletivos em células solares, os dispositivos apresentaram baixo desempenho, com resultados surpreendentemente semelhantes apesar de mudanças nas propriedades do material. A partir de análises e modelagem das características corrente-tensão de várias estruturas de células solares, com auxílio de um algoritmo de Evolução Diferencial auto adaptativo, mostramos que a função trabalho do contato elétron-seletivo está em torno de 4.35 eV para todas as composições investigadas de Sn e Ge, o que é muito alto para formar um excelente contato. Através da comparação de diferentes arquiteturas de células solares, identificamos ainda que camadas ricas em Ge impõem uma barreira adicional à extração de elétrons, independentemente de sua baixa seletividade, devido a baixos valores de condutividade. Após a identificação desses mecanismos de perdas, $MgSnN_2$ (MTN) foi considerado como um bom candidato, já que apresenta bandgap adequado e alta concentração de elétrons para uma composição de 50% Mg/(Mg+Sn) (at.%). Desse modo, fabricamos camadas de MTN através de sputtering combinatório, sem aquecimento do substrato e à 200 °C, obtendo amostras de $Mg_xSn_{1-x}N_2$ ($43\% < x < 55\%$), com bandgap em torno de 2 eV, exibindo condutividade e energia de ativação que decrescem em amostras ricas em Mg. Características JV similares àquelas observadas para ZTGN foram obtidas quando MTN foi empregado como camada elétron-seletiva, mas com desempenho ligeiramente superior. As propriedades limitantes foram as mesmas, com função trabalho estimada em 4.16 eV, aumentando para 4.3 eV para amostras fabricadas à 200 °C. Amostras ricas em Sn exibiram ainda alta afinidade eletrônica e aquelas ricas em Mg resultaram em curvas com severo perfil em "s" devido à baixa dopagem, como foi o caso de amostras de ZTGN ricas em Ge. Portanto, a dopagem desses materiais com elementos extrínsecos aparenta ser a abordagem mais relevante para a construção de dispositivos eficientes com contatos formados com camadas de ZTGN ou MTN.

Palavras-chaves: $ZnSnN_2$, $ZnGeN_2$, $MgSnN_2$, contato seletivo, heterojunção de silício, nitretos, células solares, estrutura de banda, meta-heurísticas, extração de parâmetros, evolução diferencial.

Abstract

This work initially reports the electrical characterization of $ZnSn_xGe_{1-x}N_2$ (ZTGN) layers ($10\% < x < 90\%$) deposited on glass by combinatorial sputtering and further assesses the performance of silicon heterojunction (SHJ) solar cells featuring them as electron-selective contacts. Bandgap, dark conductivity, and the activation energy of the latter were found to significantly change between Sn and Ge-rich samples. When applying ZTGN layers as electron-selective contacts for SHJ solar cells, poor solar-cell performance was observed, with surprisingly similar results despite changes in material properties. From analysis and modelling of the current-voltage characteristics of several device structures, through a self-adaptive Differential Evolution algorithm, we show that the work function of the electron-selective contact lies around 4.35 eV for all investigated Sn and Ge contents, which is too high to form an excellent electron-selective contact. By comparing different solar-cell architectures, we could further identify that the Ge-rich layer imposes an additional barrier to electron extraction, independently of its poor selectivity, due to its low conductivity. After having identified these loss mechanisms, $MgSnN_2$ (MTN) was envisioned as a good candidate, due to its high electron concentration and bandgap at 50% Mg/(Mg+Sn) (at.%). Thus, we fabricated MTN layers also through a combinatorial sputtering approach, with no substrate heating and at 200 °C, resulting in $Mg_xSn_{1-x}N_2$ ($43\% < x < 55\%$) samples, with bandgap around 2 eV, showing dark conductivity and activation energy that decreased towards Mg-rich samples. When applied to SHJ solar cells, JV characteristics similar to that when ZTGN was studied were obtained, and performance was slightly better. The limiting properties were also of the same kind, with an estimated work function around 4.16 eV, shifting to 4.3 eV for samples grown at 200 °C, and Sn-rich samples showing a too high electron affinity. Mg-rich samples, as Ge-rich ones, resulted in strong s-shapes due to poor doping. Thus, doping these compounds with extrinsic elements appears as the most relevant approach to build efficient devices with a ZTGN or MTN contact layer.

Keywords: $ZnSnN_2$, $ZnGeN_2$, $MgSnN_2$, carrier-selective contact, silicon heterojunction, nitrides, solar cells, band structure, metaheuristics, parameter extraction, differential evolution.

Contents

1 Introduction

1.1 Silicon Heterojunction solar cells

1.1.1 Theoretical background

Solar cells directly convert sunlight into electricity due to what is known as the photovoltaic effect, first reported by Becquerel in 1839 [1]. In order to efficiently convert sunlight into power, charge carriers, i.e., electron-hole pairs generated by the absorption of light in the absorber must be efficiently collected at the contacts with minimal recombination losses.

Although many solar cell technologies have been developed to address this goal, c-Si solar cells are responsible for around 95% of the PV market [2], due to attractive characteristics, such as high efficiencies, long-term stability and that Si is an Earth-abundant material. Even so, a huge research effort has been carried out in order to approach the maximum theoretical efficiency of 29.43% for crystalline silicon solar cells [3], since even small enhancements in efficiency have significant impacts on the levelized cost of electricity [4].

However, in conventional Aluminum Back-Surface-Field (Al-BSF) solar cells, metal contacts are in direct contact with the silicon surface, which introduces a large density of electronic states into the bandgap, which turns this interface into a huge sink for minority carriers, leading to a strong reduction in the splitting of the quasi-Fermi levels [5], undermining an efficient extraction of light generated charge-carriers.

Passivating contacts, which avoid direct contact between the metal and the silicon absorber without imposing barriers for majority carrier extraction [5], emerged as an alternative to reduce contact and surface recombination losses while enabling an efficient selective charge-carrier extraction [6].

The definition of a passivating contact is closely linked to that of a selective contact. According to Würfel et al., selectivity can be defined as [7]:

> Selectivity is achieved by differences in conductivities of electrons and holes in two distinct regions of the device, which, for one charge carrier, allows transport to one contact and block transport to the other contact.

According to Hermle et al. [5], this definition encompasses all the requirements for a passivating contact: suppression of recombination in the vicinity of the contact, allowing a high internal voltage; constant majority Fermi energy in the contact region at open-circuit conditions, and low resistivity for majority carrier transport.

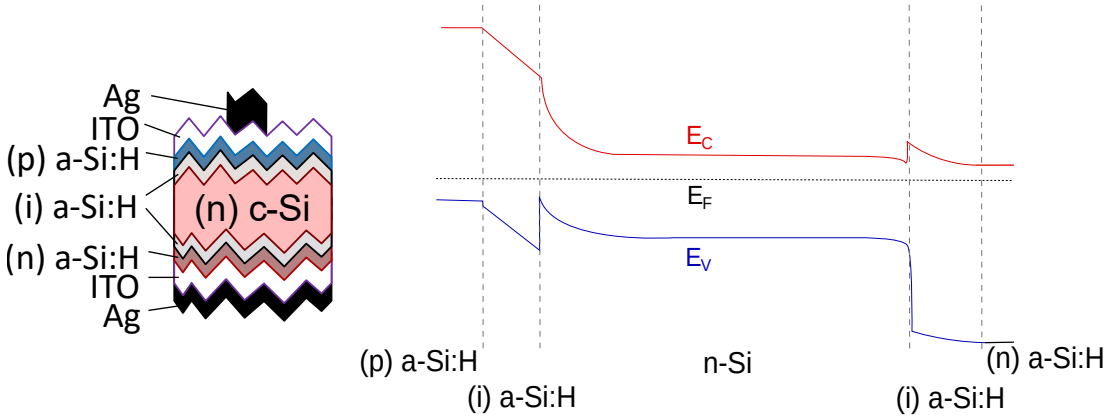

Figure 1.1 – Structure of a front-junction SHJ solar cell (left) with the corresponding (simplified) band diagram in equilibrium (right). E_C, E_F and E_V denote the minimum of the conduction band (CB), the Fermi level and the maximum of the valence band (VB).

The most successful passivating contact structure is the silicon heterojunction (SHJ) solar cell [8], which set in 2017 a new world record for crystalline silicon solar cells efficiency of 26.6% [9]. The SHJ solar cell structure, shown schematically in Fig. 1.1, consists of a crystalline silicon wafer passivated on both sides by intrinsic hydrogenated amorphous silicon — (i) a-Si:H — deposited by PECVD, typically 5–10 nm thick [5], which can neutralize the dangling bonds at the crystalline silicon surface by attaching a hydrogen atom to each dangling bond [10].

Following the (i) a-Si:H deposition, doped (p) and (n) a-Si:H layers (typically 10 nm thick [5]) are deposited on top of the intrinsic layers. These layers, besides providing low resistivity only for majority carriers, suppress minority carrier recombination due to the band offsets with c-Si, as shown in the band diagram of Fig. 1.1. Moreover, due to their higher bandgaps (∼1.7 eV [11]) compared to c-Si, these layers can keep a low minority carrier concentration even when it increases by orders of magnitude at the operating point of a solar cell [7], preventing the flow of minority carriers to the wrong contacts.

Furthermore, suitable doping levels of the a-Si:H layers cause a proper work function matching with c-Si, leading to an induced homojunction at the c-Si surface, which is the case of the (p) a-Si:H/(i) a-Si:H/n-Si interface in Fig. 1.1, which dominates the contact characteristics [5]. In this case, the resulting JV characteristics of the device can be described by the traditional diode theory.

Then, a transparent conductive oxide (TCO), typically ∼80 nm Indium Tin Oxide (ITO), is sputtered on top of the doped a-Si:H layers to provide lateral conductivity, also serving as anti-reflection coating [4]. Ag is then sputtered on the rear and front size to establish contacting, finishing the device processing.

Additionally, the TCO poses more requirements for the doped a-Si:H layers: if

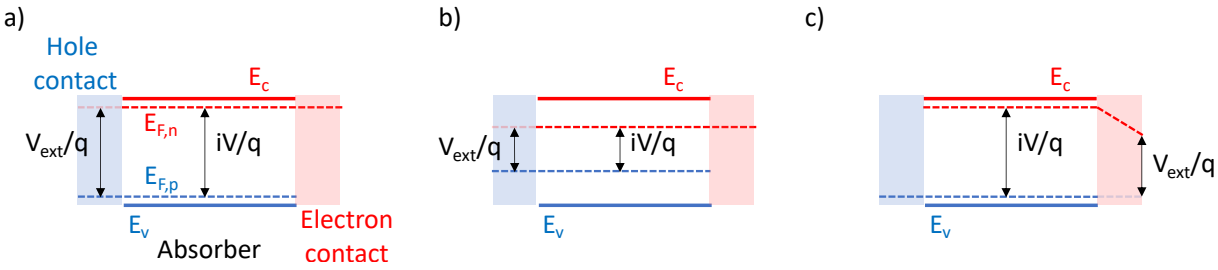

Figure 1.2 – Band diagrams illustrating an ideal voltage extraction from a solar cell (a), where all the implied voltage (iV) generated by the quasi-Fermi level splitting is transferred to the contacts (V_{ext}); a solar cell limited by minority carrier recombination in the absorber, low generation rate, or due to a significant number of extracted carriers (b), where the quasi-Fermi level splitting is lowered, but still transferred to the contacts; and a device where passivation is good but the voltage extraction is limited by a gradient in the electron quasi-Fermi level (c), due to problems to extract the intended majority carrier [5].

their doping levels and thickness are not suitably adjusted, the work function mismatch between the TCO and doped a-Si:H layers can lead to a depletion of the latter at the interface with the TCO due to a Schottky-like junction, lowering the selectivity of the doped a-Si:H layers. On the device level, this effect usually results in FF losses [4, 12].

Overall, if the device is well designed, with contacts selectively extracting their intended charge carrier and promoting excellent passivation of the c-Si surface, the implied voltage generated within the absorber due to light absorption and quasi-Fermi level splitting can be entirely extracted from the device in the ideal case, shown in Fig. 1.2 (a). In this case, the maximum voltage extracted from the device matches the implied voltage, which is limited only by inherent silicon recombination processes.

On the other hand, if the device is limited by minority carrier recombination, the quasi-Fermi level splitting is reduced but can still be extracted from the device, as shown in Fig. 1.2 (b). However, when a contact fails to extract its intended majority carrier due to transport losses, the corresponding quasi-Fermi level will drop within the contact, strongly reducing the voltage that can be extracted from the device, even though the implied voltage is still high. This situation is shown in Fig. 1.2 (c), in which a gradient in the quasi-Fermi level in the electron contact can be seen.

In highly efficient SHJ solar cells, where recombination losses are mainly due to the c-Si wafer, open-circuit voltages as high as 750 mV can be extracted from the device, which is close to the upper limit defined by c-Si [3]. Besides enabling high efficiencies, additional benefits of the silicon heterojunction solar cell technology include low temperature processing ($< 200\,°C$), stability and better performance at high temperatures [5].

Nevertheless, important bottlenecks are still present, such as parasitic absorption

in the a-Si:H layers, which can also be damaged by the sputtering of the TCO, leading to enhanced recombination that lowers V_{oc} [4, 8]. These issues have motivated an increased research for new materials that could replace the a-Si:H layers in SHJ solar cells, enabling better properties, such as higher transparency, lower defect densities, doping efficiency, and also even more suitable work functions [13].

The next section reviews some works addressing the search for new materials as passivating contacts.

1.1.2 Novel contacts for SHJ solar cells: state of research

As previously discussed, novel passivating-contact schemes are actively being investigated. In [14], a hole-selective contact scheme for n-type SHJ solar cells based on MoO_x thin films was proposed. The results showed that a power conversion efficiency of 18.8% was obtained through the insertion of an intrinsic a-Si:H passivation layer between the oxide contact and silicon absorber, MoO_x/a-Si:H/c-Si.

Furthermore, this cell architecture was subjected to I-V measurements as a function of temperature in the range 25–60 °C under the AM1.5G spectrum to better understand the "s-shaped" profile of the I-V curves observed at higher voltages. It was found that this profile straightened out at higher temperatures, indicating a thermionic emission barrier that must be overcome by holes.

The first demonstration of highly efficient devices with MoO_x based hole collector was carried out in [15]. The SHJ solar cell, with the p-type amorphous silicon film replaced by a MoO_x layer as hole collector in front of the SHJ solar cell achieved a certified efficiency of 22.5%, proving that metal oxide layers can be used as a replacement for p-doped amorphous silicon layers in highly efficient devices.

In [16], I-V measurements were carried out at several irradiance levels for a solar cell with a-Si:H, TiO_2 and Al electrode. It was seen that this cell architecture showed an increase in V_{oc} for decreased illumination, indicating that this contact scheme achieves better charge-carrier selectivity at low illumination.

In reference [17], intrinsic amorphous silicon oxide (i a-SiO_x:H) was compared with a standard a-Si:H to assess its potential as buffer and window layer on the front side. The solar cell with intrinsic a-SiO_x:H showed a slightly lower absolute value for the relative change in V_{oc}, -0.22%/°C compared to -0.25%/°C obtained for the cell using a-Si:H. Therefore, if the cell will operate at elevated temperatures, the cell with intrinsic a-SiO_x:H may be employed. Considering that in field conditions the working temperature is in general far above room temperature, this design has a promising potential, especially for warmer climates.

Recently, a 21.3 %-efficient crystalline silicon solar cell was demonstrated in [18],

by using a ZnO/LiF_x stack (on top of a passivating intrinsic a-Si:H) as electron-selective contact. In [19], an electron selective contact for crystalline silicon solar cells based on TaN_x was proposed, achieving a power conversion efficiency over 20%.

In [20], p-type microcrystalline silicon was investigated as electron-selective contacts for SHJ solar cells. With reduced deposition temperatures, $< 200\,°C$, the performance of this cell architecture was improved due to mitigated parasitic light absorption and enhanced hole extraction, achieving an efficiency of 23.45%. Moreover, variable-temperature I-V measurements were carried out to investigate the effect of low temperature deposition on charge extraction. For cells with deposition at lower temperatures, the fill factor exhibited an improvement for reduced cell temperatures, while for a cell with deposition at 200 °C, the FF improved for higher operating temperatures.

In [21], a dopant-free asymmetric heterocontact, employing a LiF_x/Al outer stack for electron extraction and standard SHJ sunward-hole contact, was tested with thin oxide protective layers to improve the stability of the contact. Four oxides were tested: TiO_x, Ta_2O_x, HfO_x and Al_2O_x, and the results showed that the thermal stability of electron-selective heterocontacts can be improved by using a TiO_x layer between the a-Si:H passivation layer and the LiF_x/Al electrode. The I-V characteristics extracted under STC showed an efficiency of 20.7%, the highest up to date obtained by this kind of cell technology.

Moreover, it has been recently shown in [22] that, for hole-selective contacts, their thickness, doping and valence band mismatch with c-Si strongly influence the FF on the device level, whereas V_{oc} would be more affected by interfacial defect density.

As seen in this literature review, deviations from the classical diode theory can occur when new materials are studied as selective contacts: the superposition principle no longer holds, resulting in anomalous I-V curves that exhibit features known as “s-shapes”, that are now often reported in the literature.

Nevertheless, the reasons for this behavior are not totally clear, since the underlying physics of passivating-contact solar cells is still not fully understood and it is difficult to generalize theories, given that in these technologies the device construction involves diverse materials that introduce many interfaces hampering charge flow.

1.2 Objectives

In the search for new materials as passivating contacts for SHJ solar cells, ternary nitrides have emerged as potential candidates due to their compelling properties for heterojunction solar cells, such as high carrier concentration and wide bandgaps, which can even be tuned upon changes in stoichiometry. Moreover, these materials are all composed

of Earth-abundant materials, making them specially interesting for PV applications.

Yet, this is still a vastly unexplored research area, with few works reporting the application of these materials as passivating contacts for SHJ solar cells, despite representing an excellent opportunity for an extensive study about contact selectivity, since their electronic properties strongly depend on stoichiometry.

In this sense, the goal of this work is to assess the suitability of $ZnSn_xGe_{1-x}N_2$ and $Mg_xSn_{1-x}N_2$ semiconductors as electron-selective contacts for silicon heterojunction solar cells, given the variable electron concentration and bandgaps shown by these materials, depending only on composition, making them an excellent platform to investigate the underlying properties of carrier selectivity in solar cells. It will be shown that these compounds can experimentally reveal critical phenomena that must be accounted when designing selective contacts, leading to a better understanding of the limiting properties of SHJ solar cells.

1.3 Structure of this work

In an effort to make comprehensive, stand-alone chapters, information about experimental and analysis methods will be introduced when needed.

As it will be necessary to carry out an extensive parameter extraction from I-V data to model the electrical performance of the fabricated solar cells and understand the limiting properties of devices featuring nitride semiconductors as carrier-selective contacts, this work firstly addresses the PV parameter extraction problem, targeting metaheuristics algorithms. Selected algorithms, with simple implementation, will be reviewed, and their performance and accuracy on the extraction of diode parameters from a benchmark, noise-free, and noisy I-V curves will be discussed in Chapter 2.

Chapter 3, which is the bulk of this work, addresses the application of nitride semiconductors, namely $ZnSn_xGe_{1-x}N_2$ semiconducting alloys and $Mg_xS_{1-x}N_2$, as carrier-selective contacts in SHJ solar cells, presenting basic material fabrication by a combinatorial sputtering approach and results from electro-optical characterization. Through an extensive characterization of several architectures of SHJ solar cells, with subsequent modelling of the resulting I-V data aided by a metaheuristic algorithm studied in Chapter 2, it will be shown how this device-oriented approach can reveal critical phenomena that must be accounted for when considering new materials as selective contacts. Finally, Chapter 4 reviews the achievements of this work and discusses prospects.

2 Stochastic optimization algorithms applied to the PV parameter extraction problem

This chapter is based on the following publication: Fébba, D. M. et al. The effects of noises on metaheuristic algorithms applied to the PV parameter extraction problem. Solar Energy, v. 201, p. 420-436, 2020 [23].

2.1 Motivation

The most important information about a solar cell electrical behavior, such as short-circuit current I_{sc}, open-circuit voltage V_{oc}, maximum power point P_{mpp}, can be extracted from its current-voltage (I-V) characteristics (or I-V curves) and by analyzing its equivalent circuit [24]. From this analysis, other important parameters such as series R_s and shunt R_{sh} resistance, diode ideality factor n and reverse saturation current I_0 may also be obtained, providing valuable information about the electrical performance of solar cells and modules.

There are many mathematical models in the literature describing the I-V characteristics of solar cells, such as single, double and triple diode models [25]. However, due to its simplicity and accuracy, the single-diode model with series and shunt resistance is the most used one [26]. According to this model, the output current I as a function of voltage V across the solar cell terminals is given by Eq. (2.1):

$$I = I_{ph} - I_0 \left[e^{q(V+IR_s)/nkT} - 1 \right] - \frac{V + IR_s}{R_{sh}}, \tag{2.1}$$

where k is the Boltzmann constant, q is the elementary charge, and T is the absolute temperature.

Extracting the five diode parameters, i.e., the photocurrent I_{ph}, diode reverse saturation current I_0, diode ideality factor n, series and shunt resistance R_s and R_{sh}, respectively, from Eq. (2.1), is not a simple task and finding the best extraction method remains a challenge, which has attracted the attention of researchers and produced many manuscripts in recent years, given the importance of this problem to evaluate and compare the performance and characteristics of new devices, as well as to improve power output prediction [27].

Methods for extracting the diode parameters from I-V curves can be essentially grouped into two main categories: analytical and numerical [27]. Within numerical methods, metaheuristic algorithms constitute powerful tools for the solar cells parameter ex-

traction problem, since they do not rely on any prior knowledge about specific points of the I-V curve, such as I_{sc}, V_{oc}, P_{mpp}, or slopes at these regions, which are usually required for analytical methods [28], nor they rely on initial conditions or fitting algorithm, which are required for numerical techniques that employ iterative methods [29].

The literature is vast regarding parameter extraction techniques, as can be seen in recently published reviews [25, 30, 31]. However, manuscripts addressing the problem of how parameter extraction methods are influenced by noise levels present on solar cells I-V curves are rather scarce, and even scarcer regarding metaheuristic algorithms. This is an important issue because solar cells I-V curves generally have some noise level due to light variation during the measurement process, which is present in any I-V measurement system for PV devices since light generation is a spatiotemporal stochastic process [32]. In this sense, it is important to evaluate how different noise levels affect the parameter extraction procedure.

In this sense, considering that metaheuristic algorithms are increasingly being applied to PV parameter extraction problem, as seen in the aforementioned reviews, the aim of this work is to compare four metaheuristic methods according to the accuracy of the obtained results for a benchmark, noise-free and noisy solar cell I-V curves, considering the single-diode model.

We intend to identify how would the algorithms perform under noisy I-V characteristics and identify the most reliable and robust ones against noise as well. Moreover, the majority of works dealing with metaheuristics for the PV parameter extraction problem employ the RMSE as the objective function [31], and do not consider the effects of other functions on the extracted parameters. Therefore, in this work four different objective functions were considered: the RMSE, MAPE, MAE and Huber loss function, to evaluate how the objective function affects the extracted single-diode parameters under different noise levels.

The compared algorithms, chosen among many others due to their promising results found in the literature, are the Self-Adaptive Differential Evolution (DE) algorithm, proposed by [33], the Performance Guided JAYA algorithm (PGJAYA), proposed by [34], the Self-Adaptive Teaching-Learning-based optimization (SATLBO) algorithm, proposed in [35], and the Biogeography-based Heterogeneous Cuckoo Search algorithm (BHCS), proposed by [36]. None of these methods were studied considering their performance on the PV parameter extraction problem when noisy scenarios are taken into consideration.

2.2 Problem formulation

The extraction of the single-diode parameters from Eq. (2.1) can be converted into an optimization problem by defining and minimizing an objective function (or cost

function), which is essentially the error between the estimated and experimental data. In general, for metaheuristic algorithms, a search mechanism tries to find the best solution among a set of possible solutions, i.e., the objective is to find the solution that provides the minimum value for the objective function.

For the single-diode parameter, each possible solution is of the form:

$$X = (I_{ph}, I_0, R_s, n, R_{sh}), \tag{2.2}$$

and the most widely used objective function for the PV parameter extraction problem is the Root Mean Square Error (RMSE), as stated by the review works mentioned in section 1.

The RMSE is defined by Eq. (2.3):

$$RMSE = \sqrt{\frac{1}{N}\sum_{i=1}^{N}(I_{i,exp} - I_{i,est})^2}, \tag{2.3}$$

where N is the number of data points, $I_{i,exp}$ is the ith experimental current point and $I_{i,est}$ is the ith estimated current point by the search algorithm, being a function of X_i. Thus, for a given temperature T, $I_{i,est} = I_{i,est}(I_{i,ph}, I_{i,0}, n_i, R_{i,s}, R_{i,sh}, V_{i,exp}, I_{i,exp})$. The RMSE is a measure of the fitness quality between the estimated and experimental points, and for a good fitting, its value should be minimized, which is accomplished by the search procedure implemented by the optimization algorithm.

However, since the aim of this work is to investigate the influences of noises on the selected algorithms, and considering that the results may depend on the cost function which is minimized by the search algorithm, three other cost functions will be considered: the Huber loss function, the Mean Average Percentage Error (MAPE) and the Mean Average Error (MAE). The minimization of the Huber function is achieving by minimizing Eq. 2.4:

$$Huber = \frac{1}{N}\sum_{i=1}^{N}\rho_i, \tag{2.4}$$

where

$$\rho_i(r) = \begin{cases} r_i^2/2 & \text{if } |r_i| \leq c\ , \quad (2.5a) \\ c(|r_i| - c/2) & \text{otherwise,} \quad (2.5b) \end{cases}$$

In Eqs. 2.5a and 2.5b r is the residual between an experimental and estimated point and c is a tuning parameter, chosen as 1.345 [37, 38] in this work. The MAPE and

MAE are define by Eqs. 2.6 and 2.7, respectively.

$$MAPE = \frac{1}{N}\sum_{i=1}^{N}\left|\frac{I_{i,exp} - I_{i,est}}{I_{i,exp}}\right| \tag{2.6}$$

$$MAE = \frac{1}{N}\sum_{i=1}^{N}|I_{i,exp} - I_{i,est}| \tag{2.7}$$

Therefore, the results will be compared considering these four objective functions. This will be important since no study was previously carried out to evaluate the effects of the objective function on the performance of the algorithms considered in this work for the PV parameter extraction problem.

2.3 Review of the metaheuristic algorithms under study

2.3.1 Self-adaptive Differential Evolution

The Differential Evolution (DE) algorithm, first introduced by [39], is a population-based stochastic function optimization algorithm [40], which optimizes a function by following evolutionary rules. It is a powerful tool to find the global minimum of non-linear and multi-modal functions [41], and is among the most popular evolutionary algorithms currently in use due to its simplicity and efficiency [42], being widely employed to the solar cell parameters extraction problem [43].

The DE algorithm has four stages: initialization, mutation, recombination, and selection. In the first stage, a set of NP individuals is randomly initialized to form the initial population, which will evolve through G generations or until some criteria is achieved. Each individual $X_i = X_i\left(I_{ph}, I_0, R_s, n, R_{sh}\right)$ is a candidate to the optimum solution that minimizes the objective function f. A possible scheme for the population initialization is

$$X_{i,j}^{G=1} = X_L^{G=1} + rand_{i,j}(0,1)\left(X_U^{G=1} - X_L^{G=1}\right), \tag{2.8}$$

where the index i goes from 1 to NP (population size), the index j goes from 1 to 5 (since the vector X has five components for the problem under study), X_L and X_U are the lower and upper bounds for the individuals, respectively, and define what is called the search space. Here, $rand_{i,j}(0,1)$ denotes a random number between 0 and 1 with uniform probability distribution. The superscript G denotes the generation number, running from 1 to the maximum iterations number G_{max}.

In the second stage, called mutation, a *donor vector* is formed. For that, there are several different strategies in DE literature [42], and in this work, the current-to-best/1

strategy will be employed. A donor vector V_i^G can be written as:

$$V_i^G = X_i^G + F\left(X_{best}^G - X_i^G\right) + F\left(X_{r1}^G - X_{r2}^G\right), \tag{2.9}$$

where, at generation G, X_i^G denotes the current individual, X_{best}^G is the best individual, i.e., the individual with the minimum value for the objective function, and X_{r1}^G and X_{r2}^G are randomly chosen individuals, different from each other and from the current individual X_i^G. Also, F ($F \in [0, 2]$) is a real number, user defined, called *mutation factor*.

In the final stage, called recombination (or crossover) the donor vector is mixed with the target vector X_i^G, yielding a *trial vector* U_i^G. For that, there are two common schemes: binary and exponential crossover [41]. In this work, the binary scheme will be used and it is described by:

$$U_{i,j}^G = \begin{cases} V_{i,j}^G & \text{if } rand(0,1)_j \leq \text{CR or } j = j_{rand}\ , \quad (2.10a) \\ X_{i,j}^G & \text{otherwise,} \quad (2.10b) \end{cases}$$

where $V_{i,j}^G$ is the donor vector, j_{rand} is a randomly integer chosen in the interval $[1, 5]$ and CR ($CR \in [0, 1]$) is another real number, user defined, known as *crossover rate*.

Finally, after recombination, the selection stage occurs. The trial and target vectors are compared, and the vectors that minimize the objective function are selected to the next generation, i.e.,

$$X_i^{G+1} = \begin{cases} U_i^G & \text{if } f(U_i) < f(X_i)\ , \quad (2.11a) \\ X_{i,j}^G & \text{otherwise.} \quad (2.11b) \end{cases}$$

However, in its standard form, as described above, the performance of the DE algorithm is highly dependent on the user-defined variables F and CR [40, 43, 44] and, moreover, there is no general rule for a suitable choice of these parameters for a given problem [45]. To deal with the problem-dependent tuning of DE control parameters, many self-adaptive DE variants have been proposed [41]. In this work, the self-adaptive control parameters proposed by [33] will be employed.

This method was tested on twenty-one benchmark functions and it was found to be better or at least comparable to the standard DE algorithm and other evolutionary algorithms from literature considering the quality of the solutions [33]. According to this work, the mutation factor is adjusted as:

$$F_i^{G+1} = \begin{cases} F_l + rand_1 F_u & \text{if } rand_2 < \tau_1, \quad (2.12a) \\ F_i^G & \text{otherwise,} \quad (2.12b) \end{cases}$$

whereas the crossover rate is adjusted as:

$$CR_i^{G+1} = \begin{cases} rand_3 & \text{if } rand_4 < \tau_2, \quad (2.13a) \\ CR_i^G & \text{otherwise.} \quad (2.13b) \end{cases}$$

Here, $rand_k$ with $k = 1, 2, 3, 4$ are four random numbers chosen with uniform probability distribution in the interval $[0, 1]$. τ_1 and τ_2 represent the probabilities to adjust F and CR and are set as $\tau_1 = \tau_2 = 0.1$ and, considering $F_l = 0.1$ and $F_u = 0.9$, the new generated F always takes a value from the interval $[0.1, 1]$, and CR from $[0, 1]$.

Furthermore, various values for τ_1 and τ_2 were tested and any significant difference in results was found. Therefore, the problem of tuning the DE control parameters is eliminated, since they are randomly initialized and are automatically adapted during the optimization routine.

2.3.2 Performance Guided JAYA

Based on the concept that the solution for an optimization problem should move towards the best and avoid the worst solution, the JAYA (a word deriving from the Sanskrit meaning victory) was introduced in 2016 by [46].

The original JAYA algorithm has a very simple implementation. Let X_{best} and X_{worst} be the best and worst solution at each iteration, respectively. Based on that, each possible solution (or individual, in the language of evolutionary algorithms) is updated as:

$$X_{i,j} = X_{i,j} + rand_1 \left(X_{best,j} - |X_{i,j}| \right) - rand_2 \left(X_{worst,j} - |X_{i,j}| \right), \quad (2.14)$$

where the index i denotes the individual (possible solution) and j each individual's component; $rand_1$ and $rand_2$ are two distinct random numbers in the interval $[0, 1]$ generated from a uniform probability distribution.

If the updated new solution provides a lower value for the objective function, the new solution is accepted; otherwise, the previous solution is maintained. This process continues until the maximum number of iterations is reached.

This algorithm was tested on 24 constrained and on 30 unconstrained benchmark functions, and the results compared with well-established optimization algorithms. The results showed that the proposed JAYA algorithm had a satisfactory performance for both kinds of optimization problems.

The main problem with this algorithm, as stated by [34] is that the search procedure, given by (2.14), may lead to a population stagnation, which undermines the exploration ability. As a strategy to enhance the performance of the standard JAYA algorithm,

promoting a better balance between exploitation and exploration, and make the algorithm more suitable to the PV parameter extraction problem, [34] proposed the Performance Guided JAYA (PGJAYA).

In this algorithm, an initial population is initialized, in a scheme such as the one given by Eq. (2.8), and for each iteration, the population is sorted in ascending order with respect to the RMSE values, and each individual is ranked according to:

$$R_i = NP - i, \tag{2.15}$$

where $i = 1, 2, ..., NP$, and a probability is assigned to each individual:

$$P_i = \left(\frac{R_i}{NP}\right)^2. \tag{2.16}$$

In this way, better individuals, i.e., individuals with lower values for the objective function will have a higher probability, since for these individuals the R_i value is higher. Initially, or each individual, a random number ($rand_0$) in the range $[0, 1]$ is generated from a uniform probability distribution, and if this number is greater than the probability of the individual, a search strategy aiming at enhancing the exploitation ability is implemented and a new individual is created:

$$X_{i,j}^{new} = X_{i,j} + rand_1 \cdot (x_{best,j} - |X_{i,j}|) - w * rand_2 \cdot (x_{worst,j} - |X_{i,j}|), \tag{2.17}$$

where $rand_1$ and $rand_2$ are again random numbers within $[0, 1]$ with uniform probability distribution, and w is a weight defined as:

$$w = \begin{cases} f(X_{best})/f(X_{worst}) & \text{if } X_{worst} \neq 0, \quad (2.18a) \\ 1 & \text{otherwise}, \quad (2.18b) \end{cases}$$

to optimize the search for the optimal region at early stages of the process.

However, if $P_i \leq rand_0$, a search strategy aiming at exploration ability is implemented. For that, two individuals, different from the current individual, are selected considering their probability P defined by Eq. (2.16), and a new individual is formed:

$$X_{i,j}^{new} = X_{i,j} + rand\left(X_{l,j}^{P_l} - X_{m,j}^{R}\right), \tag{2.19}$$

with $i \neq l \neq m$.

If a random number ($rand_3$) is greater than P_l, another individual X_l is selected until $rand_3 \leq P_l$. Therefore, if X_l is an individual with a low value for the objective function, it has a high probability P_l and the chance of $rand_3 > P_l$ is low, but if it

happens, the random number in Eq. (2.19) has a high value, and therefore the search is directed towards a better region.

Furthermore, a self-adaptive chaotic perturbation was added to find a better solution around the current best solution for replacing the worst one [34]. In this way, a logistic map was implemented:

$$z_k = 4z_k\left(1 - z_k\right), \tag{2.20}$$

where z_k is the value of the kth chaotic iteration and z_0 is a random number in the interval $[0, 1]$. Then, if $rand < 1 - G/G_{max}$:

$$X_j^* = X_{best,j} + rand(2z_k - 1). \tag{2.21}$$

If not, $X_j^* = X_{best,j}$. The new individuals formed by Eqs. (2.17), (2.19) and (2.21) survive to the new generation (iteration) if, and only if, the new individual provides a lower RMSE value. This whole process is then repeated until the maximum number of iterations, G_{max} is reached.

The results obtained by employing PGJAYA to the PV parameter extraction problem were considered competitive when compared with other state-of-art optimization algorithms [34]. Since it has a simple implementation and just only one user-defined parameter, this algorithm constitutes an interesting option for extracting the single and double diode parameters from solar cells and modules.

2.3.3 Self-adaptive Teaching-Learning-based Optimization (SATLBO) algorithm

The SATLBO algorithm was proposed by [35] as a modification to the Teaching-Learning-based Optimization (TLBO) algorithm, proposed by [47], aiming at enhancing the population diversity and search capabilities by considering the fitness of each individual.

The SATLBO, and therefore the TLBO algorithm, was inspired by the influence of a teacher on the learners [47]. Each possible solution is called a learner and, at each iteration, the learner with the minimum value for the objective function is called the teacher.

Initially, a set of possible solutions is created as given by Eq. (2.8) and this initial population is ranked according to the value for the objective function of each individual, just like the ranking employed by the PGJAYA, given by Eq. (2.15). Then, a probability

is assigned to each individual:

$$P_i = 0.5 \left[1 - \cos \left(\frac{R_i \pi}{NP} \right) \right]. \tag{2.22}$$

Based on this probability, the learners (individuals) select the learning phases in a self-adaptive way. If

$$rand \geq P_i, \tag{2.23}$$

where $rand$ is a random number in the interval $[0, 1]$ from a uniform probability distribution, a teacher phase, which is focused on improving the mean result of the class, is implemented. Otherwise, a learner phase, which focuses on enhancing the learners' diversity, is implemented.

In the SATLBO algorithm, two learning strategies for the teacher phase were implemented based on the current iteration number. If $rand \leq 1 - G/G_{max}$, the teacher phase strategy of the original TLBO algorithm is employed:

$$X_i^{new} = X_i + rand \cdot (X_{teacher} - T_F \cdot Mean), \tag{2.24}$$

where $T_F = round\,(1 + rand)$ and

$$Mean = \frac{1}{NP} \left(\sum_{i=1}^{NP} X_{i,1}, \ldots, \sum_{i=1}^{NP} X_{i,5} \right). \tag{2.25}$$

Otherwise, an elite learning strategy is employed:

$$X_i^{new} = X_{teacher} + rand \cdot (X_{teacher} - X_i), \tag{2.26}$$

where $X_{teacher}$ is the individual with the minimum RMSE value at the current iteration. In this way, the learners approach the best region during the early stages and, at later stages, the teacher is improved through a local search [35].

If the condition of Eq. (2.23) is not fulfilled, the learner phase of SATLBO is implemented. In this phase, for each individual (learner), another learner X_k is selected. Then, if

$$f(X_k) \leq f(X_i), \tag{2.27}$$

a new individual is generated through

$$X_i^{new} = X_i + rand \cdot (X_k - X_i). \tag{2.28}$$

Otherwise, two other learners X_{r1} and X_{r2}, with $X_{r1} \neq X_{r2} \neq X_i$ are randomly selected and used to generate a mutant vector. If $RMSE(X_{r1}) < RMSE(X_{r2})$,

$$V_i = X_j + rand \cdot (X_{r1} - X_{r2}) . \tag{2.29}$$

Otherwise,

$$V_i = X_j + rand \cdot (X_{r2} - X_{r1}) . \tag{2.30}$$

Then, a crossover operation is implemented, generating a new individual:

$$X_{i,j}^{new} = \begin{cases} X_{i,j} & \text{if } rand_1 < rand_2, \quad (2.31a) \\ V_{i,j} & \text{otherwise}, \quad (2.31b) \end{cases}$$

enhancing the population diversity. The new individual generated by the teacher phase or learner phase is accepted, i.e., goes to the next iteration, if, and only if, it reduces the RMSE value. This whole process continues until the maximum number of iterations is reached.

This algorithm was employed to the PV parameter extraction problem by [35], and it was found to be better than other considered algorithms. More details about the SATLBO algorithm and pseudo-code can be found in the work of [35] and [47].

2.3.4 Biogeography-based Heterogeneous Cuckoo Search algorithm (BHCS)

The hybrid metaheuristic algorithm called Biogeography-based Heterogeneous Cuckoo Search (BHCS) combines both explorations of cuckoo search (CS) and exploitation of Biogeography-based optimization (BBO) [36]. Both CS and BBO are meta-heuristic algorithms. The CS is inspired by the behavior of the female cuckoo which lays its eggs in nests of other birds. Each host bird egg represents a solution and a cuckoo egg represents a new candidate solution. The BBO is inspired by island biogeography science, where each solution is considered a habitat with a habitat adequacy index, which is used to measure the quality of the individual. The BHCS has two stages of optimization that are described below:

1. In the first stage the CS is based on the Levy flight to generate new solutions, which is good for exploring the wide area [48]. The update rules are

$$x_i^{G+1} = \begin{cases} x_i^G + \alpha(x_i^G - x_g) \oplus \text{Levy}\beta & \frac{2}{3} < r \leq 1, \\ \bar{x} + \delta \ln(\frac{1}{\eta})(\bar{x} - x_i^G) & \frac{1}{3} < r \leq \frac{2}{3}, \\ x_i^G + \delta \exp(\eta)(x_g - x_i^G) & else, \end{cases}$$

where $NP$is the population size, x_g is the best solution in current the iteration, $\bar{x}$ is the mean of all NP solutions, r and η are random numbers in the interval [0,1].

2. In the second stage, the host bird can discovery alien eggs with a probability pa, then abandon old nests and generate new ones based on the biogeography-based migration operator [49]. For this, the population is sorted from best to worst, and each solution is assigned with emigration rates μ

$$\mu_i = E\frac{S_i}{NP}, \tag{2.32}$$

where $E = 1$ is the maximum emigration rate and $S_i = NP - i$ is the number of species in the solution.

In this manuscript were adopted the values presented in [36] for the parameters $pa = 0.3$, $\alpha = 1.1$, $\delta = 1.6$ and $E = 1$.

The results obtained by the BHCS method in the extraction of PV parameters were considered competitive when compared with other optimization algorithms [36]. Thus, this algorithm is an interesting option for extracting the single and double diode parameters from solar cells I-V curves.

2.4 Generation of noisy I-V curves and computational procedures

In order to study the effects of noisy current measurements on the accuracy of the results provided by the optimization algorithms, artificial I-V curves were computationally generated through the Lambert W-function. If the five single-diode parameters and voltage points are known, the current points can be calculated for a given temperature T through Eq. 2.33 [50]:

$$I = -\frac{nkT}{qR_s} LambertW\left\{\frac{qR_sI_0R_{sh}}{nkT(R_s+R_{sh})}\exp\left[\frac{qR_{sh}(R_sI_{ph}+R_sI_0+V)}{nkT(R_s+R_{sh})}\right]\right\} - \frac{V}{R_s+R_{sh}} + \frac{R_{sh}(I_0+I_{ph})}{R_s+R_{sh}}. \tag{2.33}$$

In this way, it is possible to simulate I-V curves with arbitrary values for the single-diode parameters for a given voltage interval and temperature condition. To simulate noisy and noise-free I-V curves, the five parameters were chosen from the work of [51], since they reproduce with a high degree of accuracy the I-V curve of a commercial 57 mm diameter RTC France solar cell under 33 °C and 1000 W m^{-2} provided by [52], which is widely used in literature as a benchmark curve for parameter extraction methods [31]. The I-V points of this benchmark curve are given in Table 2.1.

Table 2.1 – I-V curve points of a 57 mm diameter commercial (R.T.C. France) silicon solar cell under 33 °C and 1000 W m^{-2} provided by [52].

Point	Voltage (V)	Current (A)	Point	Voltage (V)	Current (A)
1	-0.2057	0.7640	14	0.4137	0.7280
2	-0.1291	0.7620	15	0.4373	0.7065
3	-0.0588	0.7605	16	0.459	0.6755
4	0.0057	0.7605	17	0.4784	0.6320
5	0.0646	0.7600	18	0.496	0.5730
6	0.1185	0.7590	19	0.5119	0.4990
7	0.1678	0.7570	20	0.5265	0.4130
8	0.2132	0.7570	21	0.5398	0.3165
9	0.2545	0.7555	22	0.5521	0.2120
10	0.2924	0.7540	23	0.5633	0.1035
11	0.3269	0.7505	24	0.5736	-0.010
12	0.3585	0.7465	25	0.5833	-0.123
13	0.3873	0.7385	26	0.59	-0.210

The single-diode parameters for all simulated I-V curves considered in this work are: $I_{ph} = 0.7608\,\text{A}$, $I_0 = 3.223 \times 10^{-7}\,\text{A}$, $n = 1.4808$, $R_s = 0.036\,768\,\Omega$ and $R_{sh} = 57.746\,14\,\Omega$. The voltage points were chosen to vary from $-0.2\,\text{V}$ to $0.609\,\text{V}$ in steps of 1 mV and, for each voltage point, a current point was generated according to Eq. (2.33). The temperature was set at 33 °C, since this is the temperature condition for the benchmark curve.

This procedure generates a clean I-V curve, i.e., noise-free. Therefore, an artificial random noise was added to each current point according to the approach proposed by previous studies that considered the effect of noise on diode [53, 54] and solar cells I-V curves [55–57], as given by Eq. (2.34):

$$I_{noise} = I\,(1 + NL \cdot rand)\,, \tag{2.34}$$

where NL is the noise level and $rand$ is a random number in the interval $[-1, 1]$, with a uniform probability distribution. In this study, besides the noise-free I-V curve, six different noise levels (% of the current values) were considered: 0.001, 0.01, 0.1, 1, 5 and 10 %. Since the noise is essentially a set of random numbers, 10 noisy I-V curves were generated for each noise level, allowing a statistical assessment of the performance of the algorithms according to the noise level.

The advantage of this approach is that it is possible to guarantee that a method has converged or not to the global optimum, since each single-diode parameter is known, and evaluate the performance of the algorithms also in terms of relative errors between the global optimum parameters and the ones that were effectively extracted. In this way, it is possible to identify the most affected parameters according to the noise level. Furthermore,

considering that the optimization methods in this work are stochastic processes, 40 runs were executed for each I-V curve.

Given the computational effort, the optimization routines were executed in the Giskard High-Performance Computing Cluster at the Federal University of Itajubá, which is equipped with 6 computational nodes, each being composed of forty 2.20 GHz CPUs and 94.57 GB of RAM. All algorithms were implemented in Python 3 using the multiprocessing library, which easily allows code parallelization. Therefore, in each computational node, 40 simultaneous runs were executed.

To maximize the possibility that for each run the algorithm would start at different points, the system time was used as the random seed at the beginning of each run, which means that for every initialization a different sequence of random numbers was created. For all algorithms the same penalty function defined for the Self-Adaptive DE algorithm was implemented, to guarantee that the searched values would remain inside the search interval, defined in Table 2.2, for all I-V curves considered in this work.

Table 2.2 – Minimum and maximum allowed single-diode parameters, defining a search interval that was applied to all algorithms.

	I_{ph} (A)	I_0 (µA)	n	R_s (Ω)	R_{sh} (Ω)
Min	0	0	1	0	0
Max	1	1	2	0.5	100.0

Initially, all algorithms were tested and evaluated on the aforementioned benchmark curve, to provide comparisons with the works where they originally published, and with other algorithms that were tested on this same curve. For a better assessment of the performances of these algorithms, three different population sizes were considered for the benchmark curve: 20, 50 and 100 individuals; for the BHCS algorithm, the additional control parameters required by it were taken from its original manuscript.

Furthermore, all algorithms were allowed to reach 50,000 iterations. Then, the algorithms were tested on the noise-free and noisy I-V curves considering the population size that provided a good trade-off between the required execution time and quality of the results on the benchmark curve. Also, the maximum number of iterations was reduced to 20,000 when the algorithms where applied on the noise-free and noisy I-V curves to alleviate the computational burden.

The results for the benchmark curve were compared in terms of minimum, maximum, standard deviation, mean and median of the RMSE values obtained considering the 40 runs since the RMSE is the metric used for evaluating algorithms on this benchmark curve. Also, comparisons were made in terms of execution time, best and worst runs, defined as the minimum and the maximum number of iterations for achieving convergence, success rate (SR), defined as the number of runs that converged divided by the total

number of runs [58]. Since an RMSE of 9.86022E-04 is a commonly reported value for the benchmark curve, as seen in the reviews mentioned in the literature review, an algorithm was considered to converge when the RMSE was lower than 9.86023E-04.

Considering the noise-free and noisy I-V curves, the accuracy of the single-diode parameters extracted by the studied algorithms, considering the four different objective functions, was assessed in terms of the Absolute Relative Error, since the expected parameters were previously known. The Absolute Relative Error (%) is defined as the absolute value of the relative error, as given by Eq. (2.35):

$$|Relative\,Error| = 100 \cdot \left| \frac{P_{target} - P_{extracted}}{P_{target}} \right|, \tag{2.35}$$

where P_{target} denotes the expected parameter and $P_{extracted}$ is the parameter extracted from the I-V curve.

2.5 Results and discussion

2.5.1 Benchmark curve

Table 2.3 shows the statistical results for the RMSE and the performance metrics mentioned in the previous section for each algorithm considering various population sizes. The Self-Adaptive DE, PGJAYA, and SATLBO converged to the minimum RMSE value of 9.86022E-04 for all 40 independent runs considering NP = 20, 50 and 100 individuals. This RMSE value is in accordance with the minimum RMSE value obtained by many of metaheuristic algorithms applied to the same benchmark curve [34, 36, 59, 60].

Table 2.3 – RMSE and performance metrics obtained for the Self-Adaptive DE, PGJAYA, SATLBO and BHCS algorithms considering different population sizes NP.

	RMSE					Performance metrics			
	NP = 20								
Algorithm	Min	Max	Mean	Median	Std	Best	Worst	SR (%)	Time (min)
DE	9.86022E-04	9.86022E-04	9.86022E-04	9.86022E-04	0	474	1570	100	4.9
PGJAYA	9.86022E-04	9.86022E-04	9.86022E-04	9.86022E-04	2.20737E-16	230	5120	100	4.8
SATLBO	9.86022E-04	9.86022E-04	9.86022E-04	9.86022E-04	3.03843E-16	1651	3670	100	6.8
BHCS	9.86022E-04	3.11849E-03	1.13131E-03	9.96598E-04	3.69053E-04	9304	33903	30	4.4
	NP = 50								
DE	9.86022E-04	9.86022E-04	9.86022E-04	9.86022E-04	0	501	939	100	12.4
PGJAYA	9.86022E-04	9.86022E-04	9.86022E-04	9.86022E-04	0	129	450	100	11.7
SATLBO	9.86022E-04	9.86022E-04	9.86022E-04	9.86022E-04	0	703	1637	100	17.2
BHCS	9.86022E-04	1.34242E-03	1.0609E-03	9.92781E-04	1.09381E-04	28764	44003	10	10.7
	NP = 100								
DE	9.86022E-04	9.86022E-04	9.86022E-04	9.86022E-04	0	100	814	100	24.9
PGJAYA	9.86022E-04	9.86022E-04	9.86022E-04	9.86022E-04	0	73	274	100	23.3
SATLBO	9.86022E-04	9.86022E-04	9.86022E-04	9.86022E-04	0	694	1406	100	33.6
BHCS	9.86022E-04	1.21413E-03	1.01699E-03	9.89621E-04	5.35874E-05	9823	49971	15	47.2

On the other hand, the BHCS algorithm exhibited poor performance regardless of the population size, always failing to converge for most of the 40 runs, showing a much

higher instability than the other algorithms, as can be seen by the obtained standard deviation, which differs from the results published by [36].

The BHCS algorithm showed its best performance for NP = 20 since its success rate was higher. For all population sizes, this algorithm was seen to get trapped at many different local optima, which leads to the conclusion that the search procedure was not efficient compared to the other algorithms.

Moreover, the BHCS algorithm has many control parameters which, if not properly set, may result in poor performance. In this manuscript, the parameters were taken from the original manuscript that proposed this method. The Self-Adaptive DE outperformed all algorithms for NP = 20 in terms of lower standard deviations and convergence speed. For NP = 50 and 100, the standard deviations for the Self-Adaptive DE, PGJAYA, and SATLBO were similar and it is useful to look at Fig. 2.1, which shows notched boxplots for the iterations until convergence for these three algorithms as a function of the population size NP.

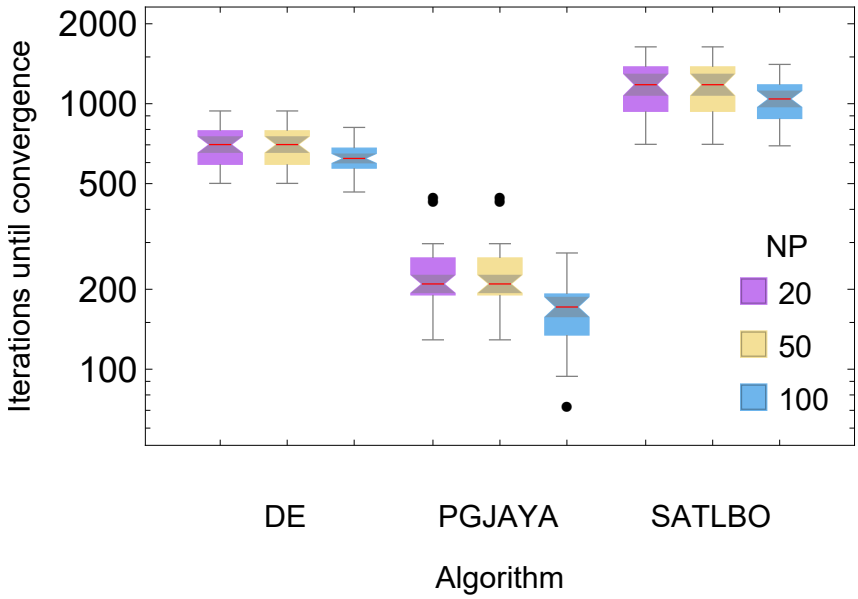

Figure 2.1 – Notched boxplots for the iterations until convergence (convergence speed) as a function of the population size NP for the Self-Adaptive DE, PGJAYA and SATLBO algorithms. The black dots denote outliers. The red line denotes the median and each note denotes a 95 % confidence interval for the median. Increasing NP results in fewer iterations for achieving convergence (higher convergence speed).

It is clear from Fig. 2.1 that increasing NP results in fewer iterations until convergence. However, this increases the execution time, as expected and confirmed by Table 2.3. For NP = 50 and 100, the PGJAYA outperformed all other algorithms in terms of convergence speed and execution time. Therefore, considering the results from this analysis, NP = 50 resulted in a good trade-off between execution time and quality of the results and was selected as the population size for simulations with noisy I-V curves. The results

obtained for the PGJAYA and SATLBO algorithms were even better than the ones obtained in their original manuscripts considering the lower standard deviations obtained, for all population sizes considered in this work.

Table 2.4 shows the minimum, maximum, mean and standard deviation for the photocurrent, dark saturation current, ideality factor, series and shunt resistance obtained from the benchmark curve at the last iteration (best individual) by all algorithms considering 40 runs for each algorithm and NP = 50. Even though the single-diode parameters extracted by the BHCS algorithm had higher variation, their medians were similar to the ones obtained by the Self-Adaptive DE, PGJAYA and SATLBO algorithm.

Table 2.4 – Minimum, maximum, mean, median and standard deviation (STD) of each single diode parameter obtained for the best solution (best individual at last iteration) considering 40 runs for each algorithm and NP = 50 individuals.

	I_{ph}(A)				
Algorithm	Min	Max	Mean	Median	STD
DE	7.60776E-1	7.60776E-1	7.60776E-1	7.60776E-1	8.15238E-11
PGJAYA	7.60776E-1	7.60776E-1	7.60776E-1	7.60776E-1	1.63155E-10
SATLBO	7.60776E-1	7.60776E-1	7.60776E-1	7.60776E-1	6.73208E-11
BHCS	7.60776E-1	7.62195E-1	7.60669E-1	7.60633E-1	3.63901E-4
	I_0(A)				
DE	3.230208E-7	3.230208E-7	3.230208E-7	3.230208E-7	1.585105E-14
PGJAYA	3.230208E-7	3.230208E-7	3.230208E-7	3.230208E-7	1.326495E-14
SATLBO	3.230207E-7	3.230209E-7	3.230208E-7	3.230208E-7	3.446202E-14
BHCS	3.119682E-7	4.525398E-7	3.526014E-7	3.267161E-7	4.012027E-8
	n				
DE	1.481184	1.481184	1.481184	1.481184	4.94543E-9
PGJAYA	1.481184	1.481184	1.481184	1.481184	4.126887E-9
SATLBO	1.481184	1.481184	1.481184	1.481184	1.074212E-8
BHCS	1.477763	1.515646	1.489472	1.482318	1.097064E-2
	$R_s(\Omega)$				
DE	3.637709E-2	3.637709E-2	3.637709E-2	3.637709E-2	1.975463E-10
PGJAYA	3.637709E-2	3.637709E-2	3.637709E-2	3.637709E-2	1.557372E-10
SATLBO	3.637709E-2	3.637709E-2	3.637709E-2	3.637709E-2	4.56818E-10
BHCS	3.526006E-2	3.646851E-2	3.610945E-2	3.634121E-2	3.542171E-4
	$R_{sh}(\Omega)$				
DE	5.371852E1	5.371853E1	5.371852E1	5.371852E1	1.728338E-6
PGJAYA	5.371852E1	5.371853E1	5.371852E1	5.371852E1	2.253902E-6
SATLBO	5.371852E1	5.371853E1	5.371852E1	5.371852E1	2.601979E-6
BHCS	4.483672E1	8.123459E1	6.003299E1	5.505347E1	8.872389

Figs. 2.2 shows the evolution of the best RMSE as a function of the number of iterations, from 1 to 50,000, for the four algorithms applied to the benchmark curve.

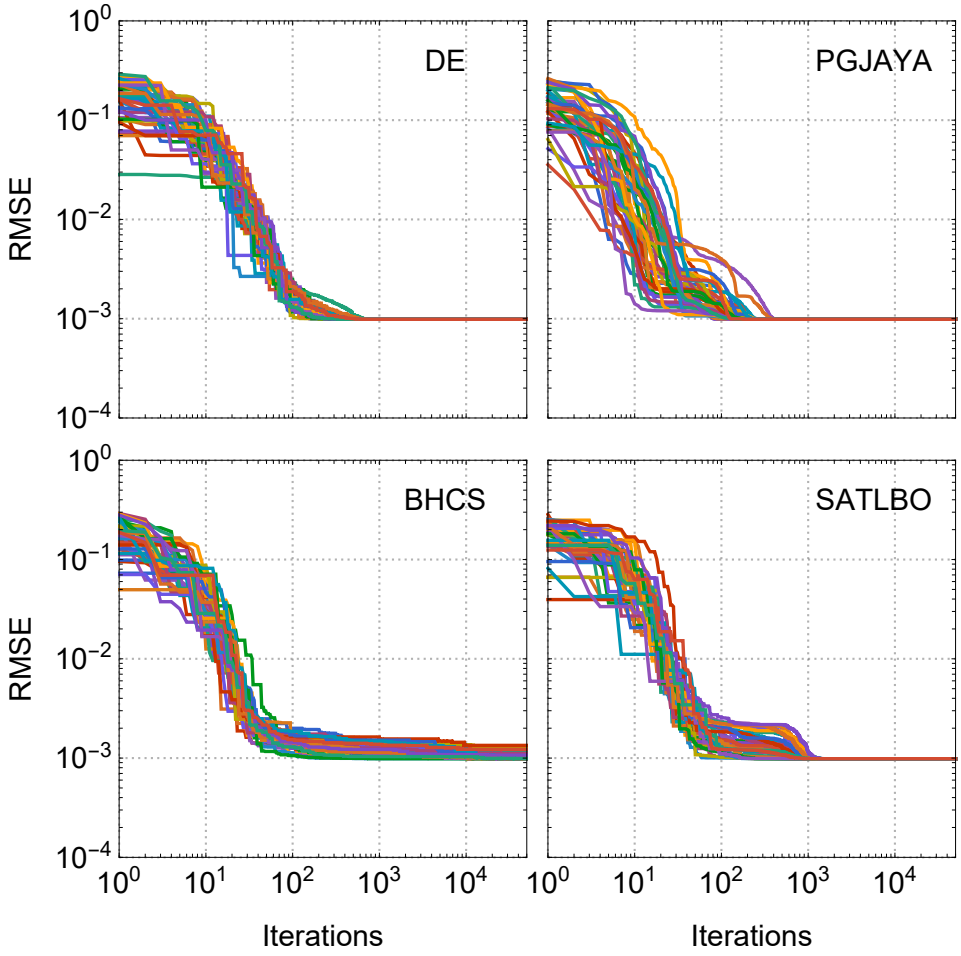

Figure 2.2 – Evolution of the best RMSE achieved by the Self-Adaptive DE, PGJAYA, BHCS and SATLBO algorithms applied to the benchmark IV curve, for all the 40 runs with NP = 50 individuals. Each color represents a different run.

2.5.2 Noise-free I-V curve

To evaluate the performance of the studied algorithms in the most favorable scenario, i.e., in the absence of noise, a noise-free I-V curve was considered. This curve was generated as described in section 3.4, considering $NL = 0$. Fig. 2.3 shows the absolute relative errors obtained for all the single-diode parameters as a function of the objective function, for each algorithm considering 40 runs.

The Self-Adaptive DE algorithm showed the best performance on the noise-free I-V curve since it achieved the lowest absolute relative errors for all parameters, with the smallest variability in the results. The photocurrent was the parameter extracted with the greatest accuracy by this algorithm, for all objective functions. For all 40 runs the extracted I_{ph} values were equal to the theoretical ones up to the 15th significant figure, reason by which there is no notched boxplot for this parameter.

Considering the diode reverse saturation current, all objective functions provided the same results for the Self-Adaptive DE algorithm, achieving an absolute relative error

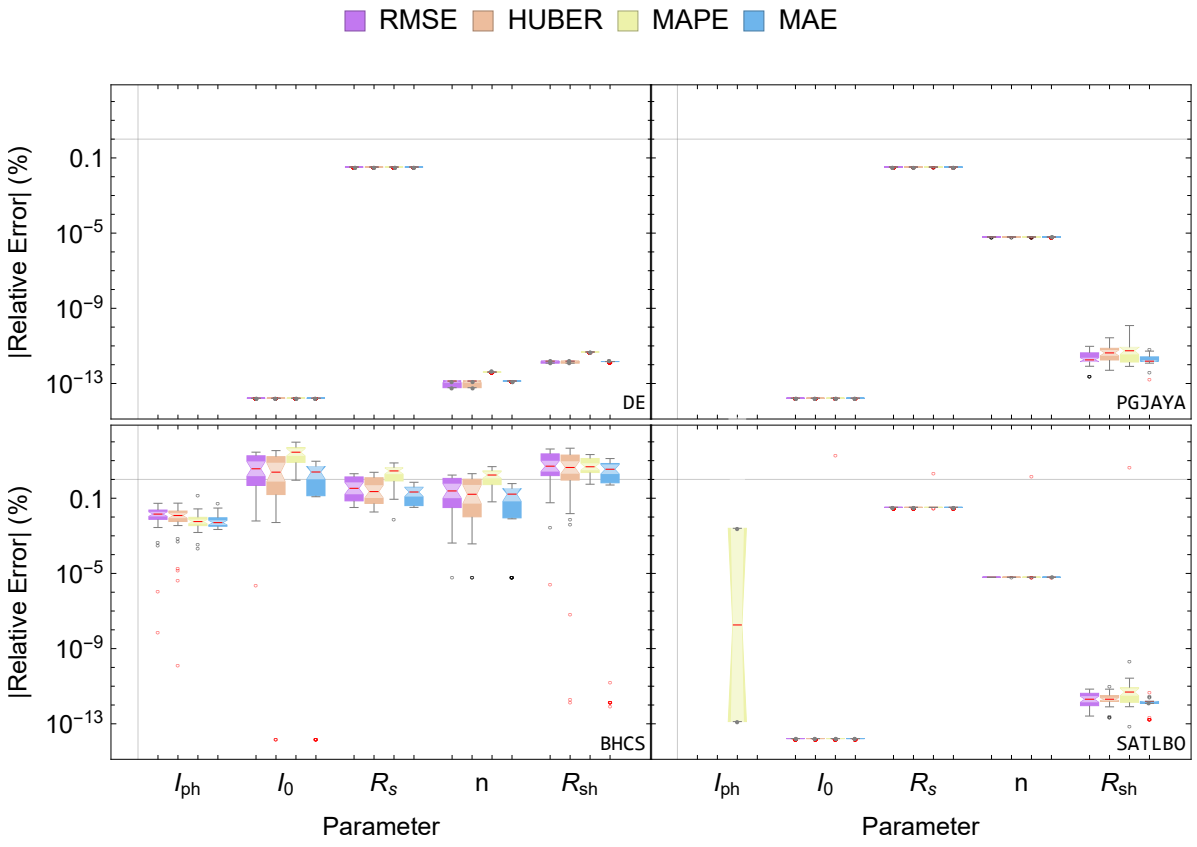

Figure 2.3 – Notched boxplots for the absolute relative errors obtained from the noise-free I-V curve for the single-diode parameters as a function of the objective function, for each algorithm, considering the best individual found at the end of 20,000 iterations. The notches denote the 95 % confidence interval for the medians. The black points denote outliers, while the red ones denote far outliers. Where there are no boxplots, the extracted parameters were equal to the theoretical ones up to the 15th significant figure, so the relative error was null.

of 1.64E-14 % for all 40 runs. The less accurate parameter extracted by this algorithm was the series resistance. The absolute relative errors achieved for this parameter were all equal to 0.032 % for all objective functions, being followed by the shunt resistance, diode ideality factor, and diode reverse saturation current in decreasing order of inaccuracy.

The MAPE provided slight higher absolute relative errors for the diode ideality factor and shunt resistance, with all runs achieving a relative error of 4.73E-12 and 4.05E-13 % for the shunt resistance and diode ideality factor, respectively. When the MAE was the objective function, the relative errors were all equal to 1.48E-12 and 1.35E-13 % for R_{sh} and n, respectively.

The RMSE and Huber loss function achieved the same results for the diode ideality factor and shunt resistance when used as objective functions, with the first quartile of the data being 6.0E-14 % for the diode ideality factor, which was equal to the minimum

relative error. Furthermore, for this parameter, the median was 1.35E-13 %, which was equal to the third quartile and maximum relative error. For the shunt resistance, the minimum relative error obtained by the Self-Adaptive DE algorithm was 1.20E-12 %, which was equal to the first quartile. The median, third quartile and maximum of the absolute relative errors obtained for the shunt resistance were equal to 1.53E-12 %.

The MAPE showed a tendency to result in higher relative errors for n and R_{sh}. For the first, all 40 runs resulted in an absolute error equal to 4.05E-13 %, while for the shunt resistance the MAPE this number increased to 4.73E-12 %. Finally, considering that for n and R_{sh} the notches overlap for the RMSE, Huber function and MAE, differing only when the MAPE was considered, it can be concluded that on the noise-free I-V curve the Self-Adaptive DE algorithm provided accurate results and that the MAPE should be avoided for achieving the lowest possible absolute relative errors between the expected and estimated parameters.

The PGJAYA showed a similar performance to the Self-Adaptive DE algorithm. The only differences were found for the diode ideality factor and shunt resistance. For n, the results for all four objective functions on the 40 runs were all equal to 6.24E-06 %, much higher than the worst-case obtained by the DE algorithm, which was of 4.05E-13 % when the MAPE was applied as the objective function.

Considering the shunt resistance, higher variance in the data according to the objective function was observed. In this case, the MAE provided the lowest absolute relative errors, with 75 % of the errors lower than 2.60E-12 % and achieving a maximum of 7.14E-12 %. For the RMSE, these values increased to 4.29E-12 % and 9.49E-12 %, respectively Also, considering the Huber loss function, these numbers increased to 7.47E-12 and 2.70E-11 %. For the MAPE, 8.33021E-12 % and 1.21E-10 %, respectively.

Also, the presence of outliers below the lower fence was observed when the RMSE and MAE were the objective functions. This means that for a few runs the PGJAYA algorithm was capable of achieving an even lower minimum, escaping the local minima at which it was trapped for most of the runs. For the shunt resistance, the lowest outlier achieved by this algorithm was 1.84569E-13 % when the MAE was considered the objective function. Besides, no significant differences were observed regarding the objective functions for all single-diode parameters except R_{sh}, for which the MAPE showed a tendency to produce higher errors.

The SATLBO achieved higher variances than the PGJAYA algorithm for all parameters except for I_0, for which the absolute relative errors were the same as the ones obtained by the Self-Adaptive DE and PGJAYA algorithms. The MAPE as objective function consistently generated far outliers for all extracted parameters except for I_{ph}, with absolute relative errors as high 21.1, 2.1, 1.6 and 4.7 % for I_0, R_s, n and R_{sh}, respectively, which occurred for the same run and means that this algorithm was trapped at a local

minimum. For I_{ph}, the MAPE as objective function was responsible for a maximum error of 2.0E-3 %. Excluding the outliers, the results obtained by the SATLBO algorithm for the diode reverse saturation current, series resistance and diode ideality factor were the same as the ones obtained by the PGJAYA algorithm. Following the same trend of the PGJAYA algorithm, a higher variance was seen for the shunt resistance, for all objective functions.

For R_{sh}, the MAE provided the lowest absolute relative errors, with 75 % of the data being lower than 1.54E-12 %. Also, outliers were seen for this parameter for all objective functions except for the RMSE, and no significant differences were observed between the RMSE and Huber loss function.

The BHCS algorithm exhibited the worst performance among all compared algorithms on the noise-free I-V curve since the absolute relative errors obtained for all single-diode parameters were significantly higher than those obtained by the other tested algorithms. For the photocurrent, the MAE provided lower errors with lower variance, with 75 % of the resulting errors being lower than 7.30E-3 %, and no significant differences were observed between the MAE and MAPE in terms of the obtained medians. Furthermore, outliers and far outliers were observed.

The lowest absolute relative error achieved by this algorithm for I_{ph} with the RMSE as objective function was of 7.56E-09 %; with the Huber loss function, 0; with the MAPE, 2.25E-04 %, and 0 with the MAE. This means that for some runs the algorithm was able to extract more accurate parameters by escaping points of a local minimum. However, even with higher relative errors, the photocurrent was considered accurate since the highest absolute relative error was of 1.44E-01 % when the MAPE was employed.

For I_0, high relative errors were obtained for all objective functions, reaching errors as high as 9.29, 28.21, 34.2 and 96.06 % when the MAE, RMSE, Huber function and MAPE were employed, respectively. Also, while the MAPE provided higher relative errors than the other objective functions, no significant differences were observed in terms of the medians considering the RMSE, Huber function and MAE. Also, the presence of outliers was seen, meaning that for a few runs the algorithm extracted accurate I_0 values by escaping points of a local minimum. The most accurate values for this parameter were provided by the MAE, with a maximum absolute relative error of 9.29 %.

The same trend was observed for R_s and n, for which the BHCS algorithm with the MAE as objective function extracted more accurate parameters, with maximum absolute relative error of 0.7 % for R_s and 0.6 % for n. The shunt resistance was, after I_0, the less accurate parameter extracted by this algorithm. The MAE provided lower relative errors, with a maximum of 12.9 % and 75 % of the errors being lower than 7 %. When the MAPE was employed, these numbers increased to 21 and 13 %; for the Huber loss function, 45.7 and 19.8 %; for the RMSE, 41.6 and 22.9 %. However, considering the

medians, no significant differences were observed.

Therefore, on the noise-free I-V curve, the Self-Adaptive DE algorithm had the best performance, with lower relative errors and higher stability, being followed by the PGJAYA, SATLBO and BHCS algorithms. Regarding the objective function, it was seen that depending on the parameter, some functions provided lower errors than others. In general, it can be stated that the RMSE, Huber loss function and MAE provided low relative errors without significant differences for the Self-Adaptive DE, PGJAYA and SATLBO algorithms considering all single-diode parameters. For the BHCS algorithm, the MAE was seen to provide the best results for all parameters, but since this algorithm showed higher relative errors and instability even for the noise-free I-V curve, its performance was considered unsatisfactory.

2.5.3 Noisy I-V curves

Figures 2.4 to 2.6 show the noisy I-V curves for the different noise levels considered in this work, with different zoom levels to provide a better distinction among the I-V curves. As can be seen from these figures, noise levels above 1 % are quite unrealistic. Yet, this analysis employed high noise levels to observe the highest noise levels for which the extracted parameters would still be reliable.

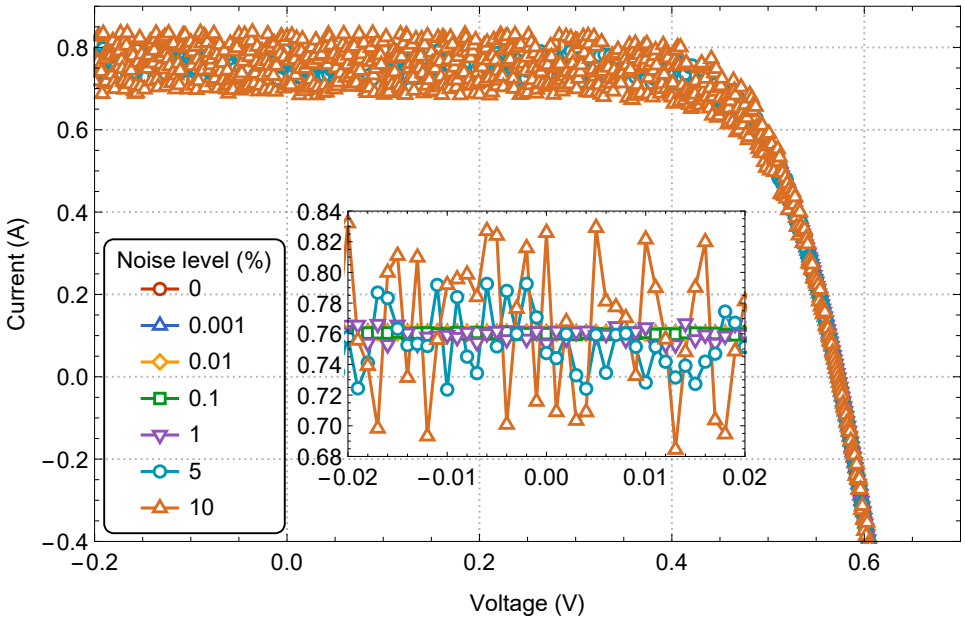

Figure 2.4 – Noise I-V curves for all noise levels (% of the current values) considered in this work. As can be seen, the noise levels of 5 % and 10 % are quite unrealistic for a proper I-V characterization.

Each algorithm was tested on each of the 10 noisy I-V curves for each noise level, considering 40 runs for each curve and the objective functions discussed in section 2. Given the volume of information, each single-diode parameter will have a dedicated discussion.

Fig. 2.7 shows the notched boxplot for the absolute relative errors obtained for I_{ph} as a function of the noise levels and objective function, for each algorithm.

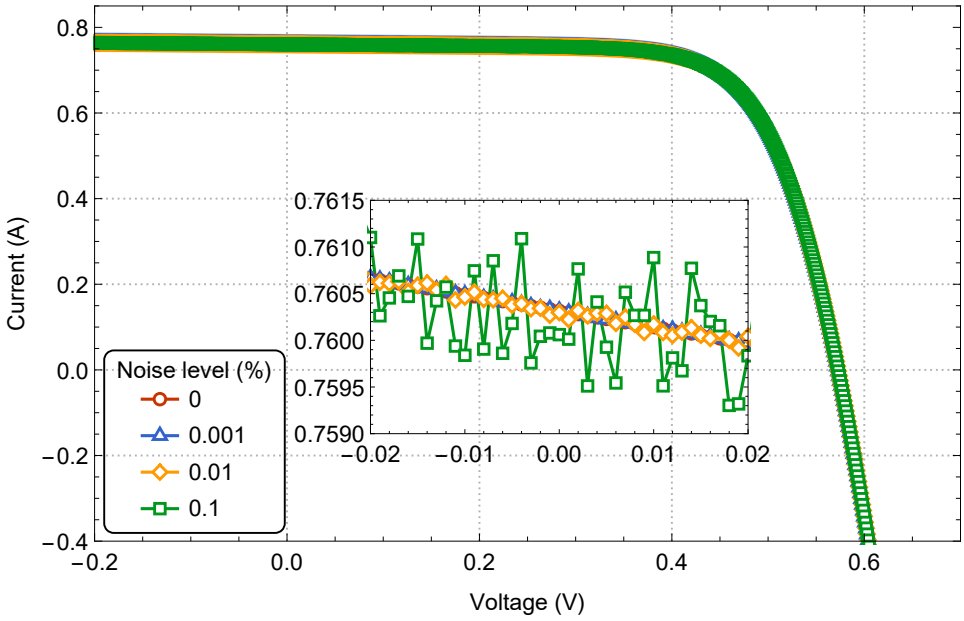

Figure 2.5 – Zoomed noisy I-V curves for noise levels (% of the current values) between 0 and 0.1 %. In this way, it is possible to observe how smaller noise levels affect the current points.

The Self-Adaptive DE and PGJAYA algorithms resulted in a similar performance for all noise levels and objective functions. The highest absolute relative errors obtained by these algorithms were 0.83 % when the MAE was employed as the objective function for the 10 % noise level. Also, for noise levels above 0.1 %, the RMSE and Huber loss function showed a tendency to provide lower absolute relative errors than the MAPE and MAE.

The SATLBO algorithm showed higher variances than the PGJAYA and Self-Adaptive DE when the MAPE and MAE were employed as objective functions, with the occurrence of many outliers and far outliers. Regarding the RMSE and Huber loss function, the performance was equal to that obtained by the previous algorithms. For all noise levels, some outliers above the upper fence were observed, indicating that this algorithm was trapped at points of a higher local minimum.

Also, outliers below the lower fence were observed, meaning that the algorithm was able to avoid being trapped at points with higher values of the objective function. This was common when the MAPE and MAE were employed. For the 10 % noise level the MAPE exhibited a maximum error of 1.05 %, exceeding the limit of 1 %. Therefore, for I-V curves with high noise levels, the RMSE, Huber loss function or MAE should be preferred over the MAPE for the SATLBO algorithm.

The BHCS algorithm showed the worst performance for extracting the photocur-

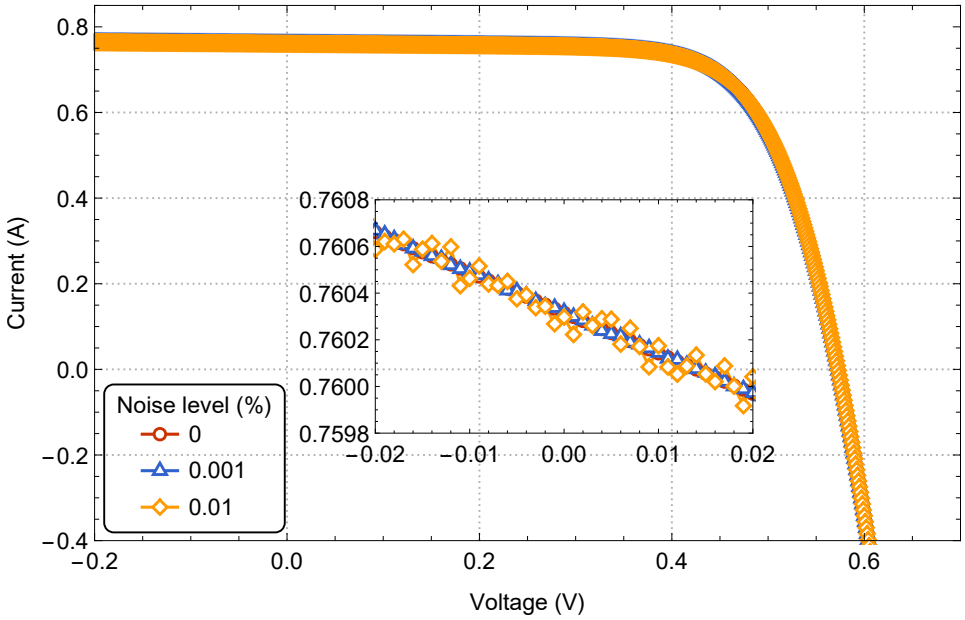

Figure 2.6 – Zoomed noisy I-V curves for noise levels (% of the current values) between 0 and 0.01 %. In this way, it is possible to observe how the smallest considered noise levels affect the current points.

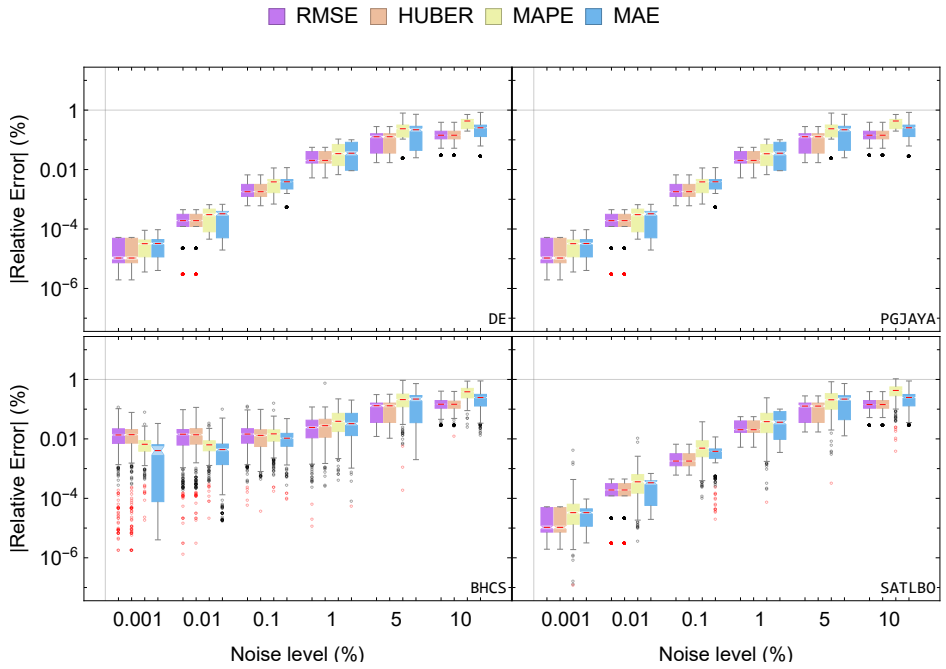

Figure 2.7 – Notched boxplots of the absolute relative errors obtained for the photocurrent as a function of the noise levels and objective function, for each algorithm, considering 10 I-V curves and 40 runs for each curve, amounting to a total of 400 samples. The notches denote the 95 % confidence interval for the medians. The black points denote outliers, while the red ones denote far outliers.

rent since it obtained higher relative errors than the previous algorithms even for low noise levels, with higher instabilities. The presence of outliers was more pronounced, which indicated the instability of the search procedure.

Although showing higher errors for low noise levels, the performance of the BHCS algorithm for the 5 and 10 % noise levels was similar to the previous algorithms. Interestingly, for some runs, it achieved lower relative errors than the PGJAYA and Self-Adaptive DE algorithms, as can be seen from the outliers in Fig. 2.7. Therefore, for practical purposes, if one is interested in extracting I_{ph}, all four algorithms can extract highly accurate values for it even for high noise levels regardless of the objective function.

Fig. 2.8 shows the absolute relative errors obtained for the diode reverse saturation current as a function of the objective function and noise level for each algorithm.

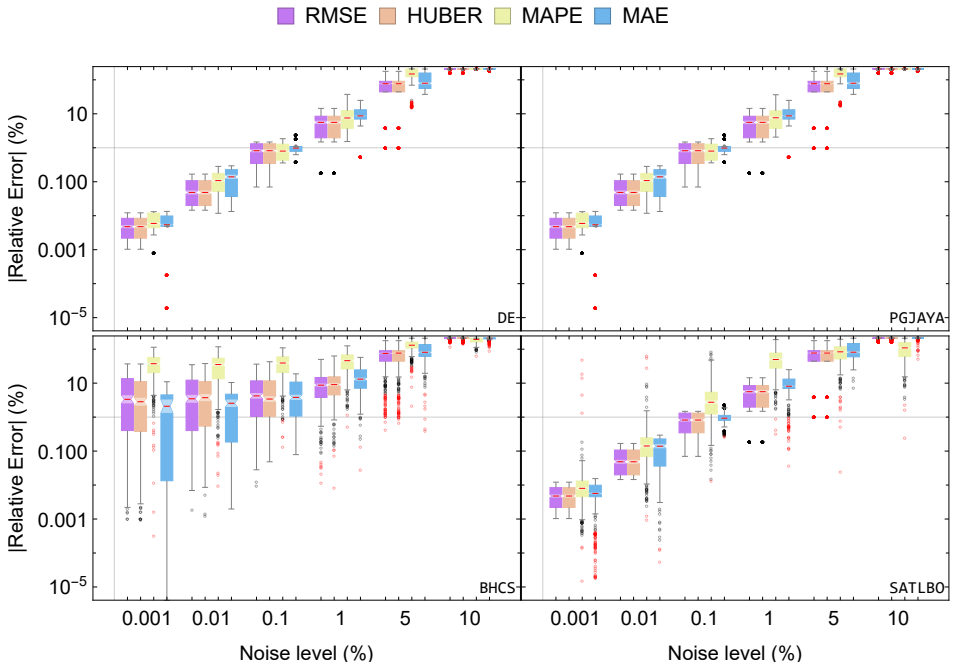

Figure 2.8 – Notched boxplots of the absolute relative errors obtained for the diode reverse saturation current as a function of the noise levels and objective function, for each algorithm, considering 10 I-V curves and 40 runs for each curve, amounting to a total of 400 samples. The notches denote the 95 % confidence interval for the medians. The black points denote outliers, while the red ones denote far outliers.

As for the photocurrent, the Self-Adaptive DE and PGJAYA algorithms showed similar performances. However, in this case, the absolute relative errors were much higher than the ones obtained for I_{ph} even for small noise levels. For the 0.001 % noise level, the absolute relative errors in I_0 are in the order of 1E-03 %, while this value was of 1E-05 % for I_{ph}. Also, these two algorithms were able to extract I_0 values with errors lower than 1 % for noise levels up to 0.1 %.

The RMSE and Huber loss functions were seen to provide more stability to these algorithms and lower absolute relative errors than the other two objective functions, with no significant differences. For the 0.1 % noise level, no significant differences were observed in the medians considering the four objective functions, with the medians equal to 0.82 % for the RMSE and Huber loss function, 0.8 % for the MAPE and 0.98 % for the MAE.

For this same noise level, the maximum relative error achieved by the RMSE and Huber function was 1.46 %, increasing to 1.85 % considering the MAPE and 2.39 % considering the MAE. Also, the third quartiles were 1.31 % for the RMSE and Huber function, 1.28 % for the MAPE and 1.1 % for the MAE. Therefore, for the 0.1 % noise level, the threshold of 1 % was exceeded, but since the highest absolute relative error was equal to 2.39 %, the I_0 values extracted by the Self-Adaptive DE and PGJAYA algorithms are still accurate. For the 1 % noise level, the medians obtained with the RMSE and Huber loss function were equal to 5.6 %, increasing to 76.8 and 210 % for the 5 and 10 % noise levels.

The SATLBO algorithm had similar performance to the Self-Adaptive DE and PGJAYA algorithms when the RMSE and Huber loss function were employed, for all noise levels. However, when the MAPE was used as the objective function, many outliers above the upper fence were observed for noise levels between 0.001 and 0.1 %, which means that this algorithm was trapped at many different points of a local minimum. Due to this fact, errors as high as 48.87 % for the 0.001 % noise level; 63.8 % for the 0.01 % noise level and 85 % for the 0.1 % noise level. Therefore, considering that the MAPE consistently provided higher errors, it should be avoided as the objective function for the SATLBO algorithm.

In addition, for the 0.1 % noise level, the SATLBO performance was similar to the two previous algorithms, except for the MAPE which, again, provided higher errors, with a median equal to 2.73 %. Considering the stability and quality of results, the RMSE and Huber loss function should be preferred as objective functions also for the SATLBO algorithm, providing accurate results for noise levels up to 0.1 %.

The BHCS showed much higher instabilities for all noise levels and objective functions, and even for a small noise level of 0.001 % relative errors as high as 36.8, 36.6, 113 and 11 % were observed when the RMSE, Huber loss function, MAPE, and MAE were considered, respectively. Interestingly, for the 0.001 and 0.01 % noise levels, the MAE provided better results as the objective function for the BHCS algorithm. Above that, the RMSE and Huber function provided better results. However, due to the high relative errors even for small noise levels, this algorithm cannot be recommended for extracting the diode reverse saturation current.

Fig. 2.9 shows the absolute relative errors obtained for the diode ideality factor as a function of the objective function and noise level for each algorithm. Even for high

noise levels, such as 5 and 10 % of the current values, this parameter was not significantly affected, with the highest errors in the order of 10 %. For noise levels below 1 %, these two algorithms were able to extract the diode ideality factor with relative errors smaller than 1 % when the RMSE and Huber loss functions were employed. Furthermore, the Self-Adaptive DE and PGJAYA algorithms showed stable and similar performances, with no significant differences observed when the RMSE and Huber function were considered as objective functions.

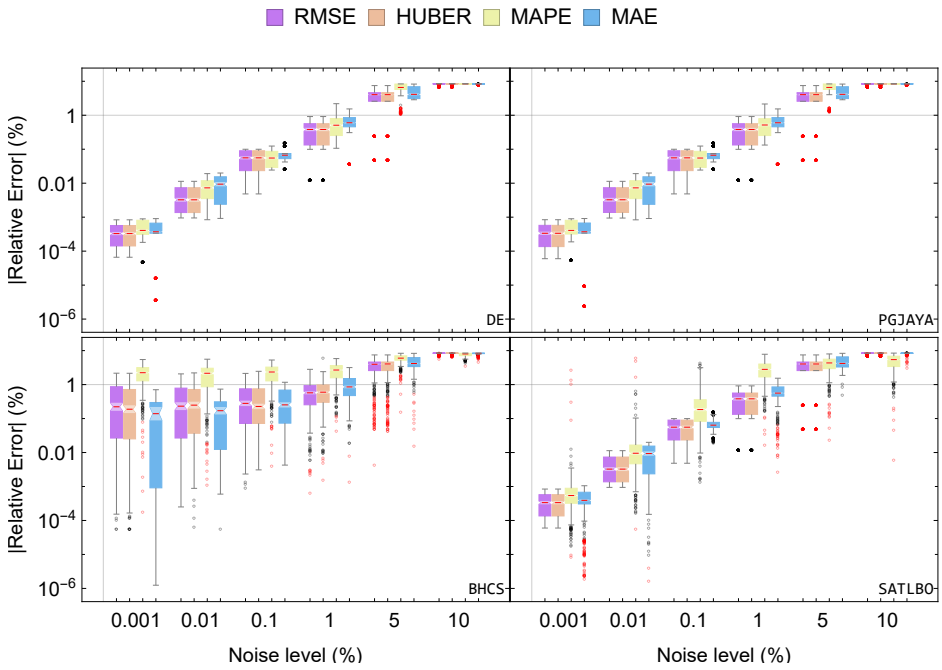

Figure 2.9 – Notched boxplots of the diode ideality factor obtained for the diode ideality factor as a function of the noise levels and objective function, for each algorithm, considering 10 I-V curves and 40 runs for each curve, amounting to a total of 400 samples. The notches denote the 95 % confidence interval for the medians. The black points denote outliers, while the red ones denote far outliers.

The SATLBO showed higher instabilities than the Self-Adaptive DE and PGJAYA algorithms, with the best results given when the RMSE or Huber function were considered as objective functions. Also, the MAPE as objective function resulted in a much higher instability, with many outliers and far outliers above the upper fences. With the RMSE and Huber loss function, the performance of the SATLBO algorithm was similar to the PGJAYA and Self-Adaptive DE with the same objective functions. The BHCS algorithm again showed much higher instabilities than the other three, even for small noise levels. For noise levels equal to 0.001 and 0.01 %, the MAE as the objective function provided better results than the ones obtained for the other functions. For noise levels equal and higher than 1 %, the RMSE and Huber function provided better results, while the MAPE showed the worst results for all noise levels.

From this analysis, it can be concluded that the diode ideality factor can be accurately extracted by the Self-Adaptive DE, PGJAYA, and SATLBO algorithms if the RMSE, Huber loss function or MAE are employed as the objective function, providing errors lower than 1 % for noise levels up to 1 %.

Fig. 2.10 shows the absolute relative errors obtained for the series resistance. For the noise level of 0.001 % of the current values, no significant differences were observed for the PGJAYA and the Self-Adaptive DE considering the four objective functions. For noise levels between 0.001 and 1 %, both algorithms extracted the series resistance with relative errors smaller than 1 % for most cases, considering the four objective functions.

For this noise range, the MAPE resulted in a higher instability, with the presence of more outliers and far outliers. For the 5 % noise level, the RMSE and Huber loss function provided lower errors, with 75 % of the data being lower than 7.1 % for both functions. Considering the same noise level, this number increased to 9.5 % when the MAE was employed, and 9.44 % when the MAPE was considered as objective function. For the 10 % noise level, all objective functions provided similar results, with relative errors in the order of 16 %.

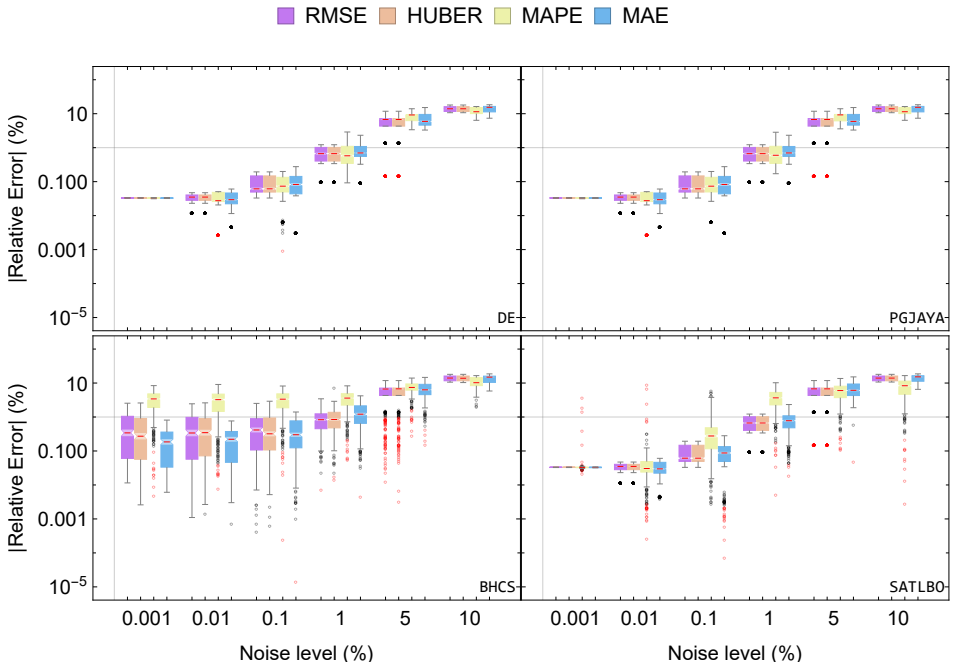

Figure 2.10 – Notched boxplots of the absolute relative errors obtained for the series resistance as a function of the noise levels and objective function, for each algorithm, considering 10 I-V curves and 40 runs for each curve, amounting to a total of 400 samples. The notches denote the 95 % confidence interval for the medians. The black points denote outliers, while the red ones denote far outliers.

The SATLBO algorithm showed a higher instability than the Self-Adaptive DE and PGJAYA algorithms when the MAPE and MAE were employed as objective functions.

Even for a 0.001 % noise level, the MAPE resulted in the occurrence of many far outliers, with errors reaching 3.9 %. The results considering the RMSE and Huber function were similar, with low relative errors and higher stability. For the 10 % noise level, the MAPE resulted in lower errors, with 75 % of the errors being lower than 11.4 %, but many outliers and far outliers were observed. For the other three objective functions, this number was in the order of 16 %, the same as for the Self-Adaptive DE and PGJAYA algorithms.

The BHCS algorithm showed the worst performance, with higher relative errors for small noise levels such as 0.001 and 0.01 %, considering the four objective functions. The MAPE was seen to provide the worst results, with relative errors reaching 8 and 9 % for the 0.001 and 0.01 % noise levels. For this algorithm, the MAE provided lower errors for noise levels between 0.001 and 0.1 %, while for the 1 and 5 % noise levels the RMSE and Huber loss function provided lower errors. For the noise levels of 1, 5 and 10 %, the performance achieved by the BHCS algorithm was similar to the other three algorithms, except for a higher occurrence of outliers and far outliers.

In general, for achieving absolute relative errors lower than 1 % for the series resistance, the level of noise on the current values should be lower than 1 %. For higher noise levels, the median of the relative errors was seen to increase to values between 15 and 20 % for all algorithms, considering all objective functions.

Finally, Fig. 2.11 shows the absolute relative errors obtained for the shunt resistance as a function of the noise level and objective function for each algorithm. Again, the Self-Adaptive DE and PGJAYA algorithms showed similar results for all noise levels and objective functions, with the RMSE and Huber function providing lower relative errors. The SATLBO algorithm showed higher instabilities than these previous two algorithms, especially when the MAPE was employed. The RMSE and Huber function achieved lower relative errors, except for the noise level of 10 % for which, again, the MAPE resulted in lower errors but showed a higher instability.

The BHCS algorithm showed higher instabilities, as for the previous parameters, and lower relative errors were found when the MAE function was considered for the noise levels of 0.001 and 0.01 %. For the noise level of 0.1 %, the RMSE and Huber function achieved lower relative errors, and for noise levels higher than that, the RMSE and Huber function achieved results with no significant differences from the ones obtained when the MAE was the objective function.

The errors obtained for the shunt resistance considering the Self-Adaptive DE, PGJAYA and SATLBO algorithms jumped from the order of 0.001 % for a 0.001 % noise level to 73 % for a 10 % noise level. In contrast, for the BHCS algorithm, the lowest relative errors were obtained when the MAE was employed, with 75 % of the results showing relative errors lower than 6.3 %. Considering the MAPE, to 12.7; considering the Huber loss function, to 13.8 %; and considering the RMSE, to 17.1 %.

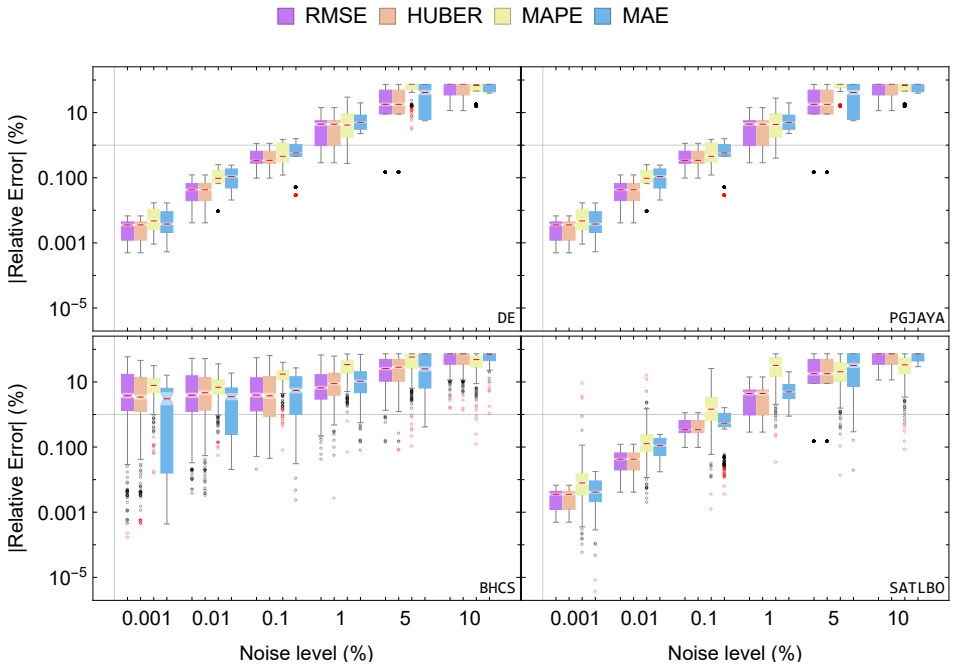

Figure 2.11 – Notched boxplots of the absolute relative errors obtained for the shunt resistance as a function of the noise levels and objective function, for each algorithm, considering 10 I-V curves and 40 runs for each curve, amounting to a total of 400 samples. The notches denote the 95 % confidence interval for the medians. The black points denote outliers, while the red ones denote far outliers.

Thus, for extracting accurate shunt resistance values, the Self-Adaptive DE, PGJAYA, and SATLBO algorithms should be preferred, with the RMSE and Huber loss function as objective functions. For the 0.1 % noise level, these objective functions had similar performance, with maximum errors of 1.14 % and 75 % of the resulting errors being lower than 0.65 %. For noise levels above than 0.1 %, the extracted R_{sh} values were not considered accurate.

Finally, considering that the tolerance error for electronic components is in the order of 0.2 % [61], the Self-Adaptive DE, PGJAYA, and SATLBO algorithms can be considered excellent alternatives for extracting the single-diode parameters from noisy I-V curves if the RMSE or Huber loss functions are employed as the objective function.

2.6 Conclusion

In this work, the metaheuristic optimization algorithms known as Self - Adaptive Differential Evolution, Performance Guided JAYA (PGJAYA), Self - Adaptive Teaching - Learning Based Optimization (SATLBO) and Biogeography - based Heterogeneous Cuckoo Search (BHCS) were employed for extracting the single-diode parameters from a widely used benchmark curve, noise-free and simulated noisy I-V curves, to study how

these methods behave in noisy environments, including simulations considering four different objective functions: the Huber loss function, RMSE, MAPE, and MAE.

The results of this work showed that on the RTC France benchmark curve the PGJAYA algorithm showed better performance considering the convergence speed and execution time for a population size of 50 individuals. For the noise-free I-V curve, it was seen that the Self-Adaptive DE algorithm provided the lowest absolute relative errors, with lower variance, than all other algorithms, being followed by the PGJAYA, SATLBO and BHCS algorithm, which showed severe difficulties for extracting accurate I_0, and R_{sh} values considering all objective functions.

Considering the noisy I-V curves, it was seen that for noise levels smaller than 0.1 % of the current values the Self-Adaptive DE, PGJAYA and SATLBO algorithms were able to extract all single-diode parameters with high accuracy, with absolute relative errors smaller than 1 %. However, for the latter, the MAPE should be avoided as the objective function since even for low noise levels it showed far outliers when employed a the objective function for the SATLBO algorithm.

Regarding the objective functions, it was seen that for the Self-Adaptive DE, PGJAYA and SATLBO algorithms, the RMSE and Huber loss function showed a tendency to provide lower absolute relative errors for all parameters, especially for noise levels up to 1 %. The MAE showed a higher variance for these algorithms, while the MAPE, when applied to the SATLBO algorithm, resulted in far outliers even for small noise levels such as 0.001 and 0.01 %. The BHCS algorithm was considered unsatisfactory for all single-diode parameters except I_{ph}, n and R_s when the MAE was used as the objective function.

Furthermore, it was seen that the single-diode parameters showed different sensitivity to noise levels, regardless of the algorithm and objective function. The photocurrent values had the highest absolute relative errors in the order of 1 % for a 10 % noise level. For this same noise level, the highest errors obtained for the diode ideality factor were in the range 7-10 %. For the series resistance, the highest relative errors increased to values between 15-20 % for a 10 % noise level. Shunt resistance and diode reverse saturation current showed absolute relative errors as high as 73 and 210 % for noise levels above 5 %, being the most affected parameters.

Finally, this work showed that the performance of metaheuristic methods can significantly change depending on the objective function, especially if noise levels are considered. Therefore, it is recommended that future research works proposing new metaheuristics for extracting PV parameters from I-V curves take into account the effects of different objective functions, as well as the robustness against noises.

3 Nitride semiconductors as electron-selective contacts for SHJ solar cells

This chapter is based on the following publications:

 D. Febba, V. Paratte, L. Antognini, J. Dreon, J. Hurni, J. Thomet, R. Rubinger,E. Bortoni, C. Ballif, and M. Boccard, "Effects of Work Function and Electron Affin-ity on the Performance of Carrier-Selective Contacts in Silicon Solar Cells Using $ZnSn_xGe_{1-x}N_2$as a Case Study, IEEE Journal of Photovoltaics, pp. 1–8, 2021 [62].

 D. Febba, V. Paratte, L. Antognini, J. Dreon, J. Hurni, J. Thomet,C. Ballif, and M. Boccard, , $ZnSn_xGe_{1-x}N_2$ as electron-selective contact for silicon heterojunction solar cells",in 2021 IEEE 48th Photovoltaic Specialists Conference (PVSC). IEEE, Jun. 2021, pp. 0854–0857 [63].

This work was developed at the Photovoltaics and Thin Film Electronics Laboratory (PV-LAB), École Polytechnique Fédérale de Lausanne (EPFL), in Neuchâtel, Switzerland.

3.1 Zinc Tin Germanium nitride ($ZnSnGeN_2$) alloys

3.1.1 Motivation

The search for new Earth-abundant and low-cost materials for PV applications has led to a recent interest in II-IV-N_2 semiconductors. Among these, $Zn_xSn_{1-x}N_2$ is an interesting candidate due to a tunable direct bandgap depending on stoichiometry ($0 < x < 1$), with values ranging from 0.7 to 2.8 eV [64], and strong optical absorption in the solar spectrum [65]. Alloying $ZnSnN_2$ with $ZnGeN_2$, another direct bandgap semiconductor but with wider energy gaps in the range 2.7–3.4 eV [66], results in $Zn(Sn_xGe_{1-x})N_2$ (ZTGN) compounds that can extend the bandgap range further up.

Moreover, given the width of its bandgap tunability, ZTGN can be applied either as a PV absorber ($x = 1$, corresponding to ZTN, for example), or as a contacting material for heterojunction solar cells when the Ge concentration increases and ZTGN shows wide bandgaps. In the latter case, it is interesting to note that this material could, at the same time, be used as absorber and contact layer in the same structure, by only changing its stoichiometry.

As a new system of materials, research on ZTGN is still in its early stages. The first work reporting its synthesis and structural characterization dates back to 2012 [67]. This was motivated by the bandgap tunability of $In_xGa_{1-x}N$ alloys, and proposed the

replacement of the group III by group II (Zn) and IV (Sn, Ge) elements to improve raw-material availability for large-scale PV applications.

Bandgap tunability of ZTGN was experimentally demonstrated in [68], which reported an increase in bandgap from 2 eV to 3.1 eV, mostly due to a shift in the conduction band to higher energies as the Ge content increased. Since then, other works reported bandgaps in the range 2.1–3.01 eV [69] and 2.2–2.7 eV [70]. Moreover, ZTGN presents also a wide range of conductivity (n-type) depending on composition, with an exponential increase in conductivity as the Sn content increases, along with a decrease of its dark conductivity activation energy [69, 70].

Yet, the accomplishment of PV devices with this family of semiconductors remains a largely unexplored research topic, with few works reporting PV devices with ZTN as absorber [71–73] and only one studying ZTN as electron-selective contact for silicon solar cells [74]. Nevertheless, the wide ranges of values for bandgap and conductivity of ZTGN alloys makes them interesting materials to study as electron-selective contact.

Historically, SHJ cells have been used as test platform for evaluating novel carrier-selective contacts since it combines a nearly perfect absorber (crystalline silicon), interlayers inherently providing excellent passivation without any selectivity (intrinsic amorphous silicon), and nearly perfect carrier-selective layers (doped silicon layers) [2, 8].

In this context, we fabricated by combinatorial sputtering ZTGN layers of varying Zn, Sn and Ge content to assess their effectiveness as electron-selective contacts in SHJ solar cells. We characterized their optical and electrical properties and analyzed several SHJ solar cells with different architectures featuring these layers as electron-selective contact.

By modelling the current-voltage characteristics of these solar cells, we draw the band alignment of $Zn(Sn_xGe_{1-x})N_2$ with silicon for various x values. Based on these results, we discuss the impact of work function and electron affinity on solar cell performance and evidence two different possible causes for poor device performance.

3.1.2 Layers on glass

3.1.2.1 Fabrication and characterization methods

ZTGN layers were initially deposited on glass for material characterization through a combinatorial co-sputtering approach to assess a wide range of composition in a single deposition run. The chamber was first evacuated to a pressure of 2.6×10^{-7} mbar, and then a constant flow of 17.5 sccm N_2 was introduced in the chamber to reach 1.3×10^{-2} mbar.

The power of RF generators on the Sn (99.995% purity) and Ge (99.999% purity) metallic targets (100-mm diameter) was adjusted at 59 and 100 W, respectively, while the

Zn target (99.98% purity) was kept at a DC power of 45 W, leading to an estimated 50% Zn/25% Sn/25% Ge composition at the central position of the substrate (assessed from deposition rate from each target individually). The substrate was not rotated during deposition, which created a gradient in composition. Deposition lasted 30 minutes, following 8 minutes of pre-sputtering.

The resulting combinatorial library, with 0.49 cm^2 samples, was subjected to ellipsometry measurements over the range 0.6–6 eV at an angle of 70° using a Horiba Jobin Yvon ellipsometer. The experimental data was fitted to the Tauc-Lorentz model through the DeltaPsi2 software to extract thickness and optical bandgap (E_{04}, the energy at which the absorption coefficient falls below 1×10^4 cm^{-1}).

For dark conductivity measurements, 100 nm thick and 8 mm long Al pads, 1 mm spaced, were evaporated on the samples which were then annealed at 210 °C for 30 min. The samples were placed on a temperature-controlled chuck inside a vacuum chamber, with N_2 atmosphere at 1 mbar, for temperature-dependent dark conductivity measurements.

For these measurements, the samples were annealed at 180 °C for 1.5 hours, followed by a slow temperature decrease down to 30 °C (5 hours in total) during which conductivity was monitored. Conductivity at 20 °C and activation energy were both extracted from Arrhenius plots, by fitting conductivity data during the temperature ramp down to $\sigma(T) = \sigma_0 \exp(-E_A/kT)$, where k, E_A and σ_0 are the Boltzmann constant, activation energy and an exponential factor which corresponds to the conductivity as $T \to \infty$, respectively.

3.1.2.2 Opto-electronic properties

Fig. 3.1 shows a picture of the resulting ZTGN combinatorial library, together with the Arrhenius conductivity plots, thickness and E_{04} for positions 1 to 5. Thickness was around 100 nm, with the Sn-rich side appearing slightly thicker. Also, E_{04} shifted to higher energies as the Ge content increased, which confirmed the findings obtained in previous studies [68–70], where an increase in bandgap was seen for samples with higher Ge content.

Conductivity and activation energy were found to strongly change between Sn and Ge-rich samples, going from 7 S cm^{-1} and 17 meV at the Sn-rich position, to 2.5×10^{-10} S cm^{-1} and 610 meV at the Ge-rich position. These findings corroborated previous works [69, 70], where a strong decrease in resistivity was observed when the Ge content increased, along with an increase in activation energy. Moreover, as observed in [69], although the Ge-rich sample showed an exponential increase in conductivity as the temperature increased, the Sn-rich sample showed only a small and linear increase. This corresponds to an intermediate behavior between semiconductor-like and metal-like, suggesting a (close-

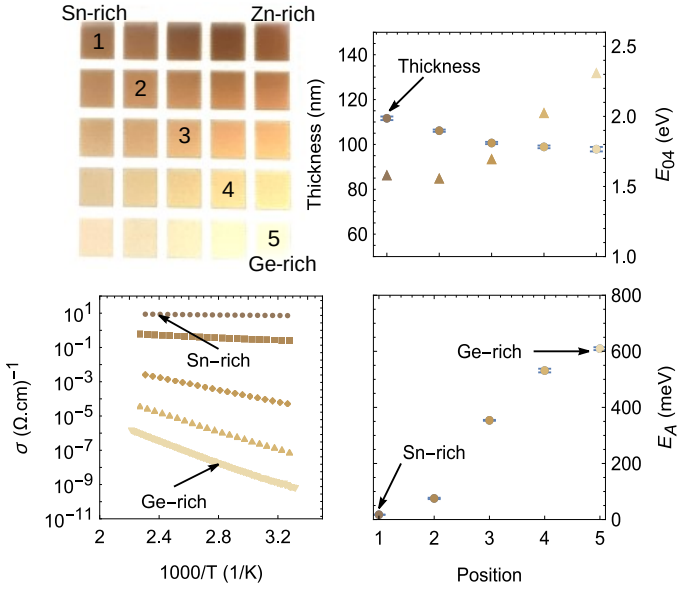

Figure 3.1 – Photograph of the combinatorial ZTGN samples deposited on glass (top left), and material properties against position on the combinatorial library. Position 1 and 5 are Sn and Ge-rich, respectively.

to-)degenerate doping. This explains the slightly higher E_{04} value for position 1 than position 2 in spite of a higher Sn content.

Thus, increasing the Ge content resulted in more insulating samples showing an increased bandgap and activation energy. This trend was attributed in [70] to the higher electronegativity of Ge than of Sn, making it a poorer electron donor, ultimately leading to a reduced density of thermally activated carriers in the conduction band.

3.1.3 Solar cells

3.1.3.1 Fabrication and characterization methods

Front-junction SHJ solar cells were fabricated through standard protocols on chemically etched c-Si wafers. Both n- and p-type float zone (FZ) wafers were used, with thickness and resistivity around 200 µm and 2 Ω cm, respectively. Intrinsic and doped amorphous silicon (a-Si:H) were deposited by PECVD, and ITO was sputtered on top of the Si wafer with a metallic grid, defining 0.49 cm^2 solar cells as sketched in Fig. 3.2. The backside of each wafer was covered with ITO/Ag by magnetron sputtering, and silver paste contacts were then applied on the front of each cell to enable contacting. Also, as reference, SHJ solar cells were fabricated with standard front-junction architecture on n and p-type Si.

Fig. 3.2 also shows the results of Energy Dispersive Spectroscopy (EDS), which was carried out on ZTGN layers grown on a Double Sided Polished (DSP) p-Si wafer to investigate the Zn, Sn and Ge composition at five positions corresponding to the ones

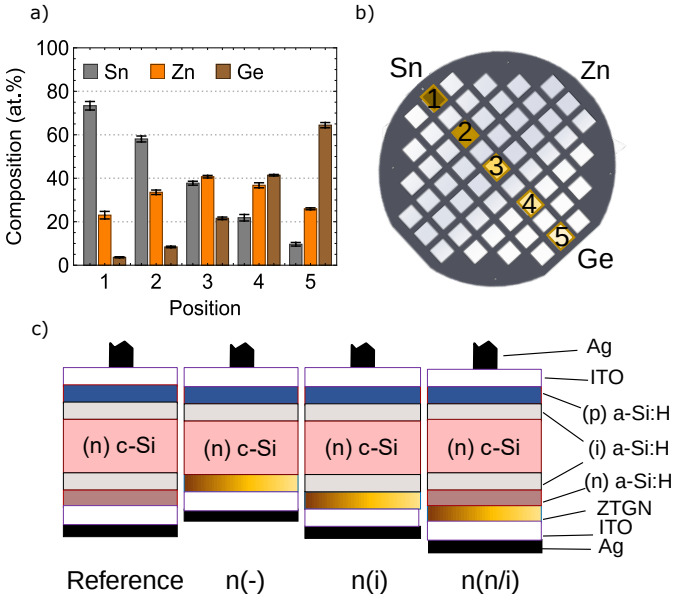

Figure 3.2 – a) Estimated composition (at.%) of each solar cell on 5 positions on the silicon wafer, shown in b), where Zn, Sn and Ge denote the approximate positions of the sputtering guns against the wafer; c) architectures of the investigated SHJ solar cells with ZTGN, and the corresponding reference cell.

of the studied solar cells. The sputtering conditions were the same as for solar cells, but deposition time was increased to 1 hour, targeting 200 nm thick layers at the center of the silicon wafer.

The resulting solar cells had a Sn/(Sn+Ge) ratio ranging from $(90 \pm 1)\%$ (position 1) to $(10 \pm 1)\%$ (position 5), which shows that the combinatorial approach was effective at exploring a wide range of cation composition. The uncertainty of the atomic percentage of each element was evaluated as the 95% confidence interval for the mean, estimated from measurements over several areas on different spots at each position.

Furthermore, as sketched in Fig. 3.2, the ZTGN layer was placed either as passivating electron-selective contact (replacing both the intrinsic and (n) a-Si:H films), or simply as electron-selective contacts on top of an (i) a-Si:H layer, or even as spectator between the (n) a-Si:H layer and ITO, according to the methodology presented in [74]. The sputtering parameters were the same as for samples deposited on glass, except that deposition time was reduced to 8 minutes, after a 2-minute pre-sputtering step, targeting layers 20 nm thick at the central position of the silicon wafer, which was confirmed by ellipsometry.

Five solar cells from each wafer were subjected to IV characterization using a custom-made solar simulator developed at PV-LAB. For that, solar cells were covered with a mask of 0.49 cm^2 and positioned on a temperature-controlled vacuum chuck at 25 °C, kept stable by a PID controller, a PT100 temperature sensor and peltier modules.

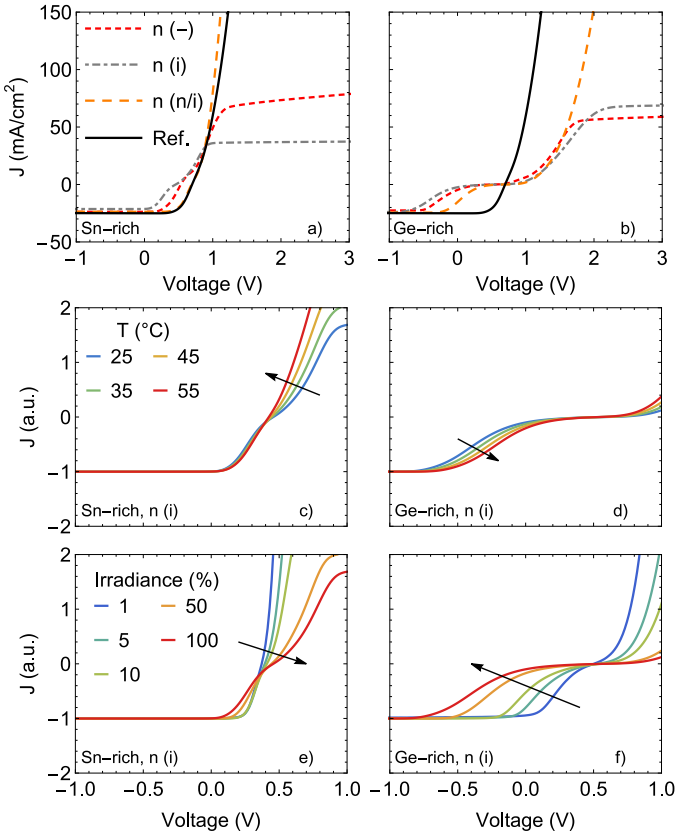

Figure 3.3 – JV curves at STC with a) Sn and b) Ge-rich ZTGN layers at STC (a standard SHJ solar cell JV curve is also shown as reference). c) and d) show the temperature effects on the JV characteristics of the Sn and Ge-rich solar cells, respectively, from architecture "n(i)", while e) and f) show the irradiance effects on the same cells. JV curves were normalized to J_{ph} in c), d), e) and f), and arrows denote increasing temperature and irradiance.

The JV characteristics were then measured with the 4-wires approach by a Keithley 2601 Source Measure Unit (SMU) at five different levels of irradiance: 1, 5, 10, 50 and 100% of 1000 W cm^{-2}, provided by LED and halogen lamps.

3.1.3.2 Device architecture: impacts on JV characteristics

Fig. 3.3 a) and b) show the JV characteristics (STC) of solar cells with Sn and Ge-rich ZTGN composition, after annealing for 30 min at 210 °C, for the three architectures tested on n-Si. The other three solar cells, at positions 2-4, showed a behavior similar to that of the Sn-rich one, and therefore are not shown.

Common features were observed when ZTGN was used as selective contact, *i.e.* structures n(-) and n(i), regardless of composition: two steps in current (one around V_{oc} and another at high bias) and a saturation behavior in forward bias (strict when a-Si:H was present, but with a slight current drift as voltage increases in absence of the intrinsic a-Si:H).

Inserting an (n) a-Si:H before the ZTGN layer, which relaxes the electron-selectivity requirements for the ZTGN layer, brings a clear difference between the two ZTGN compositions: in the Sn-rich case (Fig. 3.3 a)), the s-shape around V_{oc} and the saturation were suppressed, resulting in an IV curve similar to (and even slightly better than) the reference cell. Conversely, for the Ge-rich sample, the rectification was suppressed, but the strong s-shape around V_{oc} was maintained. These results suggest that both layers lack electron selectivity since device performance benefited from the addition of the (n) a-Si:H layer, but the Ge-rich layer imposes an additional barrier to the electron flow compared to the Sn-rich case. These two different sources of barrier to electron extraction are further discussed in the next sections.

Fig. 3.3 c) to f) further show irradiance- and temperature-dependent IV measurements of the devices using an intrinsic passivation layer under the ZTGN film (no (n) a-Si:H layer), to further investigate the S-shape observed at STC. As reported in [75], if transport through a barrier is the limiting factor, decreasing the temperature reduces the amount of charge carriers crossing the barrier, leading to an accumulation of carriers near the interface, reducing the collection efficiency and causing an early onset of the s-shape curve. Accordingly, the s-shapes around V_{oc} were reduced at high temperatures, enhancing the fill factor, as shown in Fig. 3.3 c) and d). For the Ge-rich case, a prominent S-shape remained, suggesting that a barrier is still present. This can be linked to the high activation energy in the ZTGN layer itself ($> 600\,\text{mV}$) for which a measurement temperature of 55 °C is not high enough.

Furthermore, when increasing irradiance, a higher density of photogenerated carriers will be generated, causing also a carrier accumulation at the barrier. This induces a higher band bending and therefore a higher barrier to be overcome, resulting in an earlier onset of the s-shaped curve. Accordingly, Fig. 3.3 e) and f) shows that reducing the light intensity while keeping the temperature at 25 °C reduced the s-shapes and its voltage onsets. Overall, these results suggest that a thermionic emission barrier is limiting electron extraction in both cases, though more severely for the Ge-rich case.

3.1.3.3 Exchange current density modeling

To further investigate the limiting mechanisms behind these JV characteristics, we fitted temperature-dependent JV measurements for solar cells from positions 1 to 5 using the architecture “n (i)”. We used a recent model, presented in [76], that describes the JV characteristics of a contact-limited solar cell based on the equilibrium exchange currents of electrons and holes at each contact, since the observed JV curves clearly violate the superposition principle and thus the single-diode model seen in chapter 2 cannot be applied. According to this model, the JV characteristics of a contact-limited solar cell can be described by

$$J(V) = -\left(J_L + j_{0n}^{\alpha} + j_{0p}^{\beta}\right) + \frac{J_L + j_{0n}^{\alpha} + J_{0n}^{\beta}}{1 + \frac{J_{0n}^{\beta}}{j_{0n}^{\alpha}} e^{-(V - JR_s)/V_T}} + \frac{J_L + j_{0p}^{\beta} + J_{0p}^{\alpha}}{1 + \frac{J_{0p}^{\alpha}}{j_{0p}^{\beta}} e^{-(V - JR_s)/V_T}} \tag{3.1}$$

where V_T is the thermal voltage; J_{0p}^{α} and J_{0n}^{β} denote majority hole and electron currents to the α and β contacts, while j_{0n}^{α} and j_{0p}^{β} represent the minority electron and hole currents to the α and β contacts, which represent the hole and electron contacts, respectively. Moreover, a series resistance term was added to account for ohmic losses, as in [18]. The resulting IV-T curves were then fitted to (3.1) between $-0.2\,\mathrm{V}$ and $2\,\mathrm{V}$, by the self-adaptive Differential Evolution algorithm extensively discussed in the previous chapter.

Fig. 3.4 shows the JV data and the corresponding fittings for solar cells at positions 1 to 5 (a reference cell JV data was included for comparison), at STC. The leveling around $\mathrm{V_{oc}}$ and the saturation in forward bias are well reproduced with this model, resulting in the $\mathrm{J_0}$ values shown in Table 3.1.

For positions 1 to 3, the JV data could be acceptably reproduced with similar, realistic values for the currents on the p-aSi side (j_{0n}^{p-aSi} and J_{0p}^{p-aSi}). For positions 4 and 5, acceptable fitting is also obtained, but a strong decrease in the electron current to the hole contact was required to match the experimental data. There is no physical reason for this decrease since the hole contact is the same for all positions. This suggests that the strong S-shape around open-circuit-voltage of these two samples cannot be modelled with this exchange-current density formalism. Additional information about these fitting results can be found in the appendix.

As will be discussed in more details in the last section, this is indicative of a conductivity issue [77] for electron extraction, that is unrelated to the selective extraction of charges from the silicon absorber. Nevertheless, the fitted values for the electron current at the ZTGN contact (J_{0n}^{ZTGN}) were not deviating significantly from the values obtained at the other positions, since this current is indeed mostly governed by the saturation current density in forward bias, and therefore the results were kept in this work. Conversely, the hole current is mostly governed by the $\mathrm{V_{oc}}$ value, which is not well defined due to the very flat portion of the curve in this range.

The hole currents on the ZTGN side (j_{0p}^{ZTGN}) did not show major changes between positions 1 and 3, indicative of similar (poor) passivation for all these cases, with a marginal improvement for positions 4 and 5—these should however be taken with caution in view of the questionable validity of the fits as discussed above.

Conversely, some improvement was seen for the electron current to the ZTGN contact (which can be visualized on Fig. 3.4 by an increase of the value at which forward-bias

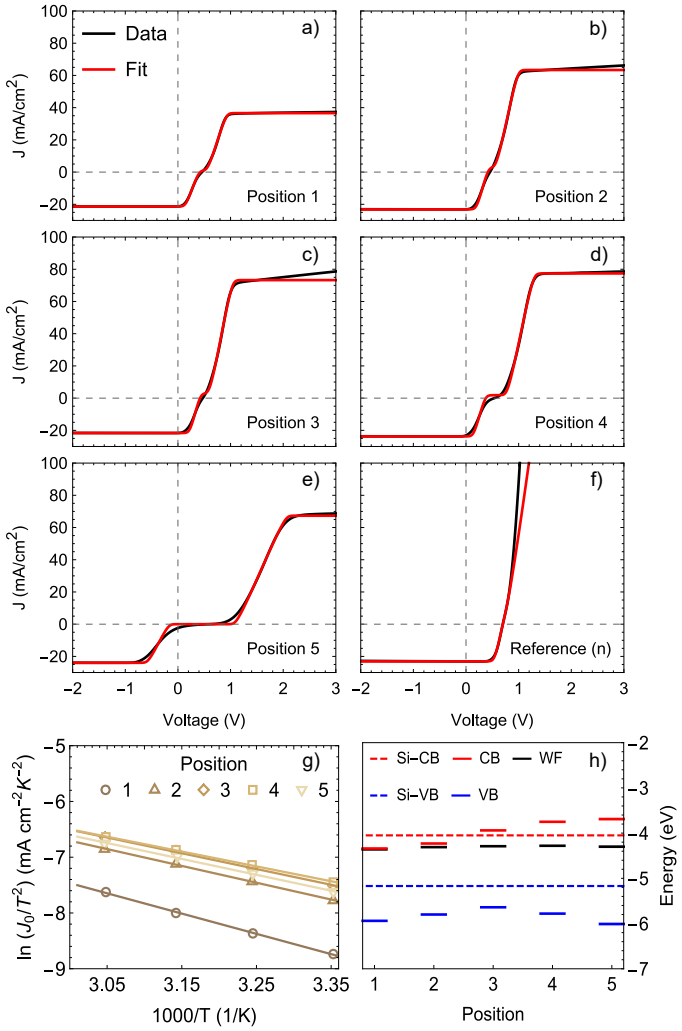

Figure 3.4 – Top: JV data and the resulting fittings to the model given in (3.1) for solar cells at positions 1 to 5 and for a reference cell, at STC. Bottom: Richardson plot of the electron current to the electron contact for solar cells at positions 1 to 5, extracted from the fittings shown in the top box, between 25 and 55 °C at 1000 W m^{-2}. A suggested band alignment between c-Si and ZTGN is also presented.

current saturates). Using the formalism of [78], the *contact* carrier selectivity can be defined by the ratio of the majority to minority carriers to a single contact (so $J_{0n}^{ZTGN}/j_{0p}^{ZTGN}$ and $J_{0p}^{p-aSi}/j_{0n}^{p-aSi}$).

Therefore, as expected the electron contact stack (ZTGN) is around 2 orders of magnitude less selective than the hole contact. Conversely, the carrier selectivity *of the device* can be defined as the ratio $J_{0n}^{ZTGN}/j_{0n}^{p-aSi}$ for electrons, and $J_{0p}^{p-aSi}/j_{0p}^{ZTGN}$ for holes, respectively. Thus, holes are the limiting carriers in these solar cells, since ZTGN could not prevent a strong hole current to the electron contact, therefore not providing enough electron selectivity for a good cell performance.

Furthermore, considering that transport of electrons to the ZTGN contact is limited by thermionic emission over the barrier at the ZTGN / n-Si interface, the electron

Table 3.1 – Equilibrium-exchange-current-density, series-resistance, and work-function values extracted from the fits shown in Fig. 3.4

	j_{0n}^{p-aSi}	J_{0p}^{p-aSi}	J_{0n}^{ZTGN}	j_{0p}^{ZTGN}	R_s	WF
		(mA/cm^2)			$(\Omega \cdot cm^2)$	(eV)
Position 1	7.02E-10	0.96	14.28	1.35E-06	7.15	4.36 ± 0.03
Position 2	1.67E-09	2.86	37.37	2.13E-06	5.08	4.31 ± 0.02
Position 3	6.11E-10	2.91	48.69	1.65E-06	4.58	4.29 ± 0.02
Position 4	4.22E-13	1.83	51.80	9.71E-06	5.13	4.28 ± 0.02
Position 5	9.89E-19	3.29E-13	43.51	2.05E-09	12.36	4.30 ± 0.04
Reference (n)	2.09E-11	6.58	2.04E+06	4.00E-12	4.04	-
Position 5 - S	3.72E-11	0.10	43.60	1.94E-06	8.44	-

exchange currents at the ZTGN contact are expected to follow

$$J_{0n}^{ZTGN} = A^* T^2 e^{-\phi/kT} \tag{3.2}$$

where A^* is the effective Richardson constant and ϕ is the barrier height, *i.e.* the difference between the n-Si electron affinity and the ZTGN work function.

As recently shown in [79], if the thermionic emission hypothesis holds, fitting IV-T to (3.1) is an effective way to estimate the work function at the contact. Therefore, we plotted in Fig. 3.4 g) the natural logarithm of J_{0n}^{ZTGN}/T^2 against $1/T$ (Richardson plot), and extracted the slope of the resulting trendline to estimate the effective work function of the electron contact for all compositions. (The fittings at 35 °C, 45 °C and 55 °C are not shown but yielded similar fitting quality to the 25 °C case).

These extracted work function values (shown in Table 3.1) shuffle around 4.3 eV, with only a marginal decrease when going from Sn-rich to Ge-rich. This corresponds to a Fermi-level position 0.25 eV below the conduction band of silicon (and 0.3 eV away from mid-gap). This renders the ZTGN layers electron selective, although not sufficiently to form a good contact as evidenced by the low obtained V_{oc} below 600 mV, as discussed in next section.

Combining this calculated work function with the activation energy and optical bandgap measurements shown in Fig. 3.1, Fig. 3.4 h) shows the reconstructed band structure of the different ZTGN alloys, and in particular the alignment with the c-Si bands. A shift of the conduction band minimum to higher energies (closer to the vacuum-level) and little movement of the valence band maximum is seen, consistently with earlier reports based on X-ray spectroscopy [68].

The relatively constant work function across variable compositions in spite of moving conduction and valence bands can be put in parallel with the InGaN alloy case. For this alloy, a similar Fermi-level position around 4.6 eV below the vacuum energy was ob-

tained upon introducing defects, independently from the alloy composition. This resulted in defective high-In-content alloys being highly conductive [80]. A similar phenomenon is indeed likely to be at play in the ZTGN family, and the samples fabricated via reactive sputtering are likely to be inherently defective.

Going further, inferring from the universal alignment of hydrogen levels in semiconductors and insulators [81], it is tempting to generalize these observations, and postulate that intrinsically conductive semiconductors (which necessarily owes their conductivity from intrinsic defects) are unlikely to perform efficiently as electron-selective contacts, since their intrinsic conductivity is inextricably linked with a too high electron affinity for this role. This would make doping a necessity to build efficient electron-selective contacts which do not rely on an elaborate combination with a low-work-function metal electrode (as in the TiO_2/Al [82] or ZnO/Al [15] cases to name a few).

3.1.3.4 Symmetric samples

Besides the arguments given in the previous section about the identification of the electron and hole currents, an experimental proof of it can be given by considering symmetric devices, i.e., solar cells fabricated with the same structure on both sides of a silicon wafer.

We fabricated three symmetrical samples, shown in Fig. 3.5. The ones on n-Si actually probe the hole extraction from the c-Si absorber to the hole contact, while those on p-Si probe how efficient is the electron extraction from the absorber to the electron contact. Additionally, one symmetrical architecture on n-Si does not feature (i) a-Si:H layers, to observe their contribution to the resulting JV curve when compared with the architecture featuring them.

It was seen that the hole current from the absorber to the hole contact results in an s-shape around $0\,\mathrm{mA\,cm^{-2}}$ in the JV characteristics, and saturation in reverse bias around $25\,\mathrm{mA\,cm^{-2}}$, as shown by architecture "pi/nSi/ip" in Fig. 3.5. The JV curves were not totally symmetrical because the rear contacts of the built solar cells were made full area whereas a metallic grid masking the ITO deposition was employed for the front-side, defining $0.49\,\mathrm{cm^2}$ cells, on which Ag paste was used to enable the external front contact.

For symmetrical samples, Eq. (3.1) reduces to

$$J(V) = -\left(J_L + J_{0n} + J_{0p}\right) + 2\frac{J_L + J_{0n} + J_{0p}}{1 + e^{-V/V_T}}, \tag{3.3}$$

since $j_{0n}^{\alpha} = J_{0n}^{\beta} = J_{0n}$ and $j_{0p}^{\beta} = J_{0p}^{\alpha} = J_{0p}$. Thus, for symmetrical samples, two steps in the JV characteristics are expected: one at reverse and one at forward bias, with same height, given by $(J_L + J_{0n} + J_{0p})$.

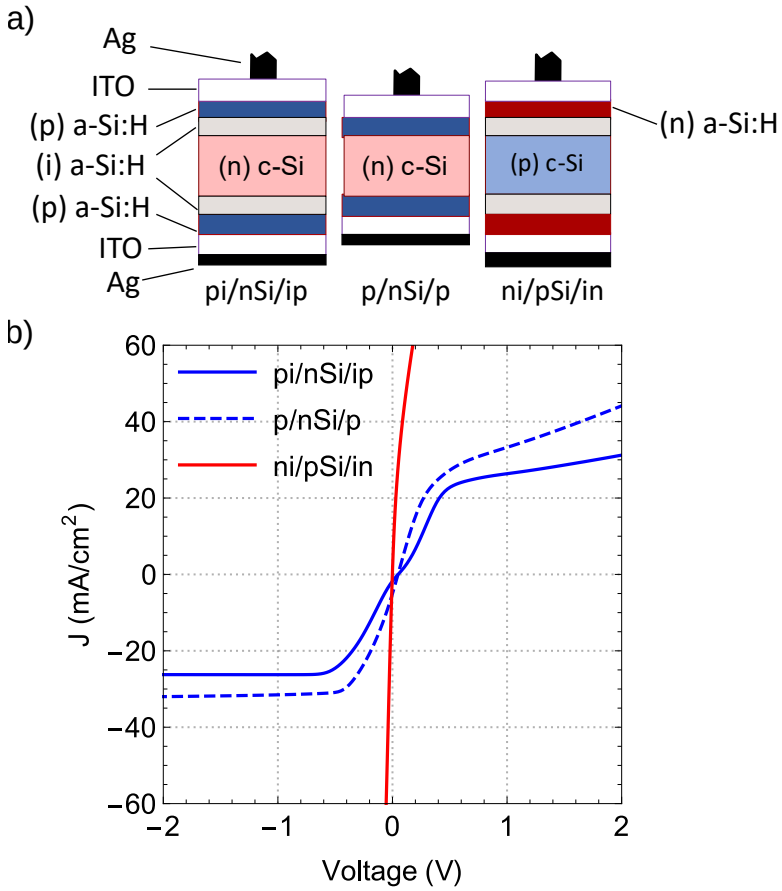

Figure 3.5 – a) Symmetrical devices fabricated on p-Si and n-Si wafers. On n-Si, one of them had no (i) a-Si:H passivating layers, to observe their contribution to the JV curves; b) resulting JV characteristics at STC.

Indeed, these two steps are observed in Fig. 3.5 for architecture "pi/nSi/ip". As this structure probes the hole current to the hole contact, due to the high resistivity faced by electrons in the (p) a-Si:H layers, $J_{0p} >> J_{0n}$ and thus the step is given $J_L + J_{0p}$. However, at reverse bias, the height of the step is approximately the photocurrent, which shows that the majority hole current to the hole contact is in fact small, close to $0\,\mathrm{mA\,cm^{-2}}$.

Thus, this analysis shows that the hole currents determined in the previous section are indeed small. Moreover, the s-shape seen for this architecture was strongly reduced upon the removal of the (i) a-Si:H layer, demonstrating that the cause for s-shapes in devices built on n-Si was the rectifying heterojunction (p) a-Si:H/(i) a-Si:H/n-Si.

On the other hand, the electron collection from the absorber to the (n) a-Si:H contacts was seen to be much more efficient, since the resulting JV curve did not show any sign of s-shapes or saturation in the explored voltage range (architecture "ni/pSi/in"), since in this case $J_{0n} >> J_L$ and $J_{0n} >> J_{0p}$.

Going further, these JV curves can be better understood with the aid of band diagrams of the interface (p/n) a-Si:H/ (i) a-Si:H/c-Si, constructed with PC1D simulations, as shown in Fig. 3.6. In a), the hole extraction from the absorber is limited by the

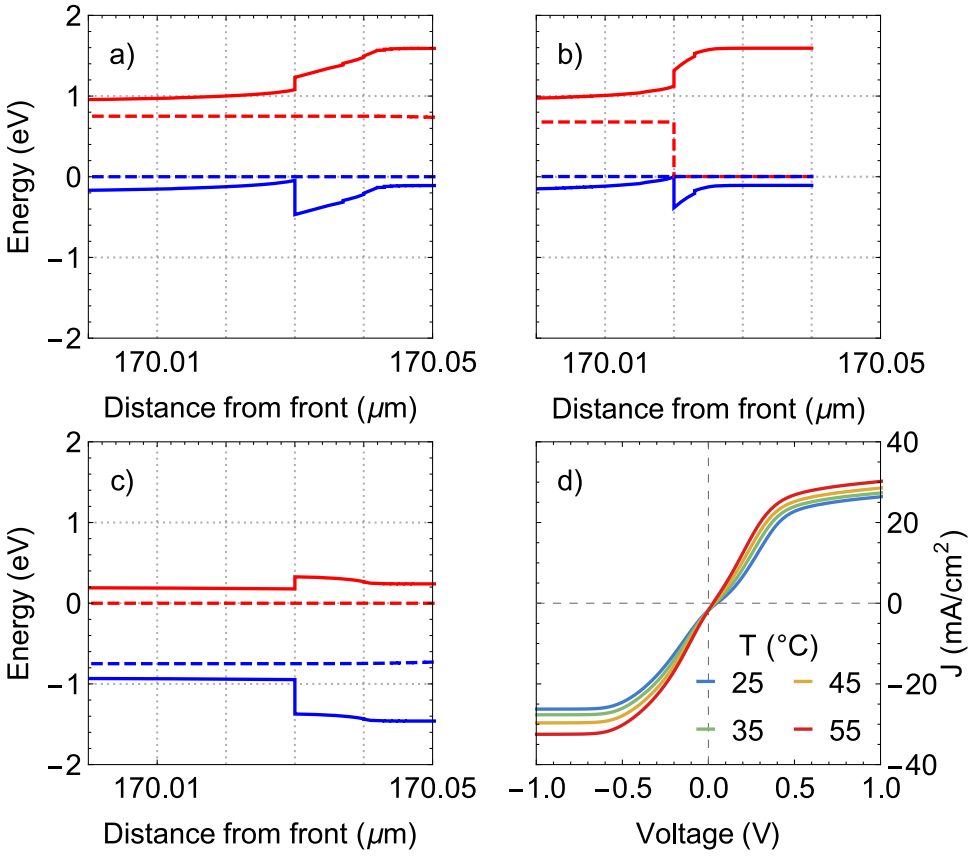

Figure 3.6 – Band diagrams at 0 V and STC for the interfaces a) c-Si/(i) a-Si:H/(p) a-Si:H; b) c-Si/(p) a-Si:H, and c) c-Si/(i) a-Si:H/(n) a-Si:H. Solid red and blue curves represent the c-Si CB and VB, respectively, while dashed red and blue lines stand for the respective electron and hole quasi-Fermi levels. Temperature-dependent JV curves at 1000 W m^{-2} for architecture "pi/nSi/ip", with band diagram represented by a).

spike of the (i) a-Si:H layer. The appearance of s-shapes at low temperatures is commonly observed for this barrier [75], but the fact that s-shapes were observed already at 25 °C suggests that this barrier was significant enough for our samples on DSP c-Si wafers, since we did not adapt the thickness of the (i) a-Si:H layer from textured to DSP wafers.

Furthermore, as expected, these s-shapes were reduced upon increasing the temperature, consistent with a thermionic emission barrier limiting hole extraction, which is seen in Fig. 3.6 (d). Removing the (i) a-Si:H passivation layer caused a reduction of the barrier height for hole extraction, as seen in Fig. 3.6 b), which results in a JV curve with a slight s-shape.

Also, Fig. 3.6 c) confirms the more efficient electron extraction, since the barrier for electrons at the interface (n) a-Si:H/ (i) a-Si:H/p-Si is much lower and can be easily surpassed by thermionic emission, resulting in a JV curve with no saturation and s-shapes, close to an ohmic behavior with low series resistance, as seen in Fig. 3.5 with architecture "ni/pSi/in".

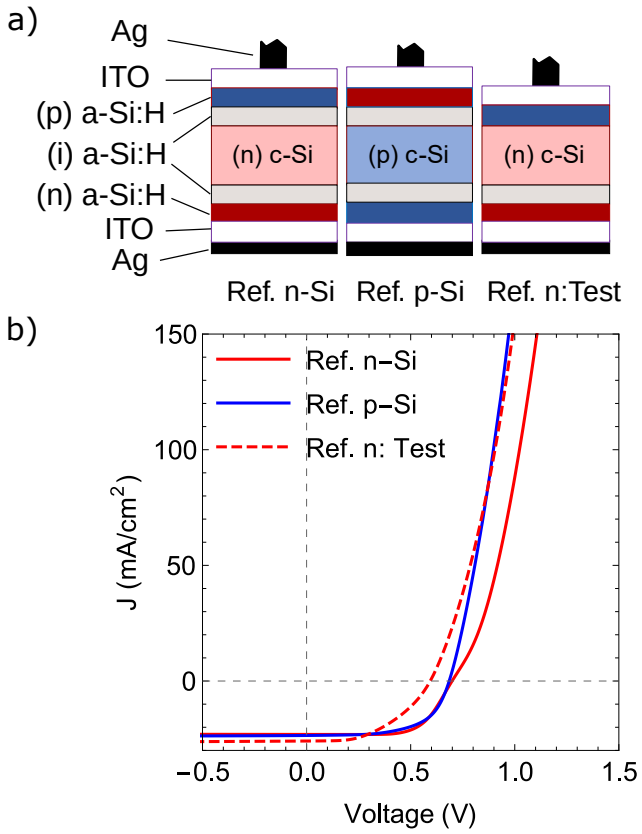

Figure 3.7 – a) Structures of the reference devices on p and n-Si, and of test device without the passivation (i) a-Si:H layer between n-Si and (p) a-Si:H; b) JV characteristics of the devices shown in a).

Therefore, the (i) a-Si:H layer in the hole contact stack plays an important role in the s-shapes observed in the JV characteristics of the reference devices built on DSP n-Si. More evidence for this can be seen with a test structure shown in Fig. 3.7, namely "Ref. n: Test", which does not feature this passivation layer, and thus the (p) a-Si:H layer is in direct contact with the silicon absorber.

In this case, it can be seen that the s-shape around the open-circuit voltage disappears, while the architecture "Ref. n-Si" features it. Despite eliminating this s-shape, the lack of passivation leads to a reduction in V_{oc} by about 110 mV, due to the formation of a defective interface between (p) a-Si:H and n-Si, which is not feasible in terms of solar cell operation, showing the need to carefully adapt the thickness of this passivation layer according to the silicon wafer type (DSP or textured).

3.1.4 Device architecture: effect of the wafer type

We now discuss the influence of the solar cell architecture, *i.e.* wafer type, with the presence or not of an (i)a-Si:H passivation layer, and of an (n)a-Si:H layer. In addition to the three architectures discussed previously and shown on Fig. 3.2, two additional architectures were compared, using a p-type silicon wafer, as shown on Fig. 3.8. A front-

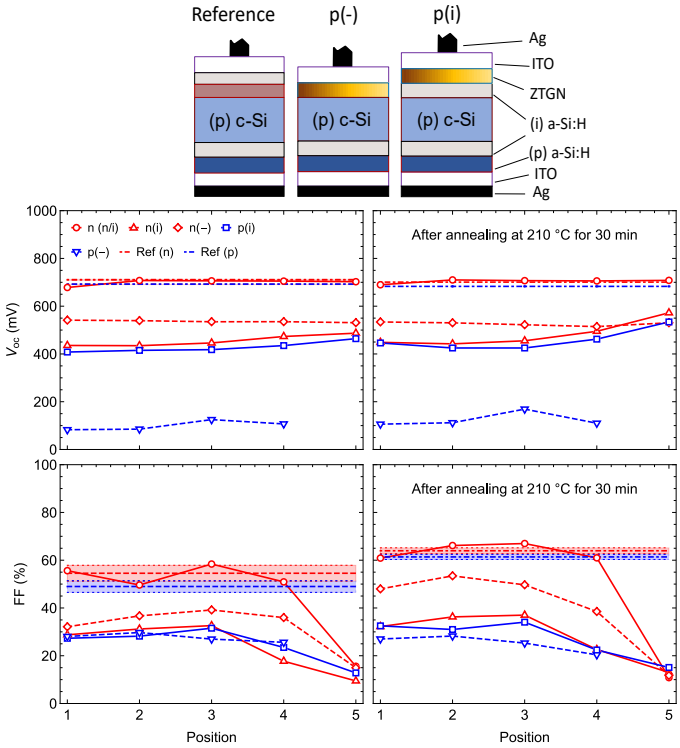

Figure 3.8 – V_{oc} and FF at STC as a function of position and device architecture. Two architectures were added, using p-type wafers. For the Ge-rich cell on p-Si, the IV curve showed a strong blocking behavior in the entire voltage range studied, and it was not possible to extract a reliable V_{oc}. Results from standard p and n SHJ solar cells are also shown for comparison. Blue and red bands denote the 95% CI for the V_{oc} (not visible) and FF from 10 SHJ reference solar cells on n and p-Si.

junction configuration was used to avoid collection issues, and the (i)a-Si:H passivation layer was used or omitted.

For cells featuring only the ZTGN layer as electron-selective contact (p(-) and n(-)), the ZTGN composition does not affect V_{oc}, but the wafer type significantly influences it, suggesting that the wafer itself is contributing to the contact behavior [77]. The strong V_{oc} difference between p(-) and n(-) devices is an indication of Fermi-level pinning at the c-Si surface, close to the (p) and (n) c-Si Fermi level, which suggests a defective interface.

For cells featuring an a-Si:H passivation layer, which enhances the role of the contact work function [83], the V_{oc} values were similar on either wafer type due to a strong increase for cells on the p-Si, but a slight decrease for cells on the n-Si. The presence of the (i) a-Si:H layer thus appears to efficiently suppress this quasi-Fermi-level pinning. The V_{oc} values were nevertheless still similar for all compositions, with a 100 mV increase towards positions 5.

Since the V_{oc} is determined by the quasi-Fermi level difference between the positive and negative contacts (and the hole contact stack is the same for all cells), this similar V_{oc} regardless the wafer type means that the quasi-Fermi levels at the electron contact

are essentially independent of composition, with a slight decrease in energy (*i.e.* moving towards vacuum energy) for samples with higher Ge content. This is consistent with the estimated work function values discussed in the previous section. Also, these V_{oc} values are in accordance with the ones obtained by Bivour *et al.* in [83], when using metal with various work-functions in direct contact to the (i)a-si:H layer.

Annealing had a mild influence on V_{oc} for all compositions, except the Ge-rich one for which a close to 100 mV increase was seen. This can be attributed to a recovery of sputtering damage, or an improvement of the electron-selectivity of the layer (e.g. decrease of work-function). The better performance in terms of V_{oc} of the Ge-rich sample when the (i)a-Si:H layer is present does not correlate with the work function extracted from the JV-curve fittings presented in previous section.

Specific care was taken to obtain accurate V_{oc} values despite the flatness of the curve around open circuit and is deemed trustworthy. Compared to the simulation results, this indeed correlates to a lower leakage of holes from these fittings (lower j_{0p}^{ZTGN}) which suggests improved passivation from this stack. This could be due to a lower defectivity of the layer, or to the fact that the valence-band edge is getting further away from the silicon one, preventing more efficiently hole recombination.

Samples including both an (i)a-Si:H and (n)a-Si:H layer under the ZTGN film showed similar V_{oc} to the reference sample, confirming that selectivity and passivation are not affected in this case. Similar FF were also measured, except for the Ge-rich case. For this composition, as also observed on Fig. 3.3, a prominent barrier to charge extraction was still observed.

Turning to FF of samples not including the (n)a-Si:H layer, low values were observed. The n(-) samples performed slightly better than the others (as also seen in Fig. 3.3), which indicates that the too high work function (low selectivity) of ZTGN is unable to screen the barrier to charge extraction imposed by the a-Si:H layer, as was the case for solar cells with ZTN as electron contacts [74].

In terms of JV characteristics, wafer type is shown to matter both for the reference contact and for the ZTGN contact. On an n-Si wafer, the JV characteristics for the latter shows a double s-shape and a saturating behavior at high forward bias. Upon changing the hole contact stack from a rectifying p-n heterojunction (p) a-Si:H/(i) a-Si:H/n-Si to an isotype heterojunction p-Si/(i) a-Si:H/(p) a-Si:H (architectures n-Si and p-Si in Fig. 3.9, respectively), the saturation at forward bias becomes a kink at 1 V followed by a drifting saturation current, with a linear dependence on the applied bias.

Interestingly, the JV characteristics of a reference device on n-Si also show an s-shape around V_{oc}, which is not seen in the JV curve of the reference device on p-Si. In a standard SHJ solar cell, the VB offset in the interface (p) a-Si:H/(i) a-Si:/n-Si and the

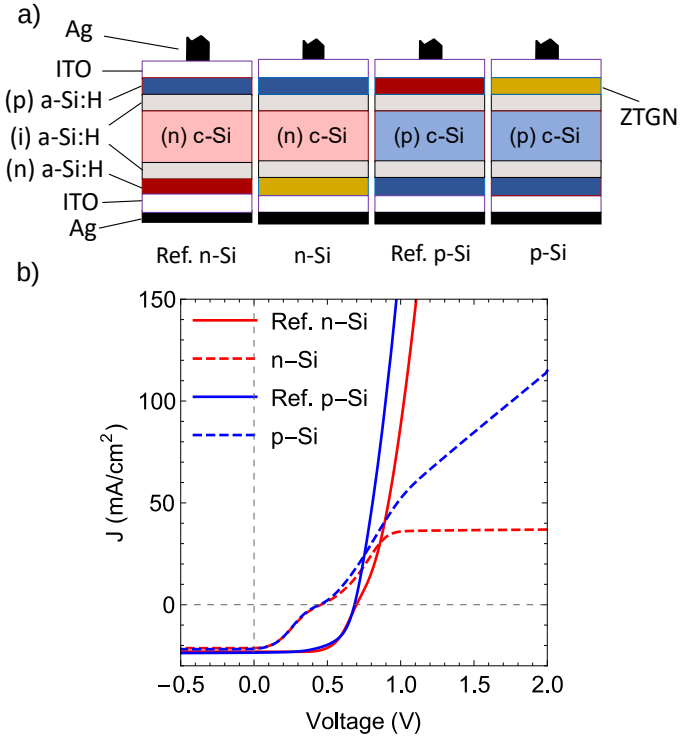

Figure 3.9 – a) Device structures of reference SHJ solar cells and test structures featuring ZTGN as electron-selective contact, replacing (n) a-Si:H; b) resulting JV characteristics at Standard Test Conditions (STC).

resulting thermionic emission barrier for holes is the limiting transport mechanism under illumination [75], which can lead to s-shapes for JV curves at low temperature and high irradiance conditions, as shown in Fig. 3.6.

Thus, considering the analysis from symmetrical samples, the s-shapes around open-circuit have actually two sources on n-Si wafers (architecture "n-Si"): from the interface with the test layer itself, but also from the hole extraction in the interface n-Si/(i) a-Si:H/(p) a-Si:H, which was shown to be limited. On the other hand, the s-shapes around V_{oc} from architecture "p-Si" have only the contribution from the ZTGN side, since the hole contact formed by (p) a-Si:H/(i) a-Si:H/p-Si does not lead to s-shapes, as seen from reference devices with p-Si.

Hence, the disappearance of the second plateau on the JV curves of the device "p-Si", which features ZTGN as electron-selective layer (Fig. 3.9) can be explained by the more efficient hole extraction when the hole contact stack is built on p-Si. This means that the second plateau can only be observed if both contacts limit device performance, which is the case of architecture "n-Si", for which electron and hole extraction are limited by thermionic emission barriers [62].

3.1.5 Discussion

As seen in Fig. 3.4, the Fermi-level of ZTGN showed only a slight decrease in energy (vacuum as reference) towards the Ge-rich sample. Upon increasing of the bandgap, the conduction band of ZTGN is therefore shifting upwards, leading to better alignment with c-si conduction band. However, since the changes in the Fermi level are much lower than the shift of the CB, the carrier density in the Ge-rich ZTGN film remains too low to make it a good electron-selective contact, leading to a strong decrease in FF. Therefore, the Sn-rich layer is a low-bandgap conductive material, whereas Ge-rich films are higher-bandgap yet insulating.

Looking at sample n(-) in Fig. 3.8 corresponding to no a-Si:H layer between the c-Si wafer and the ZTGN layer, best FF is reached for position 2. From Fig. 3.4, this corresponds to a highly doped layer with a slight negative conduction-band offset with crystalline silicon. Conversely, when a-Si:H is present (samples n(i) and n(n/i)), best FF is reached for position 3, which corresponds to a slight positive conduction-band offset with c-Si, and an approximate band alignment with a-Si:H. Deviating from these conditions leads to reduced FF, similarly to observations from [**?**] for hole-selective contacts.

To illustrate the effects of work function, doping and electron affinity on the band diagram of the n-Si/(i) a-Si:H/ZTGN, and therefore on the cell performance, simulations were carried out in PC1D considering a front-junction solar cell with three regions: hole contact/n-Si/a-Si:H/Test layer, where the test layer was making the role of Sn and Ge-rich samples.

Two illustrative situations were considered: on the one hand an unfavorable electron affinity of 4.5 eV but high doping of $1 \times 10^{19}\,\mathrm{cm}^{-3}$, representative of the Sn-rich side, and on the other hand a suitable electron affinity of 3.9 eV but low doping of $1 \times 10^{10}\,\mathrm{cm}^{-3}$, representative of the Ge-rich side.

Fig. 3.10 shows the obtained band diagrams at open-circuit condition for these two cases, for either only the studied layer as contact, or with the addition of an (i) a-Si:H layer, or with an (i/n) a-Si:H layer stack. In Fig. 6a and b, the c-Si suffered a band bending due to the work function mismatch. Moreover, in the case of Fig. 6b, an additional barrier to transport is induced by the layer itself, independent of the bending in the c-Si.

Adding an (i) a-Si:H, most of the band bending is transferred to the a-Si:H layer. Due to the additional band offset, the barrier is even slightly higher yet narrower. In Fig. 6b, the resistive nature of the test layer, due to its poor doping, becomes even more prominent than in the previous case, which correlates well with the very low FF seen in Fig. 3.8. Inserting a doped (n) a-Si:H layer does not change the barrier height, but renders it much narrower due to the high doping in the (n) a-Si:H layer.

The hole leakage towards the electron contact is also strongly decreased. This

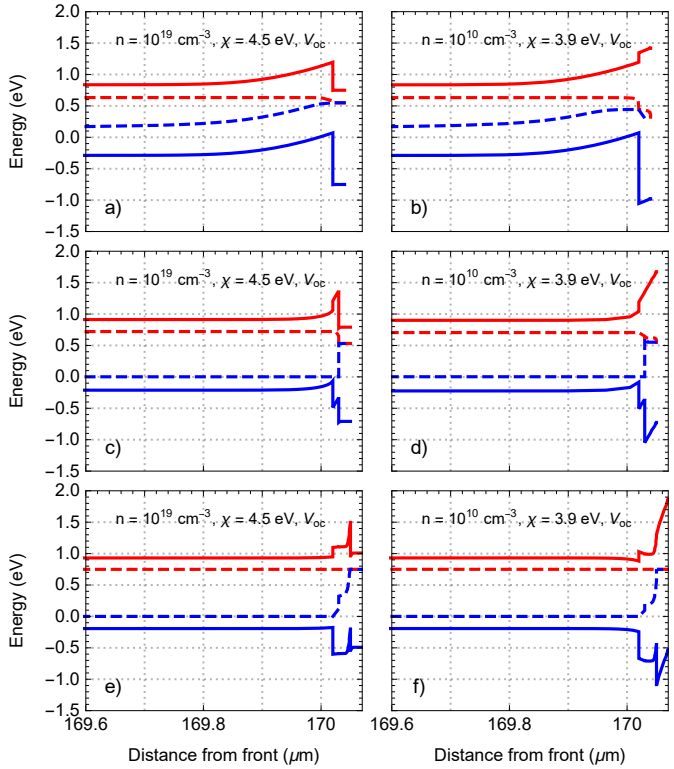

Figure 3.10 – PC1D simulations showing the band diagrams at V_{oc} for a test layer with high extrinsic electron doping and electron affinity (left column), and with low doping and electron affinity (right column), for the interface between the test layer and n-Si (a, b), n-Si/(i) a-Si:H (c, d), and n-Si/(i) a-Si:H/(n) a-Si:H (e, f). Solid lines denote CB and VB positions, while dashed lines represent the quasi-Fermi levels.

results in an increase in performance, as it was actually observed for architecture "n (n/i)" in Fig. 3. In Fig. 6e, the band diagram suggests an efficient electron-selective contact, which is what we observed. The appropriate work function of the (n) a-Si:H layer ensures electron selectivity, and its high doping screens efficiently the workfunction mismatch with the subsequent layer (mimicking here Sn-rich ZTGN, but the situation would be similar with an ITO layer).

On the other hand, in Fig. 6f, although electron selectivity is similarly granted by the (n) a-Si:H layer, the subsequent layer still imposes a barrier due to its low doping, which cannot be screened. Strong resistive losses are thus expected in all architectures for the Ge-rich solar cell, which was observed through strong s-shapes.

Thus, these simulations point that the s-shapes seen in Fig. 3.3 are caused by the barriers for electron extraction at the interface c-Si/(i) a-Si:H/ZTGN as a result of a too high work function in both cases, and additionally by the ZTGN layer itself when its doping is low, as for the Ge-rich layer. Only the latter is expected when an (n) a-Si:H layer is inserted underneath the ZTGN film. Thus going one step further in the analysis, we can separate these two barriers as one being intrinsic to the contact selectivity, and

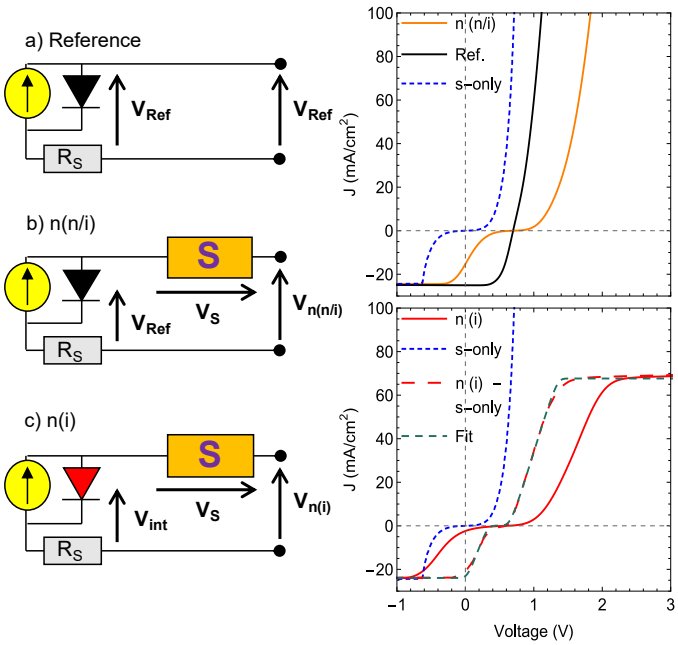

Figure 3.11 – Equivalent circuits corresponding to the reference cell (a), architectures "n (n/i)" (b) and "n (i)" (c). The s-shapes are represented by a resistor "S" in series, while the red diode represents a bad contact quality. The resulting JV curves from the operations given by (3.4) are shown in d) and e), where s-only is given by $V_{n(n/i)}(J) - V_{ref}(J)$. The dashed red curve is the JV curve of the intrinsic performance of the contact with the Ge-rich ZTGN layer.

the other one being external—thus being similar to e.g. the series resistance of the front metallic grid of the solar cell.

Considering that this is a non-Ohmic passive element in series, we can draw an equivalent circuit corresponding to the "n(n/i)", "n(i)" and "Reference" structures from Fig. 3.2. These are displayed on Fig. 3.11 a)-c), with the S-shape caused by the ZTGN layer itself being represented as a resistor with an S, and the changes in the contact selectivity being represented by a different diode color.

Using these equivalent circuits, an obvious equation to determine the intrinsic V(J) characteristic of the contact is then:

$$V_{int}(J) = V_{n(i)}(J) - (V_{n(n/i)}(J) - V_{ref}(J)) \tag{3.4}$$

Normalizing each of the JV curves, it is therefore possible to isolate the JV characteristic of the S-shape element by subtracting "Reference" from the "n(n/i)". Removing this from the "n(i)" JV curve renders the JV characteristic corresponding to the intrinsic performance of the contact.

These operations are shown in Fig. 3.11 d)-e) for the Ge-rich case (position 5), and the resulting JV characteristic is similar to the ones observed for the other four positions, as was expected from the similar value of the work function. Fitting this calculated char-

acteristic with the previously-used exchange-current model results in J_0 values shown in Table 1 as "Position 5 - S".

These are more consistent with the ones observed for Positions 1–4. Although these calculations are simplistic, and neglect e.g. the influence of the electrode, this confirms that the poor performance observed in position 5 can be split in two causes, with only one of them respecting the hypothesis of the exchange current density model, *i.e.* only one of them being an intrinsic contact selectivity issue.

3.1.6 A doping attempt

Considering that poor doping was the limiting characteristic of the Ge-rich ZTGN layer, and that a recent computational work suggested that a concentration of $n = 10^{19}\,\mathrm{cm}^{-3}$ could be achieved by doping $ZnGeN_2$ with phosphorous, due to the P_{Ge} substitutional impurity [84], we tried to incorporate phosphorous atoms on ZGN layers grown on glass by sputtering, under different atmospheres (Ar, N_2, N_2/H_2, N_2+N_2/H_2), using PH_3 plasma in H_2 and Ar atmospheres, and subsequent annealing at 300 °C, 450 °C, and 600 °C, under N_2 atmosphere for 20 min. The resulting samples were then subjected to dark conductivity measurements to check for activation energy and resistivity.

Fig. 3.12 shows the resistivity at 70 °C and activation energy extracted from Arrhenius plots, including also reference samples not subjected to the PH_3 treatment, and the corresponding values for the Ge-rich ZTGN sample. Samples not subjected to the PH_3 treatment showed the highest observed resistivity values, which were reduced after annealing at 300 °C, resulting in values similar to the Ge-rich ZTGN case.

The most promising case was for a ZGN layer grown under an N_2 sputtering atmosphere, and submitted to the PH_3 treatment under H_2, subsequently annealed at 300 °C. However, the resulting conductivity was still too high, and the activation energy similar to the Ge-rich ZTGN layer. Therefore, *ex-situ* doping was not considered successful, suggesting that *in-situ* doping is necessary.

3.2 Magnesium Tin nitride ($MgSnN_2$)

3.2.1 Motivation

Interest in $MgSnN_2$ (MTN) is also recent, with the first work addressing this compound dating back to 2016 [85], motivated by the room to explore in chemical parameter space, since these materials have two cations of different valence, and also by the fact that replacing Zn by Mg in Zn-IV-N_2 compounds could lead to bandgaps in the UV region and thus extend the electronic properties of nitrides.

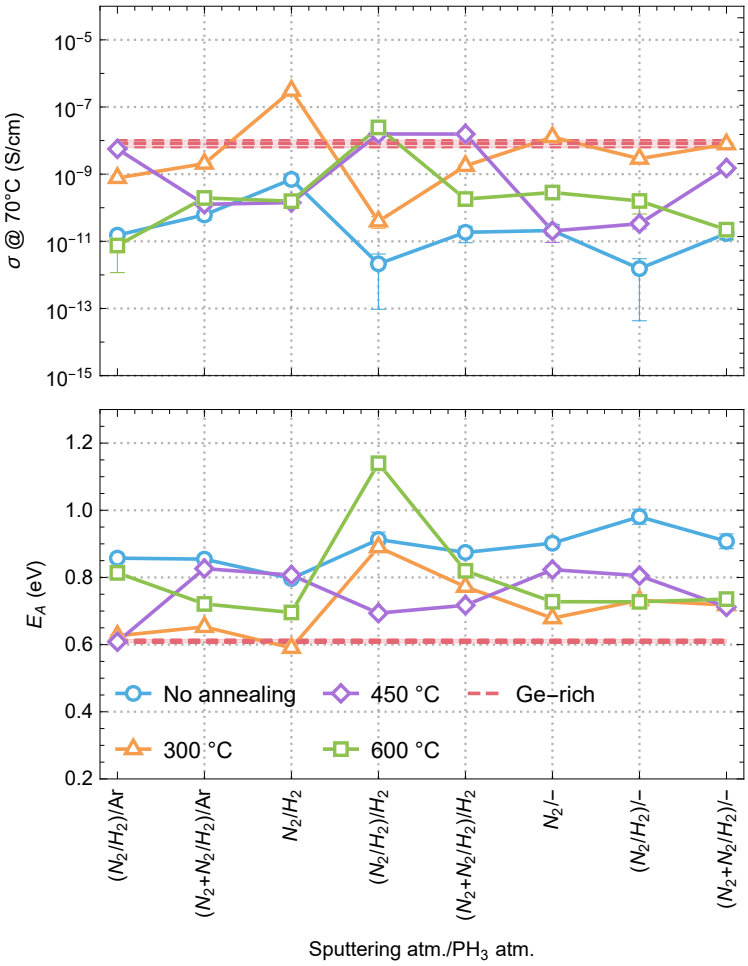

Figure 3.12 – Conductivity and activation energy extracted from Arrhenius plots for $ZnGeN_2$ layers grown under several sputtering atmospheres and subjected to different PH_3 treatment under Argon and H_2 atmospheres. The results for a Ge-rich ZTGN layer grown under N_2 and annealing at 210 °C for 30 min are also shown.

In that pioneer work [85], through a computational investigation, MTN was found to have a direct bandgap close to 3.5 eV. A couple of years later, MTN was synthesized for the first time [86], using molecular beam epitaxy, with bandgaps ranging between 1.87 eV and 3.43 eV, depending on cation ordering. Another work reported the synthesis of MTN using the metathesis reaction under high pressure and temperature [87], resulting a $MgSnN_2$ powder. Moreover, this work found a direct bandgap of 2.3 eV, in agreement to that computationally predicted in [88].

More recently, MTN was synthesized across a range of cation compositions and temperature by combinatorial sputtering [89]. A bandgap of 2.0 eV was found, consistent with cation disorder. Of special interest for this thesis, electron concentration was reported in the order of 10^{19}-10^{20} cm^{-3} at Mg/(Mg+Sn) $\approx$ 0.5 for samples grown at 300 °C and 400 °C, which places this material as an interesting candidate as electron-selective contact

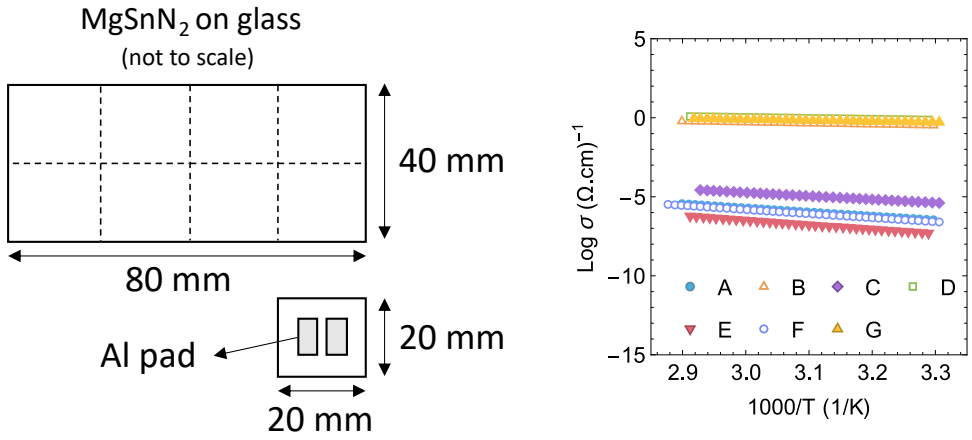

Figure 3.13 – Left: Glass slab on which $MgSnN_2$ layers were grown. The substrate was rotated during deposition. Right: dark conductivity data from seven pieces of the glass slab shown on the left picture.

for SHJ solar cells.

Given the results obtained in the previous section for ZTGN, MTN was envisioned as an interesting candidate, since it could achieve good open-circuit voltages but also higher FF, given the good electron concentrations reported in the literature, if good band alignments with c-Si could be obtained. Therefore, this section presents the fabrication details of $MgSnN_2$ layers of varying Mg/(Mg+Sn) ratio, as well as the results when applied as electron-selective contacts for SHJ solar cells.

3.2.2 Material fabrication and opto-electronic characterization

Layers of $MgSnN_2$ were initially grown on glass substrate for material characterization. For that, the powers on the Mg and Sn metallic targets were calibrated to achieve a 100 nm thick layer in approximately 40 min deposition, aiming at Mg/(Mg+Sn) $\approx$ 50% (at.%).

The deposition chamber was first evacuated to a base pressure of 1.6×10^{-7} mbar, after which a constant flow of 16.7 sccm N_2 was introduced in the chamber to achieve a working pressure of 1.3×10^{-2} mbar. Then, the powers of RF and DC generators were adjusted to 140 W DC and 65 W RF on the Mg and Sn targets, respectively. Deposition lasted for 45 min and 40 s, after a 10 min pre-sputtering step. Since a composition of 50% Mg/(Mg+Sn) was targeted, the sample holder was rotated, which should guarantee a homogeneous deposition along the substrate.

The substrate was then cleaved in several parts that were subjected to dark conductivity measurements, as described for ZTGN samples in the previous sections. Fig. 3.13 shows a schematic view of the glass substrate and the samples subjected to conductivity measurements, as well as the resulting data as function of temperature.

Table 3.2 – Thickness (from ellipsometry), resistivity at 20 °C and activation energy extracted from temperature-dependent conductivity data shown in Fig. 3.13.

Sample	Thickness (nm)	$\rho\,(\Omega\,cm)$	E_A (meV)
A	104.1 ± 0.8	737 ± 42	221.2 ± 1.1
B	98.9 ± 0.5	1.69 ± 0.04	57.1 ± 0.5
C	108.0 ± 0.8	245 ± 10	186.1 ± 0.8
D	97.1 ± 0.7	1.19 ± 0.02	49.3 ± 0.3
E	109.9 ± 0.9	1794 ± 157	244.6 ± 1.6
F	107.8 ± 0.6	836 ± 38	223.3 ± 0.9
G	100.8 ± 0.8	1.36 ± 0.03	52.3 ± 0.5

Resistivity at 25 °C and activation energy were extracted from Arrhenius plots, resulting in the data shown in Table 3.2. Thickness values were obtained from ellipsometry using the same setup for ZTGN samples. It can be seen that despite samples were all from the same deposition run, large differences in resistivity and activation energy were found, which were not consistent with a homogeneous deposition.

Nevertheless, these differences could be explained by variations in composition during deposition, since it was reported that Mg-rich samples result in lower electron concentrations, since excess Mg-rich layers include excess Mg (Mg_{Sn}) that probably behave as an acceptor-like defect, suppressing the electron concentration, while excess Sn is pointed as electron donor [90].

Thus, a detailed composition analysis was carried out to check if the composition was changing along the substrate. For that, a glass slab and also a DSP silicon wafer were positioned on the center of the substrate holder. A combinatorial mask covered both substrates, so that MTN layers would grown on symmetrical positions on glass and silicon, as shown in Fig. 3.14. Depositions at 200 °C and with no heating on the sample holder were then carried out.

Samples on glass substrate were subjected to dark conductivity and ellipsometry measurements, while the ones on silicon were subjected to EDS measurements for composition analysis, and the results are shown in Fig. 3.15. It can be seen that thickness increased towards position 4 when the substrate was not heated during deposition (room temperature - RT), which can be attributed to an increase in Mg content on the outer edges of the substrate holder, as shown by EDS data.

The increase in resistivity and activation energy with increasing Mg content, as seen in Fig. 3.15 (c), is consistent with the role of excess Mg as an acceptor-like defect, as discussed before. However, upon the increasing the substrate temperature to 200 °C, the same increase in thickness and Mg content was not observed, and the resulting samples were Sn-richer, which led to lower values of resistivity and activation energy, also consistent with [90].

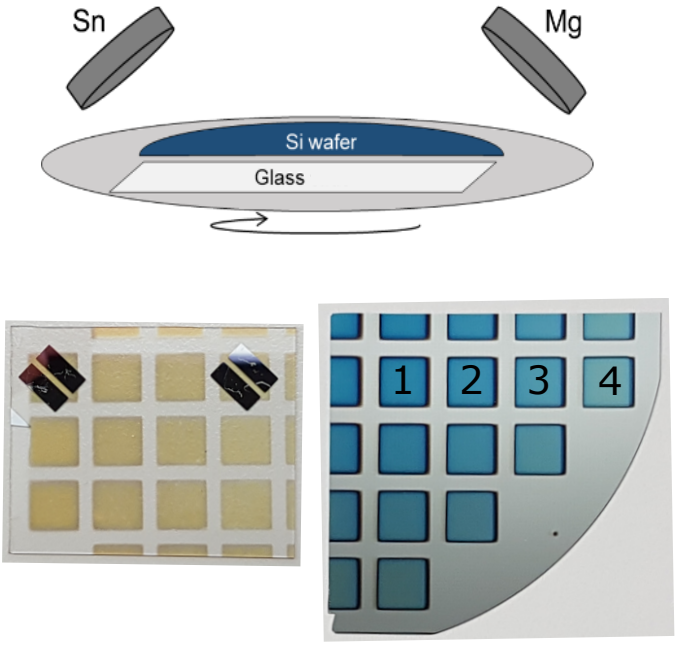

Figure 3.14 – Top: schematics showing the Sn and Mg sputtering targets relative to the positions of the substrates on the sample holder, which was rotated during deposition. MTN layers were grown on a glass substrate (left), and on a DSP Si wafer (right). Al pads were evaporated on layers grown on glass for temperature-dependent conductivity measurements.

For both growth temperatures, the E_{04} parameter shuffled around 2.0 eV, lower than what is calculated for the cation-ordered wurtzite phase [89]. However, the value measured at position 1 for MTN grown at 200 °C might be overestimated due to the conduction band filling effect, known as Burstein-Moss shift [91], given the low activation energy and resistivity found for this sample, and also that conductivity showed only a small increase with temperature. A similar behavior was found for ZTGN samples in Fig. 3.1, where a Sn-rich sample also showed a higher bandgap in spite of a higher Sn content.

Fig. 3.16 shows XRD data obtained with a PanAnalytical X'Pert Pro diffractometer, which has an incident wavelength of 1.540598 nm, from a Cu anode, and is equipped with a Ni (002) k_β filter. Four samples of MTN grown at room temperature and 200 °C on a DSP silicon wafer, with the same sputtering parameters previously mentioned, were analyzed.

Besides low layer crystallinity, Fig. 3.16 shows that for MTN grown with no heating (top), there was a coexistence of wurtzite (w) and rocksalt (rs) phases, changing from the (101)w to (111)rs, with an increase of (200)rs and decrease of (102)w peaks as the Mg content increased. Upon increasing the deposition temperature to 200 °C, only wurtzite peaks were observed in the diffractograms, which shows that the rocksalt phase disappeared. These results are consistent with [89], where no rocksalt peaks were observed neither in MTN samples grown at temperatures equal or superior to 200 °C, nor in Sn-rich

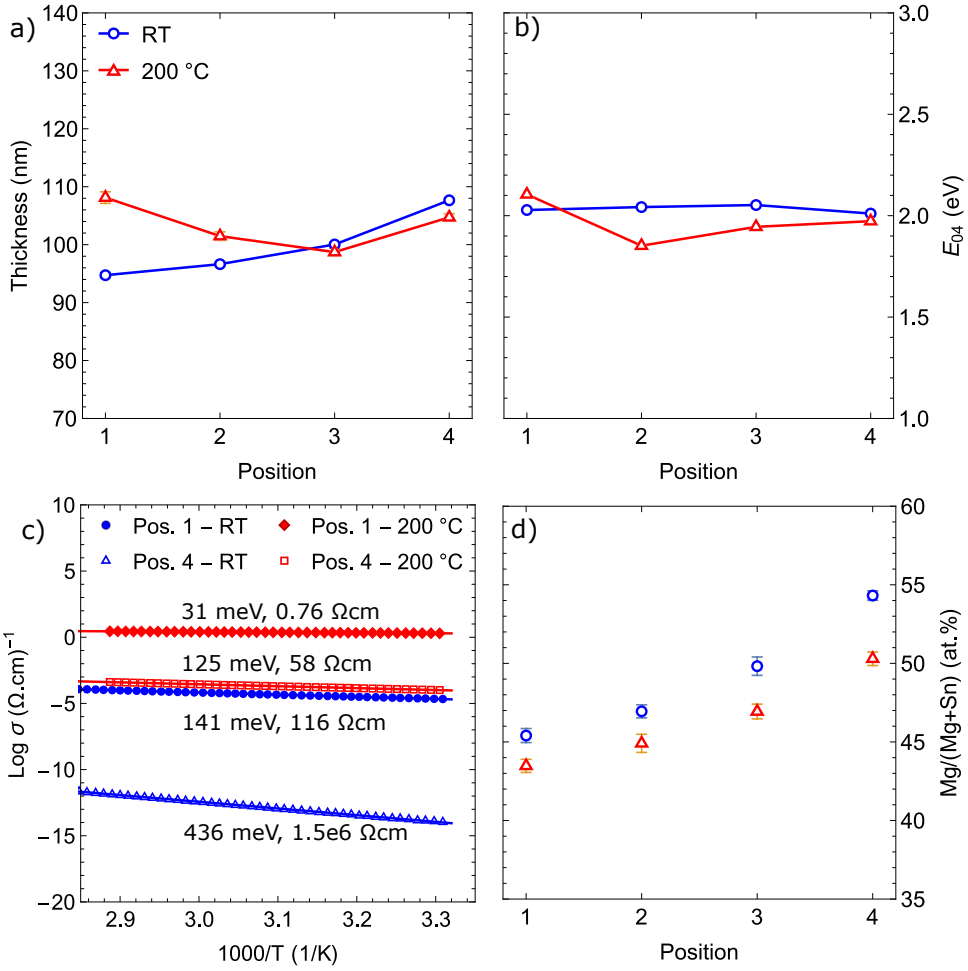

Figure 3.15 – Thickness and E_{04} (a,b) from ellipsometry measurements on glass substrate for four MTN samples, as shown in Fig. 3.14, grown with no heating (room temperature - RT), and at 200 °C. Dark conductivity data (c) and EDS measurements (d) showed that the increase in Mg content towards position 4 is accompanied by an increase in resistivity and activation energy.

samples.

In addition, images obtained by a Zeiss Gemini450 scanning electron microscope (SEM) for MTN samples grown at room temperature show an increase in triangular crystallites, consistent with columnar growth often seen in layers grown by sputtering, as the Mg content increases, which are consistent with the results recently reported in [89].

Thus, to summarize this section, it was observed that $Mg_xSn_{1-x}N_2$ layers grown under 200 °C showed a bandgap close to 2.0 eV, low resistivity and activation energy, consistent with high electron concentrations. For samples grown at room temperature, higher changes in composition were observed, leading to more resistive Mg-rich layers. Despite substrate rotation, the fabrication procedures also led to a combinatorial deposition, with composition changing between 40% and 55% Mg/(Mg+Sn) (at.%).

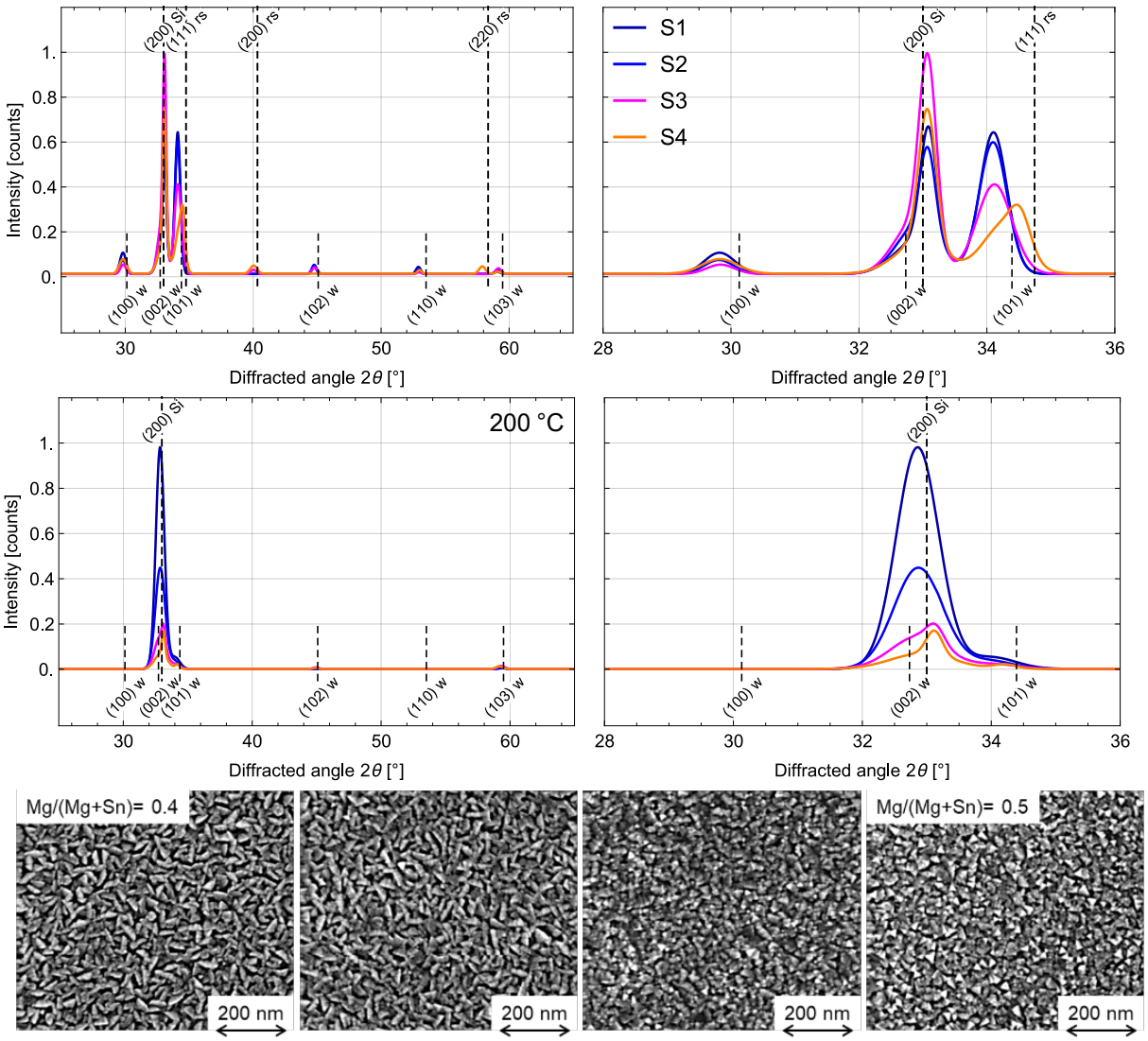

Figure 3.16 – Top: normalized X-ray diffractograms for four samples (S1-S4) of $MgSnN_2$ grown on a DSP silicon wafer with no heating, and at 200 °C (middle row). Magnesium content (at.%) increases from sample 1 (S1) to 4 (S4). Bottom: SEM images show an increase in triangular crystallites as the Mg content increases. These structures are consistent with columnar growth often seen in layers grown by sputtering [89].

3.2.3 Solar cells

After the thorough material characterization and analysis described in the previous section, $Mg_xSn_{1-x}N_2$ ($40\% < x < 55\%$) layers grown under 200 °C and with no substrate heating were employed either as passivating electron-selective contacts (on p and n-Si), as electron-selective contacts, and as spectator layer when selectivity was in charge of the (n) a-Si:H layer, which were the same structures employed when ZTGN was under investigation.

The fabrication procedures for standard layers were the same as for devices featuring ZTGN, and the sputtering time for MTN layers was reduced to approximately

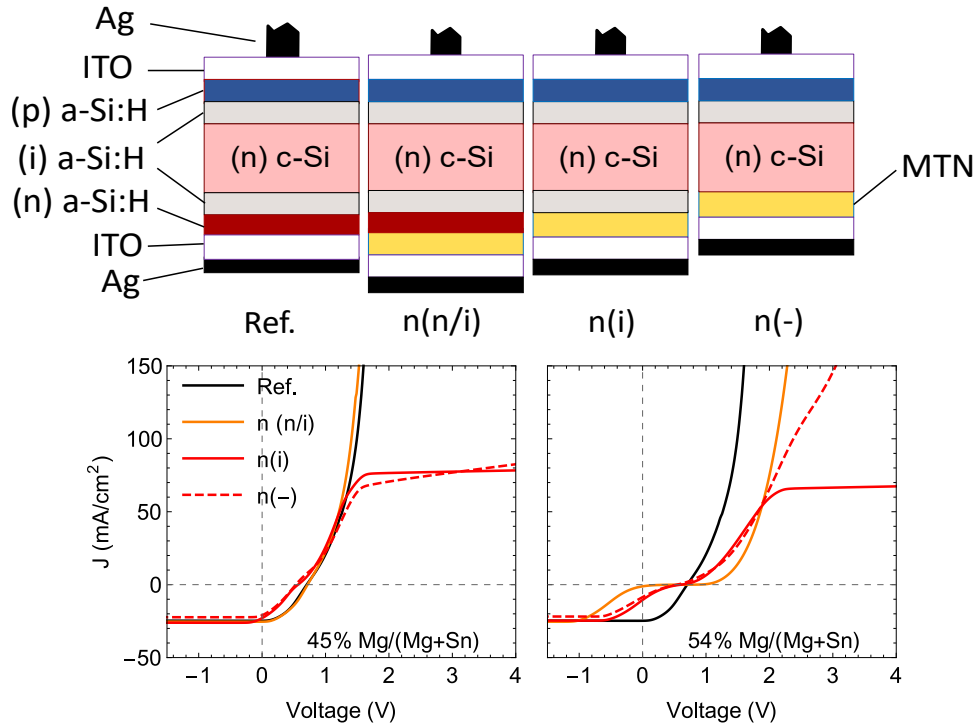

Figure 3.17 – JV characteristics (bottom) for three device architectures (top) featuring MTN as spectator layer, electron-selective contact, and passivating electron-selective contact, denoted by architectures "n(n/i)", "n(i)" and "n(-)", respectively. MTN layers were grown with no heating, and all devices were annealed at 210 °C for 30 min before characterization. A reference device is also included for comparison.

10 min, targeting 20 nm layers, as for ZTGN. Four solar cells were fabricated on the same positions as the ones depicted in Fig. 3.14, while composition of MTN layers on these four positions is shown in 3.15 (d). Furthermore, all devices were subjected to annealing at 210 °C for 30 min before IV characterization, except the ones with MTN grown at high temperature, which were characterized before and after this annealing procedure.

Fig. 3.17 shows the device architectures featuring MTN, as well as the resulting JV characteristics for solar cells with 45% and 54% Mg/(Mg+Sn) (at.%), which are representative of all other JV characteristics. It can be seen that MTN showed a similar behavior to ZTGN, with a saturation and drifting current at forward bias for architectures "n(i)" and "n(-)", respectively. Moreover, solar cells at position 4 in Fig. 3.14, corresponding to approximately 54% Mg/(Mg+Sn), exhibited stronger s-shapes around 0 mA cm^{-2}, similarly to the Ge-rich ZTGN case, previously discussed.

For architecture "n(n/i)", where selectivity was in charge of the (n) a-Si:H layer, good performance was observed for the solar cell at position 1, with 45% Mg/(Mg+Sn), which showed a similar JV curve to the reference device, with no saturation at forward bias. However, for the Mg-rich solar cell, a strong s-shape was still seen, but the saturation at forward bias disappeared as well.

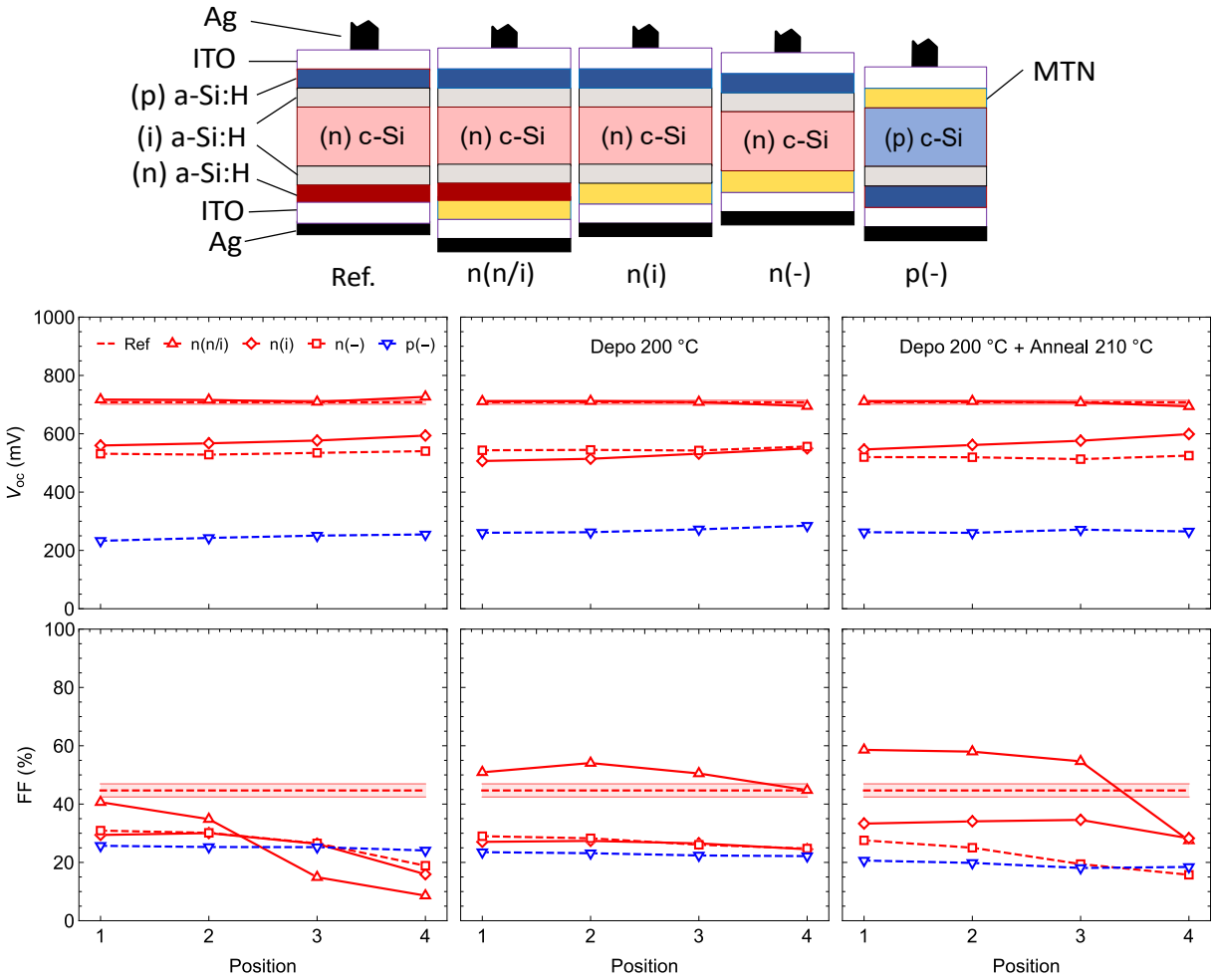

Figure 3.18 – V_{oc} and FF obtained for several device architectures featuring $MgSnN_2$ grown at room temperature and then annealed at 210 °C for 30 min (first column); for MTN grown at 200 °C with no annealing (middle column), and then annealed (last column). An additional architecture, on p-Si, was also included to observe if the resulting V_{oc} would be similar to that for ZTGN, which could point to a Fermi level pinning around the (p) c-Si Fermi level. The reference device was characterized after annealing.

More similarities with ZTGN can be seen by looking at Fig. 3.18, which shows V_{oc} and FF values obtained for several device architectures, including an additional one on p-Si, to check for Fermi-level pinning when comparing with architecture "n(-)", since both do not have the passivating (i) a-Si:H layer between MTN and c-Si. Also, different MTN growth and device conditions were studied: devices with MTN grown at room temperature and subsequent annealing (first column), and with MTN grown at 200 °C and no annealing (middle column), which were then annealed (last column). The reference device was annealed before IV characterization.

When the passivating (i) a-Si:H was not present — architectures "n(-)" and "p(-)" —, open-circuit voltages between 500 mV and 550 mV were observed for devices on n-Si, decreasing to values around 250 mV on p-Si. Furthermore, these values were not affected

by variations in Mg content. Interestingly, the V_{oc} values on n-Si were roughly the same as the ones obtained when ZTGN was in direct contact with n-Si. Considering that in the absence of the passivating layer there is a defective interface formed between MTN and c-Si, these values point to a Fermi-level pinning around the c-Si Fermi level, close to those observed for ZTGN.

Again, changes in composition did not lead to significant changes in V_{oc}, which was always between 500 mV and 600 mV, with the highest value of 599 mV found for the solar cell at position 4 when MTN was grown at 200 °C and the device subjected to annealing.

When MTN was applied just as spectator layer, leaving electron selectivity in charge of the (n) a-Si:H layer, good V_{oc} values were obtained, similar to that from the reference device, showing again that the appropriate work function of the (n) a-Si:H layer can efficiently screen the work function mismatch with the subsequent layer. If this last layer has a good conductivity, which is the case of Sn-rich MTN (position 1), a FF close or even higher than that of the reference device can be observed. On the other hand, the poor doping of the Mg-rich MTN (position 4) imposes an additional barrier to electron extraction, resulting in a low fill factor and in a strongly s-shaped JV curve, as seen in Fig. 3.17.

For MTN grown at room temperature (first column of Fig. 3.18), FF values decrease towards position 4 due to the increase in Mg content, which leads to increased resistivity and activation energy, as seen in Fig. 3.15. But when MTN was grown at high temperature, this same decrease was not seen since this growth condition implied in a higher Sn content, enhancing conductivity. Moreover, annealing the devices with MTN grown at high temperature recovered sputtering damages, since there were gains in both V_{oc} and FF were observed.

However, after the devices with MTN grown at 200 °C were annealead, a sharp decrease in FF was observed for architecture "n(n/i)" from position 3 to 4, which is not consistent to the decrease observed due to the increase in Mg content (middle column), since before annealing the FF was still close to the reference device. Since MTN was already grown at 200 °C, further annealing the wafer at 210 °C might have damaged this solar cell.

It is interesting to note that the devices with MTN grown at high temperature and employed only as spectator layer showed superior performances than the reference device. The same was observed for some solar cells featuring ZTGN, which implies that these materials might be well suited as a buffer layer for electron transport, if well optimized for this purpose.

Fig. 3.19 shows V_{oc} and FF extracted from SHJ solar cells featuring ZTGN and MTN as electron-selective contacts — architecture "n(i)". Note that position 1-5 denote

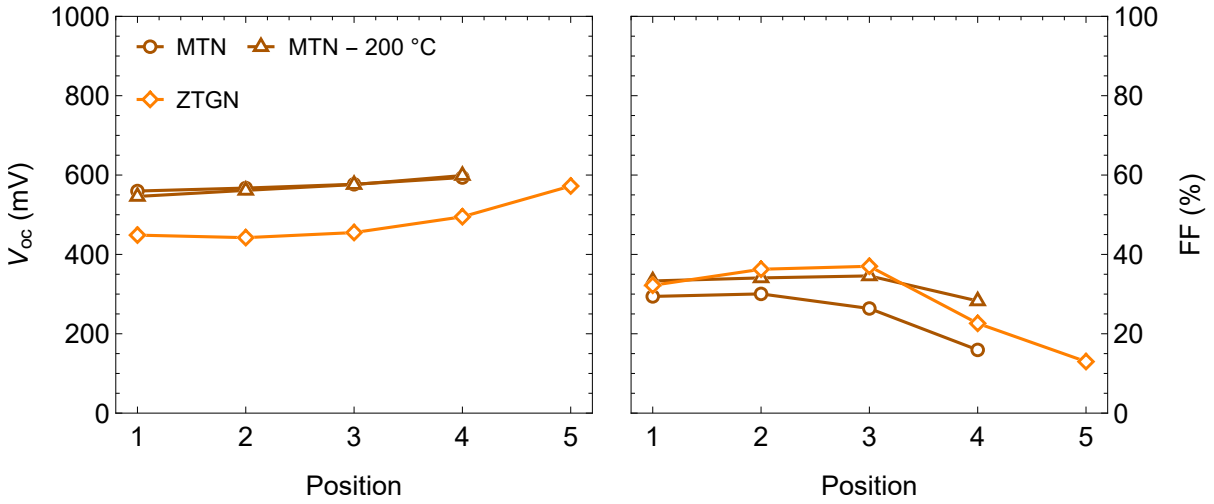

Figure 3.19 – V_{oc} and FF obtained for SHJ solar cells featuring ZTGN and MTN as electron-selective contacts. All devices were annealed at 210 °C for 30 min.

the previous positions for the five and four solar cells with ZTGN and MTN, respectively. Thus, compositions for these positions are not the same, although the results are grouped by position.

SHJ solar cells with MTN showed higher V_{oc} than the ones with ZTGN, especially for Sn-rich MTN layers (for Ge and Mg-rich layers, lower differences in V_{oc} were observed), pointing that the work function of MTN is lower (towards vacuum energy level) than ZTGN, since the hole contact stack was the same for all devices. In terms of FF, both materials resulted in similarly poor values.

Thus, all these results suggest that the same limiting mechanisms are in place when MTN and ZTGN are employed as electron-selective contacts: work function mismatch, causing a thermionic emission barrier for electron extraction, and an additional barrier due to poor doping of Mg and Ge-rich layers.

To check if this was indeed the case for MTN, the same analysis of JV-T curves and thermionic emission modelling, as applied to SHJ solar cells featuring ZTGN, was carried out for devices featuring MTN as electron-selective contacts — architecture "n(i)", for MTN layers grown at room temperature.

It is seen in Fig. 3.20 that, again, the current at forward bias is very well fitted by the model. However, if the s-shape around open-circuit gets stronger, the model fails to accurately describe the experimental data. Additionally, the JV characteristics change their slope as it goes from the power quadrant to the first quadrant, just before saturation at forward bias. Since only one term was used to model the lumped series resistance, the fitted JV curve does not fit the data accurately in the power quadrant region.

However, the J_{0n}^{MTN} current is well fitted, and thus can be approximated by the difference between the current at forward bias and the photocurrent, i.e., $J_{0n}^{MTN} =$

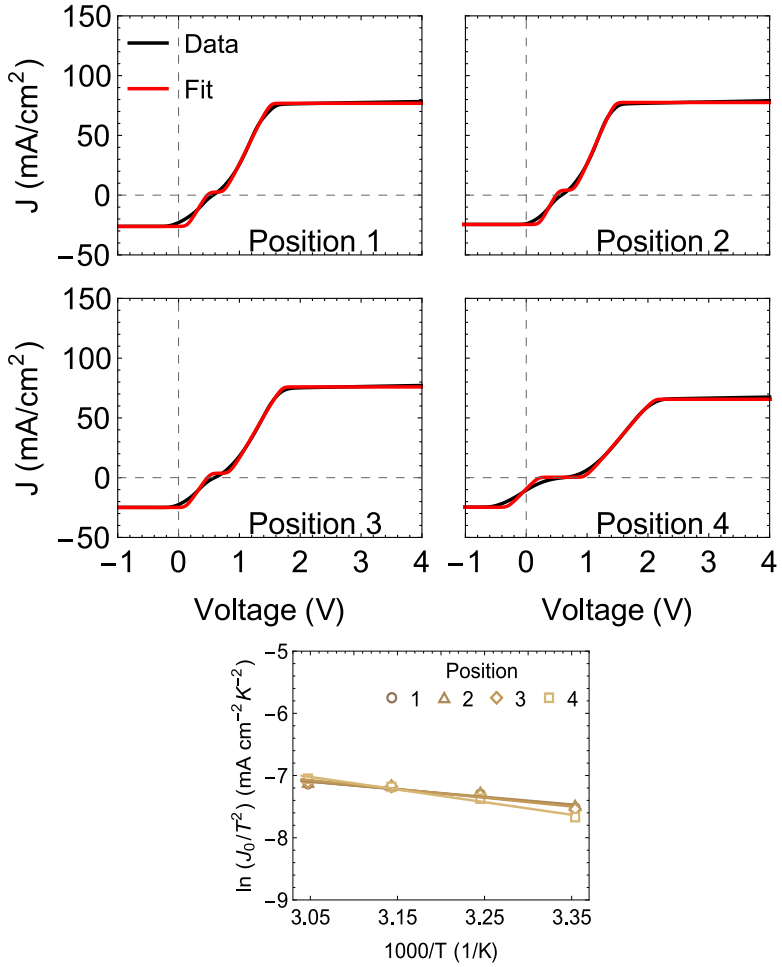

Figure 3.20 – Top: JV data and the resulting fittings to the model given by Eq. (3.1) for solar cells featuring MTN as electron-selective contact — architecture 'n(i)" — at positions 1-4, at STC. Bottom: Richardson plots of the electron current to the electron contact, extracted from the fittings shown for positions 1-4, between 25 °C and 55 °C, at 1000 W cm^{-2}.

$J_{saturation} - J_L$, since the hole current to the hole contact is small. Since both parameters are well defined, the analysis by Richardson plots is not affected. Thus, following the fitting procedure, the estimated work function was extracted from the Richardson plots of the electron current to the electron contact. Fig. 3.21 show the suggested band alignment between c-Si and the electron contact of SHJ solar cells featuring MTN grown at room temperature. The values obtained for ZTGN compounds are also shown for comparison.

The work function values obtained for the studied MTN layers grown with no substrate heating were slightly lower (towards vacuum level) than those obtained for ZTGN layers, which can account for the higher V_{oc} observed when MTN was tested as electron-selective contact, as it was suspected. Moreover, it is interesting to note the distribution of the band diagrams for $ZnSn_xGe_{1-x}N_2$ alloys and $Mg_xSn_{1-x}N_2$, with all work function values between the Sn-rich ZTGN and Sn-rich MTN, with an average of (4.27 ± 0.06) eV.

In the case of MTN, the whole bandgapmoved towards the vacuum level as the

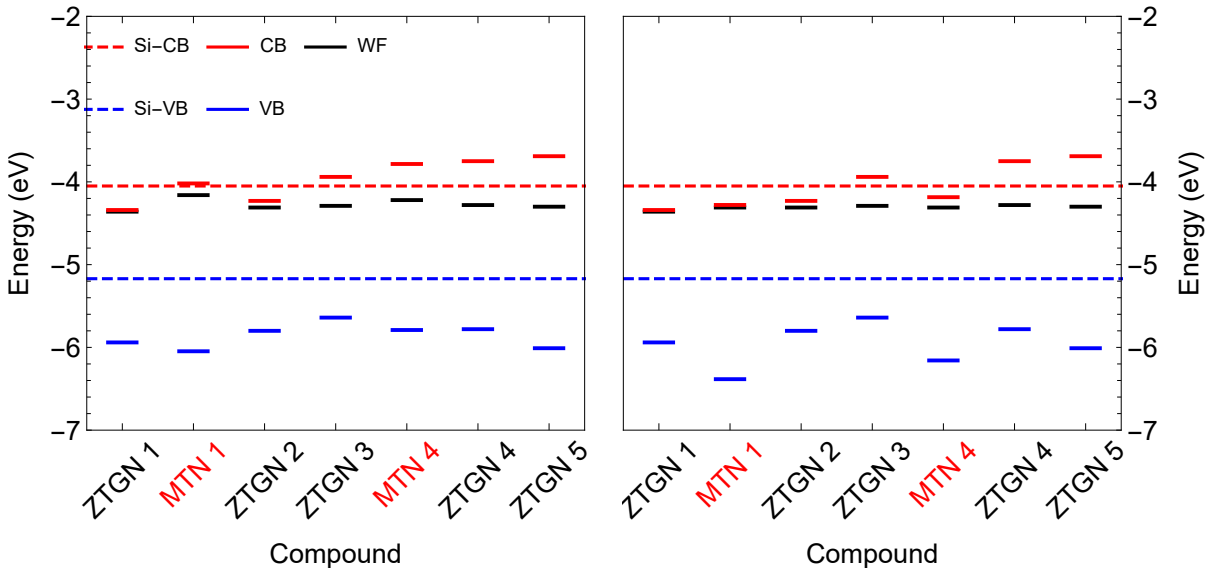

Figure 3.21 – Suggested band alignment between c-Si and electron contacts of SHJ solar cells featuring five ZTGN and two MTN compositions (at room temperature - left, and 200 °C - right), as discussed in the text.

Mg content increased, while in the ZTGN case the CB minimum moved towards the vacuum level as the Ge content increased. It has to be mentioned that these values were not experimentally measured but result from a mathematical modelling, being indirect measurements, and care should be taken when interpreting these values.

Moreover, for MTN layers grown at 200 °C, the valence and conduction bands were pushed down, away from the vacuum level. As a result, the VB offset with c-Si increased, which can explain why the V_{oc} values for solar cells with MTN at high temperature were still basically the same as for MTN at room temperature, despite these layers had higher work functions.

Considering that the MTN layers grown at 200 °C were Sn-richer, and therefore showed lower activation energy and resistivity than the ones grown with no heating, these results indeed suggest that intrinsically conductive semiconductors have high work function values, making the CB close to the Fermi level, as discussed for ZTGN layers.

3.3 Conclusions

This chapter initially reported the characterization of ZTGN layers on glass and the performance assessment of SHJ solar cells featuring these layers as electron-selective contacts. In the investigated composition range, bandgap was shown to be tunable between 1.6 eV and 2.3 eV and conductivity and activation energy from 7 S cm^{-1} and 17 meV to 2.5×10^{-10} S cm^{-1} and 610 meV, respectively. Nevertheless, for all compositions, ZTGN performs similarly as electron-selective contact with low V_{oc} (between 450 mV and 580 mV)

and FF.

Following an exchange-current modeling, the poor electron-selective ability of these layers can be attributed to the ZTGN work function being around 4.3 eV, *i.e.* within the silicon bandgap, independently of the Sn and Ge contents. The Sn-rich composition is suggested to be limited by its too high electron affinity, whereas the Ge-rich composition combines a too low electron affinity with a too low doping (too high activation energy). This causes two different barriers for electron extraction, one being intrinsic to the selectivity of the contact and originating from unfavorable band bending in the silicon itself, and the other being external and due to the resistivity of the layer itself.

After having identified the reasons limiting an efficient electron extraction in devices featuring ZTGN, $MgSnN_2$ (MTN) was envisioned as a good candidate, since it was expected to have good doping levels and a suitable bandgap. Thus, MTN layers were fabricated by a combinatorial sputtering approach, with no heating and at 200 °C, confirming high doping levels for Sn-rich MTN samples, which decreased towards Mg-rich oens, with no significant changes in bandgap, which was estimated as being close to 2 eV, in agreement with recent results reported in the literature.

When MTN layers were applied as electron-selective contacts in SHJ solar cells, only a marginal improvement in performance was seen when compared to devices featuring ZTGN. Strong s-shapes, similar to those obtained for Ge-rich ZTGN, were obtained for devices featuring Mg-rich layers, which showed a high resistivity, while devices with Sn-rich MTN showed lighter s-shapes, also similar to the ones obtained for ZTGN. Furthermore, saturation of the JV characteristics at forward bias was again observed. Also, strong Fermi-level pinning at the c-Si interface was observed when ZTGN or MTN layers were in direct contact with the wafer, which was effectively suppressed when inserting an intrinsic a-Si:H layer.

Following the same exchange-current modeling, the effective work function of the electron contact featuring MTN was estimated as being around 4.16 eV, which was pushed to 4.3 eV for more conductive layers, along with conduction and valence bands. These results suggest that the effective work function of the electron-selective contact lies around 4.3 eV when ZTGN or MTN are employed as electron-selective layers in SHJ solar cells, with Sn-rich samples showing high electron affinities, and Ge/Mg-rich ones having poor doping levels.

This work function mismatch with c-Si causes a gradient in the electron quasi-Fermi level in the electron contact, and induces a parasitic band bending in the absorber, causing an increase in hole concentration in the c-Si close to the electron contact, lowering the electron to hole ratio, which reduces the contact selectivity due to enhanced recombination. Hence, the implied voltage generated in the c-Si absorber is considerably dropped to the observed low open-circuit voltage values that were extracted from the

devices studied in this work.

Thus, since these semiconductors are conductive due to intrinsic defects, a way to increase the performance of solar cells featuring these layers would be to dope Ge-rich ZTGN and Mg-rich MTN layers with extrinsic elements, shifting their work functions to lower levels (V_{oc} improvement), improving conductivity and hence reducing the strong s-shapes observed for these compositions (FF improvement).

4 General conclusions and prospects

The search for new materials that could replace the a-Si:H layers as electron-selective contacts in SHJ solar cells is not an easy task, as it was shown in this work. Besides having high electron concentration to ensure good conductivity for majority electrons and high resistivity for minority holes, work function matching, minor and high CB and VB offsets with c-Si are additional properties that must be satisfied by these materials.

Data from several structures of SHJ solar cells featuring ZTGN and MTN as electron-selective layers strongly suggested that a thermionic emission barrier is hindering an efficient electron extraction due to work function mismatches with c-Si, resulting in a gradient in the electron quasi-Fermi level in the electron contact and parasitic band bending in the absorber, enhancing the hole concentration and reducing the electron to hole ratio in the vicinity of the contact, decreasing its selectivity. Thus, the voltage generated in the c-Si absorber could not be fully extracted, resulting in low V_{oc} obtained for devices featuring either ZTGN or MTN.

Despite having tunable band gap and electron concentration as a function of stoichiometry, the effective work function of the electron selective contact featuring ZTGN or MTN was found to not be tunable, always lying around 4.3 eV, accompanied by a too high electron affinity when conductivity was high. Even though better CB offsets could be achieved upon changes in stoichiometry, the non-moving work function resulted in poorly doped layers, which then imposed an additional barrier to electron extraction, strongly affecting the fill factor on the device level. Therefore, doping these layers with extrinsic elements could then move their work functions and result in better solar cell performance.

Considering that ZTGN and MTN own their conductivities to intrinsic defects, and the similar open-circuit voltages obtained in this work, further studies could investigate in more detail the position of the work function in these semiconductors, and also their band alignments with silicon. Perhaps the work function of all these ternary nitride semiconductors and their alloys lie around the same position, making extrinsic doping a necessity to build efficient solar cells featuring these materials as electron-selective contacts.

Moreover, it was shown how important it is to find computational methods that can effectively extract parameters from solar cell JV data. Also, since huge datasets are commonly involved in this modelling procedure, methods that can be easily automated, with low or no supervision by the user, such as metaheuristics, can be valuable tools if properly evaluated, especially considering the presence of noisy data.

Hence, research on simple yet powerful stochastic optimization algorithms that

can automatically regulate the search process is a fruitful research field, especially if these methods are applied to the PV parameter extraction problem, considering the abundance of diode models available in the literature.

Finally, anomalous JV curves are now commonly reported in the literature as the research in new materials for solar cells moves forward, and many models describing these curves can be found. However, a unified explanation, experimentally validated, has not been published yet.

Appendix

APPENDIX A – Error maps for the exchange current density modelling

As discussed in Chapter 3, fitting the JV characteristics with the exchange current density model resulted in good fittings for Sn-rich compositions. As the Ge-content (and layer resistivity) increased, the fittings started to show accuracy issues around the flat part of the JV characteristics, close to 0 mA cm^{-2}. Despite these problems, the saturating current at forward bias was always well fitted, and since this region was used for the thermionic emission modelling, those fitting issues were not problematic for the analysis carried out in this work.

Since the hole step occurs close to zero current, it can be difficult to determine the hole current densities, since even the majority hole current is small. However, for the Sn-rich ZTGN solar cell (Position 1 in Table 3.1 and Fig. 3.4), the Differential Evolution algorithm used to fit the data was capable of finding well defined parameters, resulting in a good matching between the fit and the experimental data.

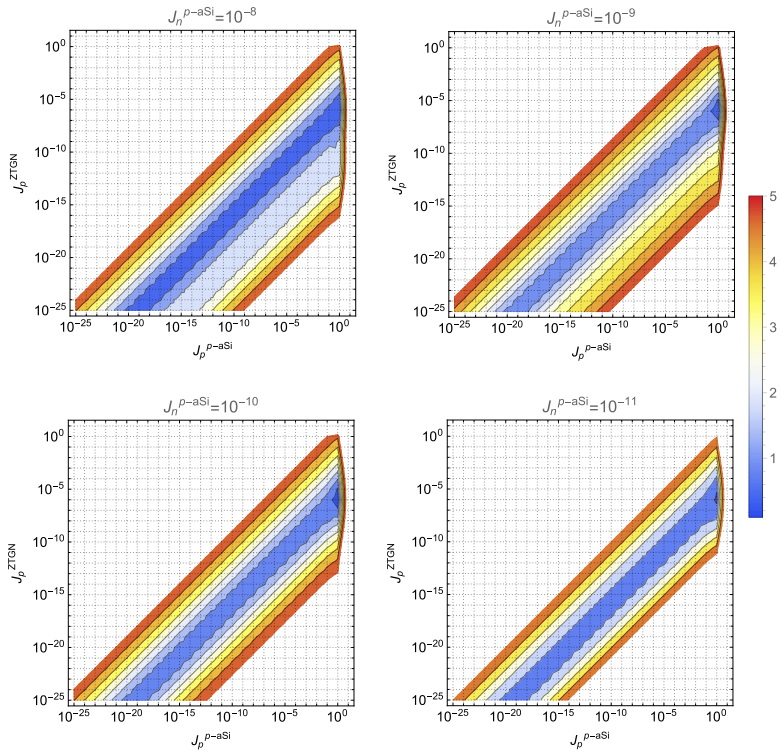

Figure A.1 – Maps of the Root Mean Square Error (RMSE) between experimental and fitted JV data for the solar cell at position 1 (Sn-rich ZTGN), for varying j_{0p}^{ZTGN}, $J_{0p}^{p\text{-}aSi}$, and $j_{0n}^{p\text{-}aSi}$, considering J_{0n}^{ZTGN} and R_s well defined and given in Table 3.1.

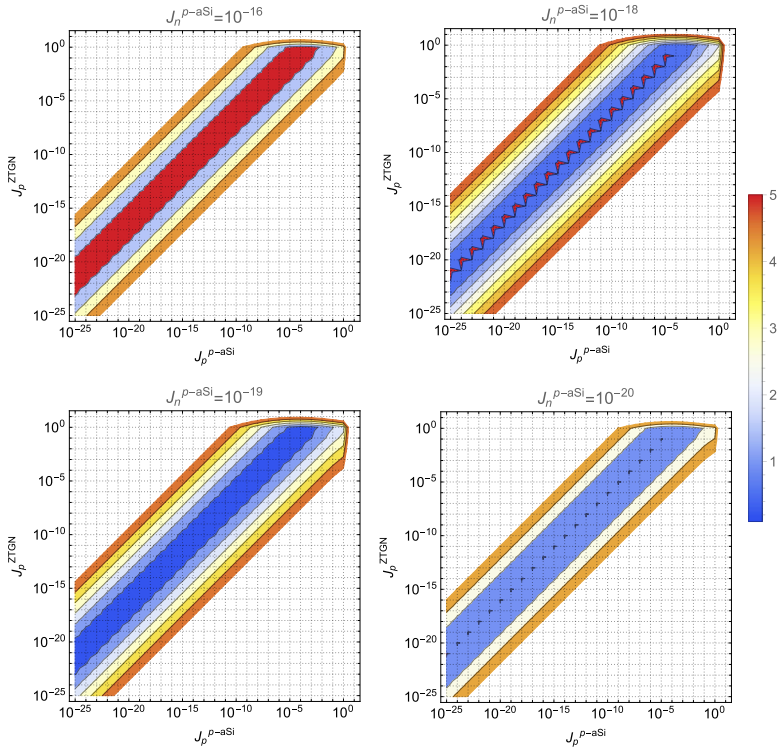

Figure A.2 – Maps of the Root Mean Square Error (RMSE) between experimental and fitted JV data for the solar cell at position 5 (Ge-rich ZTGN), for varying $j_{0p}{}^{ZTGN}$, $J_{0p}{}^{p\text{-}aSi}$, and $j_{0n}{}^{p\text{-}aSi}$, considering $J_{0n}{}^{ZTGN}$ and R_s well defined and given in Table 3.1.

Fig. A.1 shows maps of the Root Mean Square Error (RMSE) between experimental and fitted data, for varying $j_{0p}{}^{ZTGN}$, $J_{0p}{}^{p\text{-}aSi}$, and $j_{0n}{}^{p\text{-}aSi}$, considering $J_{0n}{}^{ZTGN}$ and R_s well defined and equal to $14.28\,mA\,cm^{-2}$ and $7.15\,\Omega\,cm^2$, respectively. There is clearly a small optimal region, where $10^{-10} < j_{0n}{}^{p\text{-}aSi} < 10^{-9}$, $J_{0p}{}^{p\text{-}aSi} \approx 1\,mA\,cm^{-2}$, and $j_{0p}{}^{ZTGN} \approx 10^{-6}\,mA\,cm^{-2}$, for which the RMSE has a minimum value, and thus the algorithm was capable of finding this optimal region.

On the other hand, the same is not valid for position 5, which has a Ge-rich composition: many different values for the minority currents and majority hole current could fit the JV characteristics, with only marginal differences in the fitting quality, measured by the RMSE. Around the best parameters found by the algorithm, it was not possible to clearly detect a region in which the RMSE has a minimum, as shown in Fig. A.2.

Moreover, besides the "optimal" region is where $J_{0n}{}^{p\text{-}aSi} \approx 10^{-19}$, this value is many orders of magnitude lower than that obtained for the solar cell at Position 1 (Sn-rich). Since the hole contact was supposed to be the same for all solar cells, this value is physically unreasonable, which suggests that the strong s-shape seen in the JV characteristics of solar cells with Ge-rich ZTGN cannot be described by this exchange current density model, as discussed in Chapter 3.

Bibliography

[1] J. Nelson, *The physics of solar cells*. World Scientific Publishing Company, 2003.

[2] Y. Liu, Y. Li, Y. Wu, G. Yang, L. Mazzarella, P. Procel-Moya, A. C. Tamboli, K. Weber, M. Boccard, O. Isabella, X. Yang, and B. Sun, "High-Efficiency Silicon Heterojunction Solar Cells: Materials, Devices and Applications," *Materials Science and Engineering R: Reports*, vol. 142, no. July, 2020.

[3] A. Richter, M. Hermle, and S. W. Glunz, "Reassessment of the Limiting Efficiency for Crystalline Silicon Solar Cells," *IEEE Journal of Photovoltaics*, vol. 3, no. 4, pp. 1184–1191, 2013.

[4] J. Haschke, O. Dupré, M. Boccard, and C. Ballif, "Silicon heterojunction solar cells: Recent technological development and practical aspects - from lab to industry," *Solar Energy Materials and Solar Cells*, vol. 187, no. July, pp. 140–153, 2018. Publisher: Elsevier B.V.

[5] M. Hermle, F. Feldmann, M. Bivour, J. C. Goldschmidt, and S. W. Glunz, "Passivating contacts and tandem concepts: Approaches for the highest silicon-based solar cell efficiencies," *Applied Physics Reviews*, vol. 7, no. 2, 2020. Publisher: AIP Publishing LLC.

[6] J. Melskens, W. M. M. Kessels, L. E. Black, B. W. H. van de Loo, B. Macco, and S. Smit, "Passivating Contacts for Crystalline Silicon Solar Cells: From Concepts and Materials to Prospects," *IEEE Journal of Photovoltaics*, vol. 8, no. 2, pp. 373–388, 2018.

[7] U. Wurfel, A. Cuevas, and P. Wurfel, "Charge carrier separation in solar cells," *IEEE Journal of Photovoltaics*, vol. 5, no. 1, pp. 461–469, 2015.

[8] R. V. Chavali, S. De Wolf, and M. A. Alam, "Device physics underlying silicon heterojunction and passivating-contact solar cells: A topical review," *Progress in Photovoltaics: Research and Applications*, vol. 26, no. 4, pp. 241–260, 2018.

[9] K. Yoshikawa, H. Kawasaki, W. Yoshida, T. Irie, K. Konishi, K. Nakano, T. Uto, D. Adachi, M. Kanematsu, H. Uzu, and K. Yamamoto, "Silicon heterojunction solar cell with interdigitated back contacts for a photoconversion efficiency over 26%," *Nature Energy*, vol. 2, no. 5, 2017.

[10] J. Pankov and M. Lampert, "Method of passivating a semiconductor device by treatment with atomic hydrogen," 1978.

[11] S. De Wolf and M. Kondo, "Nature of doped a-Si:H/c-Si interface recombination," *Journal of Applied Physics*, vol. 105, no. 10, 2009.

[12] M. Herman, M. Jankovec, and M. Topič, "Optimal I-V curve scan time of solar cells and modules in light of irradiance level," *International Journal of Photoenergy*, vol. 2012, 2012.

[13] M. Bivour, *Silicon heterojunction solar cells: Analysis and basic understanding*. Solare Energie- und Systemforschung/ Solar Energy and Systems Research, Stuttgart: Fraunhofer Verlag, 2017.

[14] C. Battaglia, S. M. De Nicolás, S. De Wolf, X. Yin, M. Zheng, C. Ballif, and A. Javey, "Silicon heterojunction solar cell with passivated hole selective MoO x contact," *Applied Physics Letters*, vol. 104, no. 11, 2014.

[15] S. Zhong, M. Morales-Masis, M. Mews, L. Korte, Q. Jeangros, W. Wu, M. Boccard, and C. Ballif, "Exploring co-sputtering of ZnO:Al and SiO 2 for efficient electron-selective contacts on silicon solar cells," *Solar Energy Materials and Solar Cells*, vol. 194, no. November 2018, pp. 67–73, 2019. Publisher: Elsevier B.V.

[16] M. Boccard, X. Yang, K. Weber, and Z. C. Holman, "Passivation and carrier selectivity of TiO 2 contacts combined with different passivation layers and electrodes for silicon solar cells," in *2017 IEEE 44th Photovoltaic Specialist Conference, PVSC 2017*, pp. 1–5, IEEE, 2017.

[17] J. Peter Seif, A. Descoeudres, M. Filipič, F. Smole, M. Topič, Z. Charles Holman, S. De Wolf, and C. Ballif, "Amorphous silicon oxide window layers for high-efficiency silicon heterojunction solar cells," *Journal of Applied Physics*, vol. 115, no. 2, 2014.

[18] W. Lin, M. Boccard, S. Zhong, V. Paratte, Q. Jeangros, L. Antognini, J. Dréon, J. Cattin, J. Thomet, Z. Liu, Z. Chen, Z. Liang, P. Gao, H. Shen, and C. Ballif, "Degradation Mechanism and Stability Improvement of Dopant-Free ZnO/LiF x /Al Electron Nanocontacts in Silicon Heterojunction Solar Cells," *ACS Applied Nano Materials*, vol. 3, no. 11, pp. 11391–11398, 2020.

[19] X. Yang, E. Aydin, H. Xu, J. Kang, M. Hedhili, W. Liu, Y. Wan, J. Peng, C. Samundsett, A. Cuevas, and S. De Wolf, "Tantalum Nitride Electron-Selective Contact for Crystalline Silicon Solar Cells," *Advanced Energy Materials*, vol. 8, no. 20, pp. 1–7, 2018.

[20] A. N. Fioretti, M. Boccard, R. Monnard, and C. Ballif, "Low-Temperature p-Type Microcrystalline Silicon as Carrier Selective Contact for Silicon Heterojunction Solar Cells," *IEEE Journal of Photovoltaics*, vol. PP, pp. 1–8, 2019. Publisher: IEEE.

[21] J. Bullock, Y. Wan, Z. Xu, S. Essig, M. Hettick, H. Wang, W. Ji, M. Boccard, A. Cuevas, C. Ballif, and A. Javey, "Stable Dopant-Free Asymmetric Heterocontact Silicon Solar Cells with Efficiencies above 20%," *ACS Energy Letters*, vol. 3, no. 3, pp. 508–513, 2018.

[22] R. Woods-Robinson, A. N. Fioretti, J. Haschke, M. Boccard, K. A. Persson, and C. Ballif, "Evaluating Materials Design Parameters of Hole-Selective Contacts for Silicon Heterojunction Solar Cells," *IEEE Journal of Photovoltaics*, pp. 1–12, 2020.

[23] D. M. Fébba, E. C. Bortoni, A. F. Oliveira, and R. M. Rubinger, "The effects of noises on metaheuristic algorithms applied to the PV parameter extraction problem," *Solar Energy*, vol. 201, no. November 2019, pp. 420–436, 2020. Publisher: Elsevier.

[24] D. T. Cotfas, P. A. Cotfas, and S. Kaplanis, "Methods to determine the dc parameters of solar cells: A critical review," *Renewable and Sustainable Energy Reviews*, vol. 28, pp. 588–596, 2013. Publisher: Elsevier.

[25] R. Abbassi, A. Abbassi, M. Jemli, and S. Chebbi, "Identification of unknown parameters of solar cell models: A comprehensive overview of available approaches," *Renewable and Sustainable Energy Reviews*, vol. 90, pp. 453–474, July 2018.

[26] A. R. Jordehi, "Parameter estimation of solar photovoltaic (PV) cells: A review," *Renewable and Sustainable Energy Reviews*, vol. 61, pp. 354–371, 2016. Publisher: Elsevier.

[27] S. Bader, X. Ma, and B. Oelmann, "One-diode photovoltaic model parameters at indoor illumination levels – A comparison," *Solar Energy*, vol. 180, no. January, pp. 707–716, 2019. Publisher: Elsevier.

[28] K. Ishaque, Z. Salam, S. Mekhilef, and A. Shamsudin, "Parameter extraction of solar photovoltaic modules using penalty-based differential evolution," *Applied Energy*, vol. 99, pp. 297–308, 2012. Publisher: Elsevier Ltd.

[29] J. Ma, Z. Bi, T. O. Ting, S. Hao, and W. Hao, "Comparative performance on photovoltaic model parameter identification via bio-inspired algorithms," *Solar Energy*, vol. 132, pp. 606–616, 2016. Publisher: Elsevier Ltd.

[30] E. Batzelis, "Non-iterative methods for the extraction of the single-diode model parameters of photovoltaic modules: A review and comparative assessment," *Energies*, vol. 12, no. 3, pp. 14–28, 2019.

[31] D. S. Pillai and N. Rajasekar, "Metaheuristic algorithms for PV parameter identification: A comprehensive review with an application to threshold setting for fault detection in PV systems," *Renewable and Sustainable Energy Reviews*, vol. 82, no. October 2017, pp. 3503–3525, 2018. Publisher: Elsevier Ltd.

[32] M. Campanelli and K. Emery, "Device-dependent light-level correction errors in photovoltaic I-V performance measurements," *Conference Record of the IEEE Photovoltaic Specialists Conference*, no. June, pp. 67–72, 2013.

[33] J. Brest, S. Greiner, B. Boskovic, M. Mernik, and V. Zumer, "Self-Adapting Control Parameters in Differential Evolution: A Comparative Study on Numerical Benchmark Problems," *IEEE Transactions on Evolutionary Computation*, vol. 10, no. 6, pp. 646–657, 2006.

[34] J. Liang, C. Yue, B. Qu, K. Yu, X. Chen, and S. Ge, "A performance-guided JAYA algorithm for parameters identification of photovoltaic cell and module," *Applied Energy*, vol. 237, no. August 2018, pp. 241–257, 2019. Publisher: Elsevier.

[35] K. Yu, X. Chen, X. Wang, and Z. Wang, "Parameters identification of photovoltaic models using self-adaptive teaching-learning-based optimization," *Energy Conversion and Management*, vol. 145, pp. 233–246, 2017. Publisher: Elsevier Ltd.

[36] X. Chen and K. Yu, "Hybridizing cuckoo search algorithm with biogeography-based optimization for estimating photovoltaic model parameters," *Solar Energy*, vol. 180, no. December 2018, pp. 192–206, 2019. Publisher: Elsevier.

[37] S. Lambert-Lacroix and L. Zwald, "Robust regression through the Huber's criterion and adaptive lasso penalty," *Electronic Journal of Statistics*, vol. 5, pp. 1015–1053, 2011.

[38] Y. G. Wang, X. Lin, M. Zhu, and Z. Bai, "Robust estimation using the huber function with a data-dependent tuning constant," *Journal of Computational and Graphical Statistics*, vol. 16, no. 2, pp. 468–481, 2007.

[39] R. Storn and K. Price, "Differential Evolution - A Simple and Efficient Heuristic for Global Optimization over Continuous Spaces," *Journal of Global Optimization*, vol. 11, no. 4, pp. 341–359, 1997.

[40] L. L. Jiang, D. L. Maskell, and J. C. Patra, "Parameter estimation of solar cells and modules using an improved adaptive differential evolution algorithm," *Applied Energy*, vol. 112, pp. 185–193, 2013. Publisher: Elsevier Ltd.

[41] S. Das, S. S. Mullick, and P. N. Suganthan, "Recent advances in differential evolution-An updated survey," *Swarm and Evolutionary Computation*, vol. 27, pp. 1–30, 2016. Publisher: Elsevier.

[42] G. Wu, X. Shen, H. Li, H. Chen, A. Lin, and P. N. Suganthan, "Ensemble of differential evolution variants," *Information Sciences*, vol. 423, pp. 172–186, 2018. Publisher: Elsevier Inc.

[43] D. Fébba, R. Rubinger, A. Oliveira, and E. Bortoni, "Impacts of temperature and irradiance on polycrystalline silicon solar cells parameters," *Solar Energy*, vol. 174, pp. 628–639, Nov. 2018. Publisher: Pergamon.

[44] J. Zhang and A. C. Sanderson, "JADE: Adaptive differential evolution with optional external archive," *IEEE Transactions on Evolutionary Computation*, vol. 13, no. 5, pp. 945–958, 2009.

[45] Q. Fan and Y. Zhang, "Self-adaptive differential evolution algorithm with crossover strategies adaptation and its application in parameter estimation," *Chemometrics and Intelligent Laboratory Systems*, vol. 151, no. 1550, pp. 164–171, 2016. Publisher: Elsevier B.V.

[46] R. Venkata Rao, "Jaya: A simple and new optimization algorithm for solving constrained and unconstrained optimization problems," *International Journal of Industrial Engineering Computations*, vol. 7, no. 1, pp. 19–34, 2016.

[47] R. V. Rao, V. J. Savsani, and D. P. Vakharia, "Teaching-learning-based optimization: A novel method for constrained mechanical design optimization problems," *CAD Computer Aided Design*, vol. 43, no. 3, pp. 303–315, 2011. Publisher: Elsevier Ltd.

[48] X. Ding, Z. Xu, N. J. Cheung, and X. Liu, "Parameter estimation of Takagi-Sugeno fuzzy system using heterogeneous cuckoo search algorithm," *Neurocomputing*, vol. 151, no. P3, pp. 1332–1342, 2015. Publisher: Elsevier.

[49] D. Simon, "Biogeography-based optimization," *IEEE Transactions on Evolutionary Computation*, vol. 12, no. 6, pp. 702–713, 2008.

[50] A. Jain and A. Kapoor, "Exact analytical solutions of the parameters of real solar cells using Lambert W-function," *Solar Energy Materials and Solar Cells*, vol. 81, no. 2, pp. 269–277, 2004. Publisher: North-Holland.

[51] M. Derick, C. Rani, M. Rajesh, M. E. Farrag, Y. Wang, and K. Busawon, "An improved optimization technique for estimation of solar photovoltaic parameters," *Solar Energy*, vol. 157, pp. 116–124, 2017. Publisher: Elsevier Ltd.

[52] T. Easwarakhanthan, J. Bottin, I. Bouhouch, and C. Boutrit, "Nonlinear Minimization Algorithm for Determining the Solar Cell Parameters with Microcomputers," *International Journal of Solar Energy*, vol. 4, no. 1, pp. 1–12, 1986.

[53] A. Ortiz-Conde, Y. Ma, J. Thomson, E. Santos, J. J. Liou, F. J. García Sánchez, M. Lei, J. Finol, and P. Layman, "Direct extraction of semiconductor device parameters using lateral optimization method," *Solid-State Electronics*, vol. 43, no. 4, pp. 845–848, 1999.

[54] A. Ferhat-Hamida, Z. Ouennoughi, A. Hoffmann, and R. Weiss, "Extraction of Schottky diode parameters including parallel conductance using a vertical optimization method," *Solid-State Electronics*, vol. 46, no. 5, pp. 615–619, 2002.

[55] K. Bouzidi, M. Chegaar, and A. Bouhemadou, "Solar cells parameters evaluation considering the series and shunt resistance," *Solar Energy Materials and Solar Cells*, vol. 91, no. 18, pp. 1647–1651, 2007.

[56] N. Maouhoub, "Photovoltaic module parameter estimation using an analytical approach and least squares method," *Journal of Computational Electronics*, vol. 17, no. 2, pp. 784–790, 2018. Publisher: Springer US.

[57] W. Peng, Y. Zeng, H. Gong, Y. Q. Leng, Y. H. Yan, and W. Hu, "Evolutionary algorithm and parameters extraction for dye-sensitised solar cells one-diode equivalent circuit model," *Micro and Nano Letters*, vol. 8, no. 2, pp. 86–89, 2013.

[58] H. G. Nunes, J. A. Pombo, P. M. Bento, S. J. Mariano, and M. R. Calado, "Collaborative swarm intelligence to estimate PV parameters," *Energy Conversion and Management*, vol. 185, no. November 2018, pp. 866–890, 2019. Publisher: Elsevier.

[59] S. Ebrahimi, E. Salahshour, M. Malekzadeh, and FranciscoGordillo, "Parameters Identification of PV Solar Cells and Modules Using Flexible Particle Swarm Optimization Algorithm," *Energy*, vol. 179, pp. 358–372, 2019. Publisher: Elsevier Ltd.

[60] N. Pourmousa, S. M. Ebrahimi, M. Malekzadeh, and M. Alizadeh, "Parameter estimation of photovoltaic cells using improved Lozi map based chaotic optimization Algorithm," *Solar Energy*, vol. 180, no. January, pp. 180–191, 2019. Publisher: Elsevier.

[61] H. Qasem, T. R. Betts, I. D. Sara, M. Bliss, J. Zhu, and R. Gottschalg, "Analysis of key performance parameter extraction from current voltage measurements of photovoltaic devices," *Conference Record of the IEEE Photovoltaic Specialists Conference*, pp. 002283–002288, 2011.

[62] D. Febba, V. Paratte, L. Antognini, J. Dreon, J. Hurni, J. Thomet, R. Rubinger, E. Bortoni, C. Ballif, and M. Boccard, "Effects of Work Function and Electron Affinity on the Performance of Carrier-Selective Contacts in Silicon Solar Cells Using ZnSn_x Ge_1-xN2as a Case Study," *IEEE Journal of Photovoltaics*, pp. 1–8, 2021.

[63] D. Febba, V. Paratte, L. Antognini, J. Dreon, J. Hurni, J. Thomet, C. Ballif, and M. Boccard, "ZnSnxGe1-xN2 as electron-selective contact for silicon heterojunction solar cells," in *2021 IEEE 48th Photovoltaic Specialists Conference (PVSC)*, pp. 0854–0857, IEEE, June 2021.

[64] I. S. Khan, K. N. Heinselman, and A. Zakutayev, "Review of ZnSnN 2 semiconductor material," *Journal of Physics: Energy*, vol. 2, no. 3, pp. 032007–032007, 2020.

[65] F. Deng, H. Cao, L. Liang, J. Li, J. Gao, H. Zhang, R. Qin, and C. Liu, "Determination of the basic optical parameters of ZnSnN_2," *Optics Letters*, vol. 40, no. 7, pp. 1282–1282, 2015.

[66] C. L. Melamed, J. Pan, A. Mis, K. Heinselman, R. R. Schnepf, R. Woods-Robinson, J. J. Cordell, S. Lany, E. S. Toberer, and A. C. Tamboli, "Combinatorial investigation of structural and optical properties of cation-disordered ZnGeN2," *Journal of Materials Chemistry C*, vol. 8, no. 26, pp. 8736–8746, 2020. Publisher: Royal Society of Chemistry.

[67] N. C. Coronel, L. Lahourcade, K. T. Delaney, A. M. Shing, and H. A. Atwater, "Earth-Abundant ZnSnxGe1-xN2 Alloys as Potential Photovoltaic. Absorber Materials," in *2012 38th IEEE Photovoltaic Specialists Conference*, pp. 003204–003207, IEEE, June 2012.

[68] P. Narang, S. Chen, N. C. Coronel, S. Gul, J. Yano, L. W. Wang, N. S. Lewis, and H. A. Atwater, "Bandgap tunability in Zn(Sn,Ge)N2 semiconductor alloys," *Advanced Materials*, vol. 26, no. 8, pp. 1235–1241, 2014.

[69] N. Beddelem, S. Bruyère, F. Cleymand, S. Diliberto, C. Longeaud, S. l. Gall, R. Templier, P. Miska, and B. Hyot, "Structural and functional properties of Zn(Ge,Sn)N2 thin films deposited by reactive sputtering," *Thin Solid Films*, vol. 709, no. October 2019, pp. 138192–138192, 2020. Publisher: Elsevier.

[70] A. M. Shing, N. C. Coronel, N. S. Lewis, and H. A. Atwater, "Semiconducting ZnSnxGe1-xN2 alloys prepared by reactive radio-frequency sputtering," *APL Materials*, vol. 3, no. 7, 2015.

[71] K. Javaid, W. Wu, J. Wang, J. Fang, H. Zhang, J. Gao, F. Zhuge, L. Liang, and H. Cao, "Band Offset Engineering in ZnSnN2-Based Heterojunction for Low-Cost Solar Cells," *ACS Photonics*, vol. 5, no. 6, pp. 2094–2099, 2018.

[72] K. Javaid, J. Yu, W. Wu, J. Wang, H. Zhang, J. Gao, F. Zhuge, L. Liang, and H. Cao, "Thin Film Solar Cell Based on ZnSnN2/SnO Heterojunction," *Physica Status Solidi - Rapid Research Letters*, vol. 12, no. 1, pp. 1–7, 2018.

[73] R. Qin, H. Cao, L. Liang, Y. Xie, F. Zhuge, H. Zhang, J. Gao, K. Javaid, C. Liu, and W. Sun, "Semiconducting ZnSnN2 thin films for Si/ZnSnN2 p-n junctions," *Applied Physics Letters*, vol. 108, no. 14, 2016.

[74] A. N. Fioretti, M. Boccard, A. C. Tamboli, A. Zakutayev, and C. Ballif, "Nitride layer screening as carrier-selective contacts for silicon heterojunction solar cells," in *AIP Conference Proceedings*, vol. 1999, pp. 040007–040007, 2018.

[75] R. V. K. Chavali, J. V. Li, C. Battaglia, S. De Wolf, J. L. Gray, and M. A. Alam, "A generalized theory explains the anomalous suns- V OC response of si heterojunction solar cells," *IEEE Journal of Photovoltaics*, vol. 7, no. 1, pp. 169–176, 2017. Publisher: IEEE.

[76] E. T. Roe, K. E. Egelhofer, and M. C. Lonergan, "Exchange current density model for the contact-determined current-voltage behavior of solar cells," *Journal of Applied Physics*, vol. 125, no. 22, 2019. Publisher: AIP Publishing LLC.

[77] A. Onno, C. Chen, P. Koswatta, M. Boccard, and Z. C. Holman, "Passivation, conductivity, and selectivity in solar cell contacts: Concepts and simulations based on a unified partial-resistances framework," *Journal of Applied Physics*, vol. 126, no. 18, 2019. Publisher: AIP Publishing LLC.

[78] E. T. Roe, K. E. Egelhofer, and M. C. Lonergan, "Limits of Contact Selectivity/Recombination on the Open-Circuit Voltage of a Photovoltaic," *ACS Applied Energy Materials*, vol. 1, no. 3, pp. 1037–1046, 2018.

[79] J. Dreon, J. Cattin, G. Christmann, D. Fébba, V. Paratte, L. Antognini, W. Lin, S. Nicolay, C. Ballif, and M. Boccard, "Performance Limitations and Analysis of Silicon Heterojunction Solar Cells Using Ultra-Thin MoO x Hole-Selective Contacts," *IEEE Journal of Photovoltaics*, vol. 11, no. 5, pp. 1158–1166, 2021. Publisher: IEEE.

[80] W. Walukiewicz, J. W. Ager, K. M. Yu, Z. Liliental-Weber, J. Wu, S. X. Li, R. E. Jones, and J. D. Denlinger, "Structure and electronic properties of InN and In-rich group III-nitride alloys," *Journal of Physics D: Applied Physics*, vol. 39, no. 5, 2006.

[81] C. G. Van de Walle and J. Neugebauer, "Universal alignment of hydrogen levels in semiconductors, insulators and solutions," *Nature*, vol. 423, pp. 626–628, June 2003.

[82] X. Yang, K. Weber, Z. Hameiri, and S. De Wolf, "Industrially feasible, dopant-free, carrier-selective contacts for high-efficiency silicon solar cells," *Progress in Photovoltaics: Research and Applications*, vol. 25, pp. 896–904, Nov. 2017.

[83] M. Bivour, C. Reichel, M. Hermle, and S. W. Glunz, "Improving the a-Si:H(p) rear emitter contact of n-type silicon solar cells," *Solar Energy Materials and Solar Cells*, vol. 106, pp. 11–16, 2012. Publisher: Elsevier.

[84] N. L. Adamski, Z. Zhu, D. Wickramaratne, and C. G. Van De Walle, "Optimizing n - type doping of ZnGeN2 and ZnSiN2," *Physical Review B*, vol. 100, no. 15, pp. 155206–155206, 2019. Publisher: American Physical Society.

[85] A. P. Jaroenjittichai and W. R. Lambrecht, "Electronic band structure of Mg-IV- N2 compounds in the quasiparticle-self-consistent GW approximation," *Physical Review B*, vol. 94, no. 12, pp. 1–8, 2016.

[86] R. A. Makin, K. York, S. M. Durbin, N. Senabulya, J. Mathis, R. Clarke, N. Feldberg, P. Miska, C. M. Jones, Z. Deng, L. Williams, E. Kioupakis, and R. J. Reeves, "Alloy-Free Band Gap Tuning across the Visible Spectrum," *Physical Review Letters*, vol. 122, no. 25, pp. 256403–256403, 2019. Publisher: American Physical Society.

[87] F. Kawamura, M. Imura, H. Murata, N. Yamada, and T. Taniguchi, "Synthesis of a Novel Rocksalt-Type Ternary Nitride Semiconductor MgSnN2 Using the Metathesis Reaction Under High Pressure," *European Journal of Inorganic Chemistry*, pp. 446–451, 2019.

[88] S. Lyu and W. R. Lambrecht, "Quasiparticle self-consistent GW band structures of Mg-IV-N2 compounds: The role of semicore d states," *Solid State Communications*, vol. 299, no. June, pp. 113664–113664, 2019. Publisher: Elsevier Ltd.

[89] A. L. Greenaway, A. L. Loutris, K. N. Heinselman, C. L. Melamed, R. R. Schnepf, M. B. Tellekamp, R. Woods-Robinson, R. Sherbondy, D. Bardgett, S. Bauers, A. Zakutayev, S. T. Christensen, S. Lany, and A. C. Tamboli, "Combinatorial Synthesis of Magnesium Tin Nitride Semiconductors," *Journal of the American Chemical Society*, vol. 142, no. 18, pp. 8421–8430, 2020.

[90] N. Yamada, K. Matsuura, M. Imura, H. Murata, and F. Kawamura, "Composition-Dependent Properties of Wurtzite-Type Mg 1+ x Sn 1– x N 2 Epitaxially Grown on GaN(001) Templates," *ACS Applied Electronic Materials*, no. 001, 2021.

[91] X. Cao, F. Kawamura, Y. Ninomiya, T. Taniguchi, and N. Yamada, "Conduction-band effective mass and bandgap of ZnSnN2 earth-abundant solar absorber," *Scientific Reports*, vol. 7, no. 1, pp. 1–10, 2017. Publisher: Springer US.